ONE-DIMENSIONAL HIGH-FIDELITY AND REDUCED-ORDER MODELS FOR THREE-WAY CATALYTIC CONVERTER

ONE-DIMENSIONAL HIGH-FIDELITY AND REDUCED-ORDER MODELS FOR THREE-WAY CATALYTIC CONVERTER

By

Tongrui Li, B.Eng.

A Thesis

Submitted to the School of Graduate Studies

In Partial Fulfilment of the Requirements

For the Degree of

Master of Applied Science

McMaster University

Master of Applied Science (2016) McMaster University

(Mechanical Engineering) Hamilton, Ontario, Canada

TITLE: One-Dimensional High-Fidelity and Reduced-Order Models For Three -Way Catalytic Converter

AUTHOR: Tongrui Li

SUPERVISOR: Dr. Fengjun Yan

NUMBER OF PAGES: xx, 128

ABSTRACT

To improve the performance of the three-way catalytic (TWC) converter, advanced control strategies and on-board diagnostics (OBD) systems are needed. Both rely on a relatively accurate but computationally efficient TWC converter model. This thesis aims to develop a control-oriented model that can be employed to develop the control strategies and OBD systems of the TWC converter.

The thesis consists of two parts, i.e., the high-fidelity model development and the model reduction. Firstly, a high-fidelity model is built using the energy and mass conservation principles. In this model, a constant inlet simulation is used to validate the warming-up characteristics, and a driving cycle simulation is used to calibrate the reaction rate parameters. The results of the simulation show that the high-fidelity model has adequate accuracy. Secondly, a reduced-order model is developed based on phase and reaction simplifications of the high-fidelity model. The aim of the development of the reduced-order model is to propose a computationally efficient model for further development of control strategies and state estimators for OBD systems. The accuracy of the reduced-order model is then validated by means of simulations.

ACKNOWLEDGEMENT

This research was undertaken thanks to the help of my supervisor Professor Fengjun Yan for his guidance with respect to the modeling of the three-way catalytic converter and the engine control strategy, as well as the financial support for the licenses of the GT-SUITE. Special appreciation also goes to Dr. Jinbiao Ning and Vida™ Fresh Air Corp. for their help and support for the tested data and scripts MATLAB coding.

Many thanks to the Department of Mechanical Engineering and its fellows, as well as McMaster University, for two memorable years. Also my gratitude to the country of Canada for its beauty and friendly people, and its open mind towards international students.

I would like to thank all my friends for their love and support, which have given me courage and determination even in the darkest days.

Last, I am grateful to my parents for their over 20 years' love and continuous support.

TABLE OF CONTENTS

LIST OF FIGURES

LIST OF TABLES

LIST OF SYMBOLS

Acronyms:

TWC - Three Way Catalysts

OBD - On-Board Diagnostics

CO - Carbon monoxide

NO - Nitric oxide

HC - Hydrocarbon

LEV - Low-Emission-Vehicle

ECE - Economic Commission for Europe

ECU - Engine Control Unit

CSTR - Continuous Stirred Tank Reactor

EKF - Extent Kalman Filter

Variables:

Ψ_s - Effective heat capacity of solid phase $(J/m^3 \cdot K)$

T_g - Gas temperature (K)

T_s - Solid temperature (K)

f_{sb} - Solid fraction of substrate

λ_{sb} - Thermal conductivity of solid phase ($J/m \cdot s \cdot K$)

λ_g - Thermal conductivity of gas phase ($J/m \cdot s \cdot K$)

h - Heat transfer coefficient ($J/m^2 \cdot s \cdot K$)

S - Specific area (m^2/m^3)

Δh_j - Enthalpy exchanging expression (J)

r_j - Reaction rate

ρ_{cor} - Density of cordierite (kg/m^3)

ρ_{al} - Density of Alumina (kg/m^3)

c_{cor} Specific heat of Cordierite ($J/kg \cdot K$)

c_{al} - Specific heat of Alumina ($J/kg \cdot K$)

V_{cor} - Volume of Cordierite (m^3)

V_{al} - Volume of Alumina (m^3)

L - Converter length (m)

D - Width of the channel (m)

w_1 - Substrate thickness (m)

w_2 - Washcoat thickness (m)

ε - Void fraction

Nu - Nusselt number

D_h - Characteristic length (m)

ρ - Gas density (kg/m^3)

μ - Gas viscosity (Pa · s)

v Gas velocity (m/s)

η - Stoichiometric number

H - Enthalpy of the species

R - Gas constant

ρ_s - Exhausted gas density (kg/m^3)

$c_{p,g}$ - Exhausted gas specific heat ($J/kg \cdot K$)

u_z - Exhausted gas velocity (m/s)

A - Front area of substrate (m^3)

w - molar flow rate of inlet gas (mol/s)

$c_{g,i}$ - Concentration

k_j - Reaction rate parameter

A_i - Pre-exponent multiplier

E_i - Activation energy

G - Adsorption rate of reactant

Chapter 1 . Introduction

1.1 Emission regulations

Gasoline engines have been the primary power source for transportation since the second industrial revolution. They have many advantages, such as their high efficiency and low cost. However, a serious problem caused by the combustion of fossil fuels is the emission of pollutants, including hydrocarbon (HC), carbon monoxide (CO) and nitric oxide (NO), which are some of the main causes of environmental degradation. This problem has been recognised by a growing number of organisations and governments.

The United States was the first country to regulate these pollutant emissions through legislation in the 1960s. In 1963, the Clean Air Act was passed, and California began to control the emissions of fuel vapour from the crankshaft case of gasoline engines. From 1966 to 1975, a number of policies and regulations were implemented to gradually reduce vehicle emissions. In 1968, the U.S. Federal government passed the Seven Working Conditions Act. In 1972 and 1975, the LA-4C (FPT-72) and LA (FPT-75) driving cycles were applied to test vehicle pollutant emissions under driving conditions. At the same time, laws were also passed to limit NOx emissions. From 1975 through to the 1980s, American vehicle emissions regulations were significantly increased to limit NOx emissions. 1994 was a key year for vehicle emissions regulations in the US, when extremely strict low-emission vehicle (LEV) regulations were introduced. Up until the present day, these regulations have been revised to further lower the acceptable emission level. A series of

detailed clauses in these revisions have limited the permitted levels of pollutant emissions, as shown in Table 1.1 and Table 1.2.

Table 1.1: US Tier 1 LEV regulations (FTP 75 g/mile)

Vehicles	50,000 miles / 5 years				100,000 miles / 10 years			
	THC	CO	NO_x	PM	THC	CO	NO_x	PM
Passenger car	0.41	3.4	0.4	0.08	-	4.2	0.6	0.1
LLDT LVW < 3,750 lb	-	3.4	0.4	0.08	0.8	4.2	0.6	0.1
LLDT LVW > 3,750 lb	-	4.4	0.7	0.08	0.8	5.5	0.97	0.1
HLDT LVW < 5,750 lb	0.32	4.4	0.7	-	0.8	6.4	0.98	0.1
HLDT LVW > 5,750 lb	0.39	5.0	1.1	-	0.8	7.3	1.63	0.12

Table 1.2: US Tier 2 LEV regulations (FTP 75 g/mile)

Bin #	50,000 miles / 5 years				120,000 miles / 10 years			
	NMOG	CO	NO_x	PM	NMOG	CO	NO_x	PM
8	0.100	3.4	0.14	-	0.125	4.2	0.2	0.02
7	0.075	3.4	0.11	-	0.09	4.2	0.15	0.02
6	0.075	3.4	0.08	-	0.09	4.2	0.1	0.01
5	0.075	3.4	0.05	-	0.09	4.2	0.07	0.01
4	-	-	-	-	0.07	2.1	0.04	0.01
3	-	-	-	-	0.055	2.1	0.03	0.01
2	-	-	-	-	0.01	2.1	0.02	0.01
1	-	-	-	-	-	-	-	-

From 1970 onwards, the Economic Commission for Europe (ECE) has controlled the pollutant emissions of light gasoline vehicles by means of the ECEW5 regulation and has gradually limited the emission of NOx by passing the ECER83 and ECER15-8 regulations. Between 1992 and 2014, these regulations were revised and made stricter through the passing of the Euro I to Euro VI emissions regulations, as shown in Table 1.3 [1][2][3].

Table 1.3: European emission standards for passenger vehicles (g/km)

Tire	Date	THC	NO_x	CO	PM
Euro 1	July 1992	1.0		2.72	-
Euro 2	January 1996	0.3		2.2	-
Euro 3	January 2000	0.20	0.15	2.3	-
Euro 4	January 2005	0.10	0.08	1.0	-
Euro 5	September 2009	0.10`	0.06	1.0	0.005
Euro 6	September 2014	0.10	0.06	1.0	0.005

Other countries across the globe, such as China, Japan, and India, also have emissions regulations, which have been modified over time to make them stricter.

1.2 The three-way catalytic (TWC) converter

Serious environmental problems and strict regulations have forced vehicle manufacturers to improve not only fuel combustion efficiency but also the performance of the after-treatment system.

Engine exhaust fumes contain both oxidizing species (O_2 and NOx) and reducing species (HC and CO). Pollution reduction can be accomplished by means of reactions between the oxidizing and reducing species. These reactions only became possible when the three-way catalytic (TWC) converter was invented. With its low cost and high

conversion efficiency, the TWC converter is one of the most efficient devices for the after-treatment system.

Figure 1.1: Three-way catalytic converter

The key component of the TWC converter is a honeycomb-shaped ceramic monolith, called the “substrate”, which provides a large surface area for surface reactions, as shown in Figure 1.2.

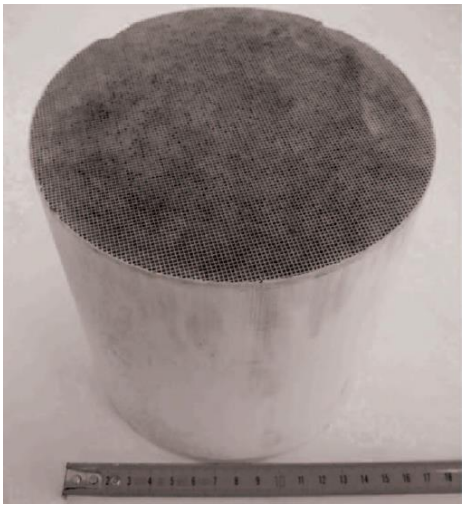

Figure 1.2: Honeycomb structure of the substrate

The small channels of the monolith help to avoid fouling, since gas can easily travel through the channels. The substrate material must be heat-resistant, due to its high operating temperature. Cordierite, which has a low thermal expansion coefficient, is widely used for the substrates of TWC converters.

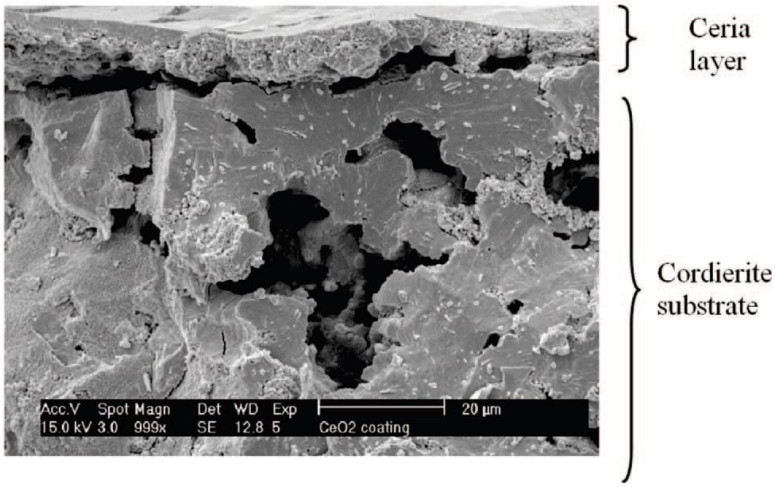

Figure 1.3: Microscope image of a cordierite substrate loaded with phases

The thin layers, referred to as the "wash-coat", that contain the catalysts are painted on the surface of the channels in a layer typically less than 10µm thick, as shown in Figure 1.3 The catalysts are composed mainly of noble metals (catalyst), cerium-based oxides and alumina [4].

1.3 Control and diagnosis of the TWC converter

The performance of the TWC converter is mainly determined by two factors: the concentration ratio of the reactants and the converter's temperature. These factors depend on the fuel injection and ignition timing of the engine. In other words, the performance of the TWC converter is closely related to the control strategies of the engine.

Currently, the concentration ratio of the reactants can be accurately controlled by electronic fuel injection systems. However, the TWC converter's internal temperature control strategy still needs to be modified to improve the converter's performance. A model-based control strategy can maintain the temperature of the TWC converter within an ideal range.

In addition to model-based control, diagnosis of the TWC converter is important to keep it in good working condition. Diagnosis is usually performed by the on-board diagnostics (OBD) system. When the TWC converter is degraded and fails, the OBD system can provide users with timely feedback.

1.4 Novelty and contribution

This thesis proposes an accurate and computationally efficient one-dimensional control-oriented TWC converter model.

The complete design process for the high-fidelity TWC converter model is presented, including a determination of the one-dimensional heat transfer mechanism and a calculation of the pollutant concentrations based on reaction kinetics. The high-fidelity model accurately simulates the temperature and pollutant concentrations.

A reduced-order model is built through phase and reaction simplifications of the high-fidelity model. The reduced-order model decreases the model's computational cost while maintaining sufficient accuracy. The reduced-order model is more applicable to the control system and state estimation.

1.5 Thesis outline

This thesis consists of five chapters: an introduction, a literature review, presentations of the high-fidelity and reduced-order models, and a conclusion.

Chapter 1 provides a brief introduction to the history and fundamentals of the TWC converter. The structure and reactions of the TWC converter are also described. Moreover, the novelty and contribution of the research presented in this thesis are identified in this chapter.

Chapter 2 introduces current TWC converter control strategies and their advantages and disadvantages. Furthermore, the purposes of the high-fidelity and reduced-order models are clarified. Current advances in research related to the TWC converter model are discussed to provide a better understanding of mainstream ideas about this model.

Chapter 3 presents a high-fidelity TWC converter model. The high-fidelity model reflects the one-dimensional heat and mass transfer mechanism of the solid and gas phases. The simulations are processed and the experimental and simulated results are compared to ensure the accuracy of the high-fidelity model.

Chapter 4 describes the development of the reduced-order TWC converter model. The reduced-order model is built by simplifying the high-fidelity model. The results of the high-fidelity and reduced-order models are compared to ensure that the two models have equivalent accuracy levels.

The final chapter presents the conclusion and recommendations for further research.

Chapter 2． Objective and Literature Review

This chapter describes the purposes of high-fidelity and reduced-order models by means of a literature review. TWC converter models can be used for various purposes, such as model-based control strategies and OBD systems development. The model-based control strategies and OBD systems are critical to the performance and maintenance of the converter [5].

2.1 Purpose and requirements

The model proposed in this thesis can be applied to the development of control strategies and OBD systems.

2.1.1 Control strategies

Currently, increasingly strict emission regulations are difficult to meet if the system control strategies of TWC converters do not include the converter's internal dynamics (such as reaction mechanism and temperature) [6]. Therefore, research into TWC control strategies which include the converter's internal dynamics and aim to improve the converter's performance is required.

As mentioned in Chapter 1, previous researchers have found that the conversion efficiency of the TWC converter is highly dependent on catalyst temperature [7][8], as

shown in Figure 2.1. The TWC converter's internal temperature control strategy still needs to be modified to improve the converter's performance.

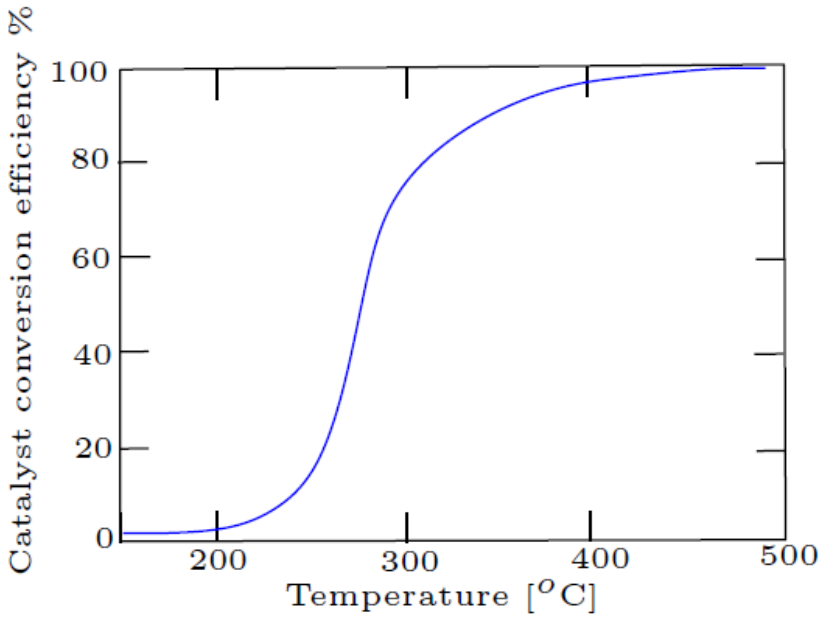

Figure 2.1: Conversion efficiency as a function of temperature in the TWC converter [17]

Commonly, when TWC conversion efficiency reaches 50%, the corresponding temperature is called the "light-off" temperature [9]. The process during which the temperature increases from the initial point to the light-off point is known as "warming-up". Many pollutants are expelled in the exhaust during the warming-up stage due to the low conversion efficiency. Therefore, increasing the speed of the warming-up process is important to enable the converter to reach a higher level of pollutant reduction [10][11][12].

Traditionally, the converter's warming-up process relies on the time-shift control [13]. During a cold start, the engine initiates the warming-up mode, and once the light-off point is reached, the optimal combustion mode is switched on. In the warming-up mode,

exhaust gas temperature can be raised by modifying the ignition timing, which increases the speed of the converter's warming-up [14]. However, this usually leads to a degradation in combustion efficiency [15]. Due to the detrimental effects on combustion, this open-loop process leads to a substantial increase in fuel consumption. Therefore, the light-off point needs to be accurately detected in order to obtain a balance between warming-up and fuel consumption [5][16][17].

The light-off temperature can be determined by temperature sensors mounted in the coolant system [18]. The thermal behaviour of the coolant system can be indirectly related to the engine and the exhaust line temperatures. However, this information is easily biased by other heat sources [19].

An alternative means of determining the warming-up control reference is by using models. An accurate model that reflects the internal temperature and the reaction mechanism inside the converter can provide a more certain and stable control reference for the TWC converter's thermal management system [20][21][22]. With an accurate yet simplified model, the time-shift control strategy can be modified, and more advanced control strategies can also be developed to meet future emission regulations [23].

Although many of the effects that occur inside TWC converters are well known [11], it is also a challenge to convert them into a reliable and accurate mathematical model. Not only is the number of reactions relatively large, but the converter's physical characteristics are also highly dynamic [24][25]. Converter inputs include exhaust gas

concentrations, temperature, and flow rate, which are some of the variables leading to the dynamic nature of the converter's operation.

2.1.2 On-board diagnostics (OBD)

The OBD system assists in troubleshooting problems in a vehicle subsystem and helps manufacturers to monitor the states of different components and detect failures. A failure in an after-treatment system would result in a vehicle exceeding emissions limits. The OBD system can detect any critical failures, which can help users to prevent serious damages to their vehicles and to reduce repair costs.

OBD performance is a direct function of the ability to measure and estimate internal states. This is usually done by means of sensors. However, sensors cannot be used to measure all the states the OBD needs, because this is not feasible and involves high costs. Models and state estimators can sometimes be used as virtual sensors to estimate the states that sensors cannot measure directly. With respect to the TWC converter, these models need to be implementable in the engine control unit (ECU). However, in order to ensure stability, the ECU's computational ability is limited. Thus, computational efficiency is of great importance in model development.

2.2 Advanced research on the TWC converter model

Previous research on the TWC converter has mainly focused on reaction kinetic modelling, heat and mass transfer modelling, and whole model structure modelling. A summary of the general framework of the research is provided in what follows.

2.2.1 Research on chemical reaction kinetics inside the TWC converter

The reactions that occur in TWC converters are heterogeneous solid-gas phase surface reactions [26]. The composition and active components of the catalysts are complex and variable, and the TWC converter's operating conditions are complicated [27]. Thus, one of the main challenges in building a kinetic model of the TWC converter is obtaining the appropriate kinetic mechanism [28]. An appropriate kinetic model is crucial for improving the TWC converter model's predictive power, especially in predicting cold start emissions and the light-off temperature [28]. Research on reaction kinetics is helpful for understanding the performance of catalytic converters and for modelling TWC converters [29]. The simplest approach to kinetic modelling is the look-up table [30]. In this approach, the kinetic model is represented by a database of conversions for various species as a function of temperature and space velocity. The advantage of this approach is that the model is computationally efficient [28]. However, as it does not describe the underlying chemical processes, its applicability is limited. Another approach is the microkinetic model. However, this model is at the opposite extreme from the look-up table, since all the intermediate reaction steps are considered and various reaction rate parameters are obtained from experiments [28][31][32][33]. As it requires intensive computation, the microkinetic model is not appropriate for control applications.

A middle path involves finding a balance between accuracy and complexity. In this regard, researchers use a single global rate expression for each reaction. For this purpose, the Langmuir-Hinshelwood mechanism is increasingly employed. Kinetic models that use the Langmuir-Hinshelwood mechanism typically have good predictive power, which helps to develop control algorithms [28].

The application of the Langmuir-Hinshelwood mechanism in TWC converter modelling has its basis in the pioneering work of Voltz, Morgan, Liederman, and Jacob [34], who developed a set of equations for the oxidizing reaction kinetics of CO and HC. In this research, they used mixtures of synaptic gas, with C_3H_6 as a representative hydrocarbon. The result of their experiment was consistent with previous research. The enhancement of oxidations by O_2 and inhibitions by CO and C_3H_6 also aligned with the findings of previously published studies [34]. The results showed that the inhibitions of CO and C_3H_6 were closely related to chemisorption, a kind of adsorption that involves a chemical reaction between the surface and adsorbate of CO and C_3H_6 on active sites. Moreover, these researchers developed a kinetic model to describe the oxidation of CO and HC in real engine exhausts. Their kinetic model provided a description of reaction rates under the influence of chemisorption. By comparing their model results and the testing results, they found that reaction rates were also related to temperature, as indicated by the values of the modified activation energies. The kinetic equations of oxidization reactions proposed by Voltz et al. [34] have been applied by numerous researchers, some of whom have modified and fixed the reaction rate parameters and added the reaction kinetics of NO.

Although kinetic parameter estimation based on laboratory experiments is well-controlled and well-behaved, it cannot be translated directly to engine data because of the following: the sensitivity of the kinetic parameters to wash-coat and formulations; the difficulty in obtaining the same level of deactivation; and the aging of the catalytic process [28][35][36]. Due to the promoting and inhibiting roles played by H_2O and CO_2, parameter estimation cannot be generalized; nor can the sensitivity of the kinetic parameters to the outer environment, such as feed composition and temperature. With respect to developing technologies, parameter estimation using optimization methods, which minimize the errors between measured and simulated data, is useful for estimating kinetic parameters.

The first reported estimation of kinetic parameters using a computer-aided method was based on conjugate gradients [37]. This research examined 13 different reactions using the Langmuir-Hinshelwood mechanism and estimated 95 parameters using a multidimensional conjugate gradient optimization method. However, this research was based on results obtained under controlled steady-state conditions in a laboratory setup.

The systems in which multiple kinetic parameters appear and in which multiparameter optimization is performed can possess multiple minima. Therefore, it is necessary to obtain a global minimum to provide the lowest objective function value. Certain exploratory optimization algorithms such as the genetic algorithm (GA) and the adaptive simulated annealing and downhill simplex can help to obtain the global minimum. Glielmo and Santini's study [38] was the first to use GA to optimize the kinetic parameters. These authors tuned seven parameters. Pontikakis, Konstantas, and Stamatelos [39] tuned

ten parameters using the same method in their research. Ramanathan and Sharma [28] used a similar method based on the minimization of the errors between the measured and simulated data through a combination of evolutionary and local optimization methods. They considered 15 reactions and tuned a total of 38 parameters.

2.2.2 Research on heat and mass transfer inside the TWC converter

Improved heat and mass transfer performance can significantly reduce the light-off time of the TWC converter monolith and thus increase conversion efficiency [40][41]. Research on heat and mass transfer inside the TWC converter has included analyses of density and temperature distribution [42][43], determinations of the heat transfer coefficient, and examinations of the parameters that can impact the performance of heat and mass transfer inside the converter.

The heat and mass transfer model is an important component of the TWC converter model. For example, Votruba et al. [44] developed an appropriate model of heat and mass transfer inside the TWC monolith that considered the convective heat and mass transfer in the holes of the converter's honeycomb structure, the longitudinal heat conduction within the solid structure, and the interface of heat and mass transfer between the gas and solid structures [44]. The results of this model agreed with experimental observations.

Heat and mass transfer can be considered both two-dimensionally and one-dimensionally. Unlike Votruba et al. [44], M. Flytzani-Stephanopouloqt et al. [45] developed a two-dimensional heat transfer model without ambient heat transfer. Without considering chemical reactions, the model was solved analytically to provide solid and gas

temperature profiles in two dimensions inside the converter monolith. Boehman [46] also developed a model for radiation heat transfer in converter passages that clarified the impact of radiation heat transfer by examining the influence of the operating temperature of the surface reaction.

2.2.3 Research on TWC converter modelling

Various models in the literature describe the TWC converter with varying degrees of complexity [47][48][49][50][51]. For example, Oh and Cavendbh [48] developed a transit mathematical model of catalyst monoliths that accounted for the simultaneous processes of heat transfer, mass transfer, and chemical reactions. This model simulated the dynamic behaviour of a catalytic monolith following a step change in the feed stream temperature. It examined the monolith's response to this increase as a function of catalyst design parameters and operation conditions to analyse the effects of these variables on the light-off behaviour of the catalyst [48]. In addition, this model examined the transient response of a hot monolith that was subjected to a cool feed stream containing high concentrations of pollutant species. The Pt-catalysed oxidation reactions of CO, HC and H_2 were also analysed. However, this model did not consider some important reactions, such as those related to NOx.

In addition to the physics-based model mentioned previously, some phenomenological models have also been developed. For example, Brandt and Grizzle [52] developed a more appropriate model for control engineering. The formulation of this model

focused on the mass ratio and the air-fuel ratio (AFR). Since the AFR is also a fundamental variable in most engine models, this model can be conveniently connected to an engine model to create a complete engine after-treatment system for further research.

Another way to classify TWC converter models is by dimension: zero-dimension, one-dimension, two-dimension, and three-dimension. The differences between these models are the direction of heat and mass transport and the diffusion direction inside the converter. In a zero-dimensional TWC converter model, the converter is considered as a continuous stirred tank reactor (CSTR). The zero-dimension model is only appropriate for research in which the effect of the TWC converter is not significant. The simple input and output variants are not appropriate to research on the internal mechanisms of the TWC converter. For example, Aimard and Sorine [53] developed a zero-dimension TWC converter model. Their physical model was based on simplified dynamics of the TWC converter and focused on oxygen storage. This model was validated by experimental results.

Using a mechanism consisting of 23 reactions, Koc et al. [54] examined the diffusion in the wash-coat and the microkinetics of the oxidation of CO, HC and the reduction of NOx. The mechanism of the TWC monolith was examined in two steps. In the first step, the catalytic converter was considered as a CSTR. Qualitative agreement between the simulated results and the tested data indicated the robustness of the model. In the second step, the TWC converter monolith was modelled as a two-dimensional model. The TWC converter was considered as a plug-flow reactor (PFR) and the diffusion in the wash-coat was examined [54].

For practical applications, a one-dimensional model that captures all the physics has been found to be sufficient for explaining the important aspects of these reactors. One-dimensional models are optimal, as they are computationally inexpensive and mathematically robust [35]. Rao et al. [35] developed a TWC model similar to the model developed by Oh and Cavendish [48] that considered a more detailed set of reactions and kinetics.

2.3 Research on converter model reduction

Vehicles need to function in different conditions. Hence, the working conditions of the ECU are harsh under various temperatures and humidity and vibration levels. In addition, the sharp changes in the power supply and the electromagnetic waves from inside and outside the vehicle disturb the ECU's working conditions. Therefore, the ECU's computational ability needs to be limited to ensure stability. As a model designed to process the engine control or state estimation, it should be as simple as possible computationally.

Simplification of the converter model can be achieved by different methods. One is to build sub-models to separate oxygen storage reactions from other reactions, instead of considering all reactions concurrently. Brant, Wang, and Grizzle [55] developed a simplified model of this kind by splitting it into three parts: standard steady-state efficiency curves driven by tailpipe AFR, an oxygen storage mechanism model similar to that in [56] to account for the modification of AFR, and a thermal dynamic of the converter's warming-up process. These methods are widely used in other research, such as [57]. Figure 2.2 illustrates the simplified model structure.

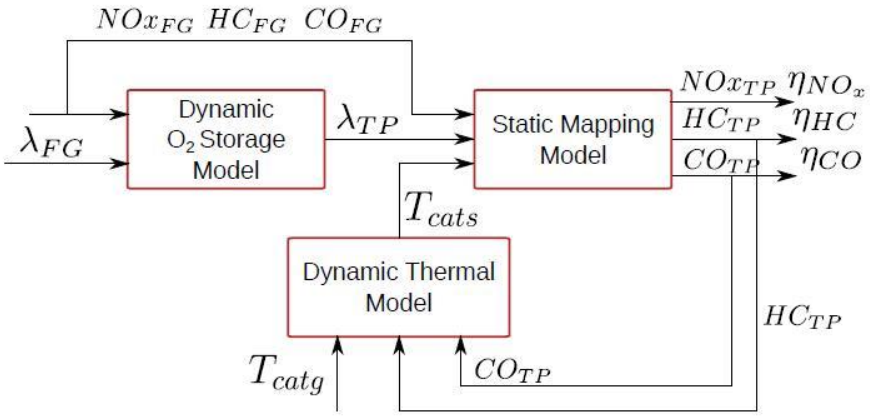

Figure 2.2: A simplified TWC system model including sub-models [77]

Figure 2.2 shows how to obtain the tailpipe AFR (λ_{TP}) from the oxygen storage model and input information. The temperature of the catalysts is obtained from the thermal model. The tailpipe AFR, catalyst temperature, and input concentrations are used to obtain the output pollutant concentration by means of the look-up table of the steady mapping model. However, the static map used in the mapping model covers only the steady state, so this kind of simplified model does not focus on the warming-up stage. In addition, the thermal dynamic model is not concrete enough to reflect the complex heat transfer mechanism or the heat released by the reactions inside the converter.

Surenahalli et al. [58] [59] provided another model reduction method, which implemented a phase reduction by combining the gas and solid phases. This reduced-order model was employed for temperature estimation using the Extended Kalman Filter (EKF). Although Surenahalli et al. [58] [59] mainly focused on diesel oxidation catalysts (DOC),

the structures and principles of TWC and DOC are similar. Therefore, a similar simplification method is employed in this research.

Chapter 3 . The high-fidelity TWC converter model

3.1 Development of the high-fidelity TWC converter model

As introduced above, researchers have developed a variety of models to describe the mechanisms of TWC converters. These models vary in accuracy and complexity. The high-fidelity model proposed in this chapter is a one-dimensional single-square channel approximation of the TWC converter. The heat and mass transfer of the high-fidelity model assumes that a single channel can represent a TWC converter, and the model simulates the mass and energy conservation of the converter in the gas and solid phases. The objective of this chapter is to develop a sufficiently accurate high-fidelity model. This can be achieved by determining the heat transfer characteristics and tuning the reaction rate parameters.

3.1.1 Assumptions

Some important assumptions are made to reduce the complexity of the high-fidelity TWC converter model.

As mentioned in the previous chapter, two-dimensional and three-dimensional models are more accurate than one-dimensional models, but they are too complicated to be applied in control systems and state estimations. One-dimensional converter models are more efficient for controllers and estimators, since they are computationally inexpensive and mathematically robust. The Biot (Bi) number of the converter channel was calculated and

found to be lower than 0.12. Therefore, it is justified to assume that the model is one-dimensional. The calculation of the Bi number is presented separately in Appendix C.

The second assumption is that all the reactions occur in the surface phase of the converter. As shown in Figure 3.1, the molecules of the reactants are first adsorbed into the wash-coat. Then, chemical reactions occur as molecules collide. This mechanism is based on the theory of the Langmuir-Hinshelwood mechanism [60].

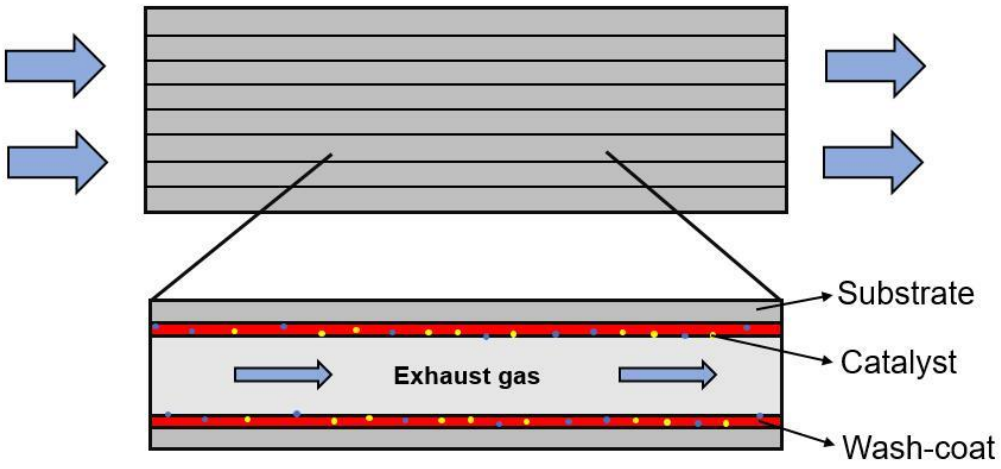

Figure 3.1: Schematic showing the flow of exhaust gas through the TWC

The final assumption is that heat transfer between the converter and the atmosphere is negligible, since the heat prevention material of the outer layer can block most of the heat transfer to the environment [61].

3.1.2 Heat and mass transfer of the high-fidelity model

Similarly to Oh and Cavendish [48], a one-dimensional heat and mass transfer model is developed based on the heat and mass conservation of the gas and solid phases. The equations of the heat and mass transfer are as follows:

- Solid phase energy conservation:

$$\Psi_s \frac{\partial T_s}{\partial t} = f_{sb}\lambda_{sb}\frac{\partial^2 T_s}{\partial x^2} + hS\left(T_g - T_s\right) - \sum_{j=1}^{n}\Delta h_j r_j \quad (1)$$

In equation (1), the left term is the overall heat transfer of the solid phase. T_g and T_s are the temperatures of the gas and the solid. The solid phase contains two kinds of materials. Therefore, the effective heat capacity Ψ_s needs to be calculated based on material density, material-specific heat, and channel geometries, as shown in equation (2):

$$\Psi_s = \frac{\rho_{cor}c_{cor}V_{cor}+\rho_{al}c_{al}V_{al}}{LD^2} \quad (2)$$

In equation (2), ρ_{cor}, c_{cor}, and V_{cor} are the density, specific heat, and volume of cordierite (the substrate material). ρ_{al}, c_{al}, and V_{al} are the density, specific heat and volume of alumina (the wash-coat material).

The volumes of the substrate and wash-coat are calculated based on the channel geometries. Figure 3.2 shows the square channel geometries.

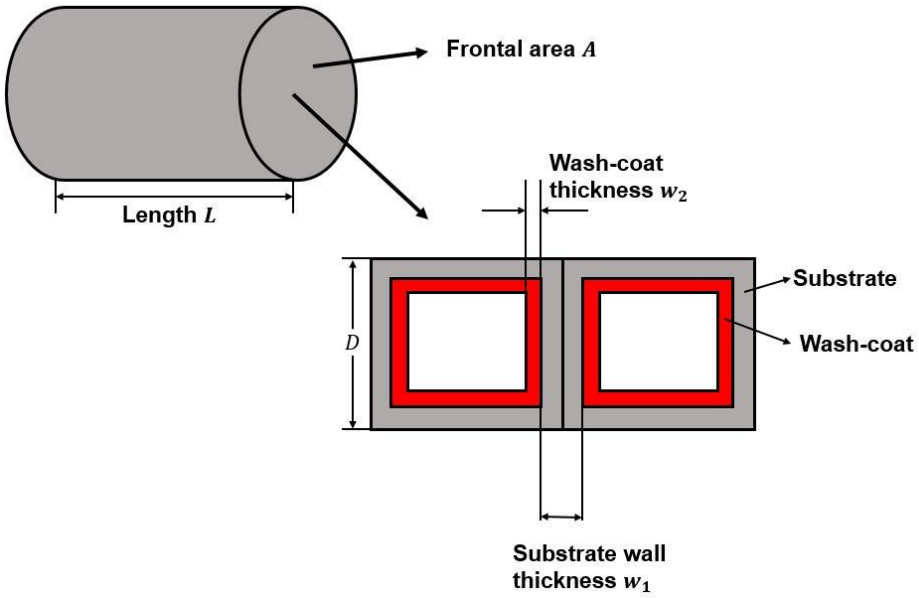

Figure 3.2: Definitions for square channel geometries

In Figure 3.2, the width of the channel, D, can be determined based on cell density, which is the number of channels in the unit frontal area (1 m^2). Equation (3) shows the calculation of D.

$$\mathrm{D} = \sqrt{1/\text{cell density}} \tag{3}$$

The volumes of the substrate and the wash-coat are given in equations (4) and (5).

$$V_{cor} = L(2w_1 D - w_1^2) \quad (4)$$

$$V_{al} = 4Lw_2(D - w_1 - w_2) \quad (5)$$

The cordierite specific heat (c_{cor}) varies with the temperature. The values of the cordierite-specific heat are given in Appendix B. The alumina-specific heat is 1,000 $J/kg \cdot K$.

Table 3.1 shows the values related to the square channel geometries.

Table 3.1: Values of the square channel geometries

Item	Values
Frontal area (A)	0.0082 m^2
Length (L)	150 mm
Substrate thickness (w_1)	1.0922×10^{-4} m
Wash-coat thickness (w_2)	1×10^{-5} m
Cell-density	1394910 $/m^2$
Channel width (D)	8.47×10^{-4} m
Void fraction (ε)	0.719
Specific area (S)	16471.9 m^2/m^3

Characteristic length (D_h)	1.75×10^{-4}m
Cordierite density (ρ_{cor})	1720 kg/m^3
Alumina density (ρ_{al})	1300 kg/m^3
Cordierite specific heat (c_{cor})	Appendix B
Alumina specific heat (c_{al})	1000 $J/kg \cdot K$

The first term on the right side of equation (1) is the heat conduction in one dimension along the axial direction of the substrate [62], where f_{sb} stands for the solid fraction of the substrate. f_{sb} is calculated in equation (6).

$$f_{sb} = 1 - \varepsilon \tag{6}$$

In equation (6), ε is the void fraction of the reactor. The void fraction can be calculated by means of equation (7) below.

$$\varepsilon = \frac{(D - w_1 - 2w_2)^2}{D^2} \tag{7}$$

In this study, the wash-coat is relatively thin (commonly referred to $1\times 10^{-5}\,\mathrm{m}$) compared to the substrate ($1.0922\times 10^{-4}\,\mathrm{m}$). Therefore, the solid phase's thermal conductivity is directly represented by λ_{sb}, which is $1.5\,\mathrm{J/m\cdot s\cdot K}$.

The second item on the right side of equation (1) is the heat transfer from the gas phase to the solid phase, where h stands for the gas-solid heat transfer coefficient, and S stands for the surface area of the solid substrate per converter volume [63].

The heat transfer coefficient h depends on the Nusselt number (Nu) for a fully-developed laminar flow through a channel. The heat transfer coefficient can be calculated by equation (8),

$$h = Nu\frac{\lambda_g}{D_h} \tag{8}$$

where the of the gas λ_g is given by equation (9) [28][64],

$$\lambda_g = 2.66 \times 10^{-4} T_g^{0.805} \quad (9)$$

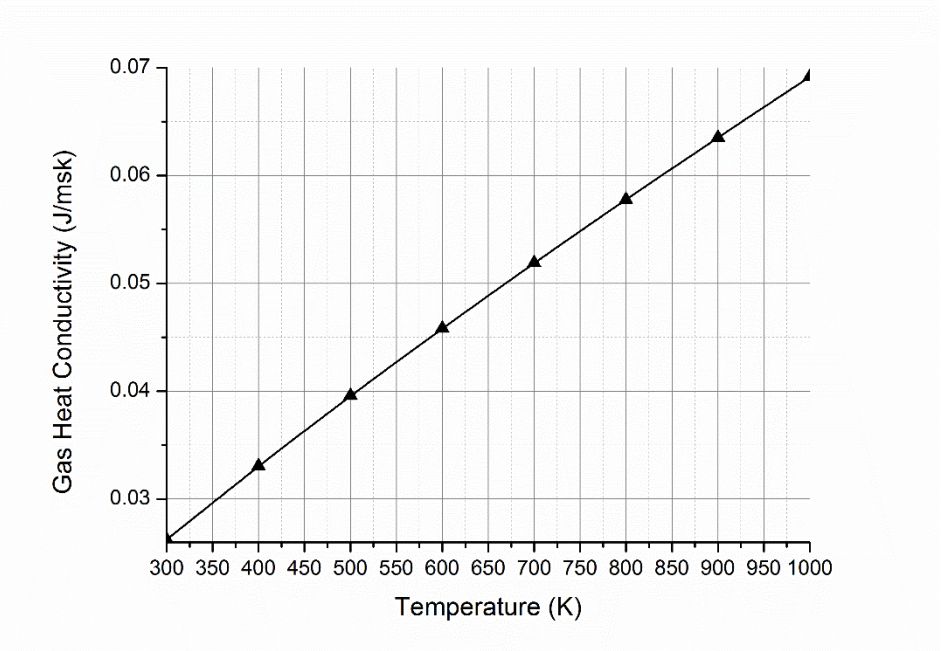

Figure 3.3: Heat conductivity of the exhaust gas

From equation (9), it can be observed that the heat conductivity of the exhaust gas is a function of gas temperature. Figure 3.3 shows the heat conductivity of the exhaust gas under different exhaust gas temperature values.

We assume an asymptotic (constant) Nu for simulation purposes. The channel cross-section is assumed to be close to a square geometry, and correspondingly a value of Nu = 3 (2.98 for square channels) is chosen [28] [65].

D_h is the characteristic length of the gas/solid interaction and is calculated by means of equation (10) [66],

$$D_h = \frac{4\varepsilon}{S} \tag{10}$$

where S is the specific area, the surface area of the substrate per converter volume. S can be determined by means of equation (10).

$$S = \frac{4\times(D-w_1)}{D^2} \tag{11}$$

The third item on the right side of equation (1) represents the heat release from the reactions [67]. r_j stands for the reaction rate of the jth reaction. Δh_j is the enthalpy exchanging expression, which is given in equation (12),

$$\Delta h_j = \sum \eta H_{product} - \sum \eta H_{reactant} \tag{12}$$

where η stands for the stoichiometric number of the species during the reaction, and H is the enthalpy of the species. Enthalpy is calculated as follows [68]:

$$H_i = RT_s\left(-a_1 T_s^{-2} + \frac{a_2 \ln T_s}{T_s} + a_3 + \frac{a_4 T_s}{2} + \frac{a_5 T_s^2}{3} + \frac{a_6 T_s^3}{4} + \frac{a_7 T_s^4}{5} + \frac{b}{T_s}\right) \quad (13)$$

In equation (13), the gas constant R is 8.314, and i=species. The values of the specific heat coefficient a_1~a_7 and the enthalpy constant b are provided in Appendix A.

- Gas phase energy conservation:

$$\varepsilon \rho_s c_{p,g} u_z \frac{\partial T_g}{\partial x} = hS(T_s - T_g) \quad (14)$$

In this thesis, heat convection is the only factor causing the change in temperature in the gas phase. In equation (14), the left side is the overall heat transfer of the gas phase, and the right side is the heat transfer from the solid phase to the gas phase. The gas specific heat is calculated as follows:

$$c_{p,g} = \sum_{i=1}^{n} x_{g,i} M_i c_{p,i} \quad i = \text{species} \quad (15)$$

where $x_{g,i}$ is the ith species mole fraction, $c_{p,i}$ is the specific heat of the ith species, and M_i is the molar mass of the ith species. The calculation of $c_{p,i}$ is given as follows:

$$c_{p,i} = R(a_1 T_g^{-2} + a_2 T_g^{-1} + a_3 + a_4 T_g^1 + a_5 T_g^2 + a_6 T_g^3 + a_7 T_g^4) \quad (16)$$

- Species mass conservation:

$$\frac{w}{A}\frac{\partial x_{g,i}}{\partial x} = -k_{m,i} S(x_{g,i} - x_{s,i}) = \sum_{j=1}^{n_{rct}} \eta r_j \quad (17)$$

In equation (17), the left side is the overall change in mass of the ith species in the gas phase, which is equal to the mass of the ith species involved in the reactions on the right side of the equation. η is the stoichiometric coefficient and $x_{g,i}$ is the species mole fraction. The mass transfer coefficient is calculated by means of the equation below.

$$k_{m,i} = \frac{Sh}{D_h}(c_g D_{i,m}) \quad (18)$$

In equation (18), the Sherwood number $\mathrm{Sh} = \mathrm{Nu} = 3$ according to the model of Ramanathan and Sharma [28]. The mass diffusivity $D_{i,m}$ is given by the equation below,

$$c_g D_{i,m} = \frac{3.85\times10^{-5} T_g^{0.75} \sqrt{\frac{1}{M_i}+\frac{1}{M_{N_2}}}}{(\sqrt[3]{\Sigma_i}+\sqrt[3]{\Sigma_{N_2}})^3} \tag{19}$$

where Σ_i is the diffusion volume of the species.

3.1.3 Reaction kinetics of the high-fidelity model

The high-fidelity TWC converter model simulates the oxidation of CO, HC and the reduction of NO. The reactions and species of the TWC converter are complicated. Typically, hundreds of reactions occur in a converter, depending on the exhaust gas and wash-coat compositions and the temperature. For the most part, only reactions concerning the elimination of noxious emissions are of interest, including the oxidation of CO and HC, the reduction of NO, and the oxygen storage reactions. Some research [34][37] on catalytic converter modelling has concluded that propene (C_3H_6) and propane (C_3H_8) are sufficient to represent the HC in the exhaust gas of the gasoline engine. Hence, in the high-fidelity TWC converter model used in this study, C_3H_6 and C_3H_8 are selected as the representative HCs in the TWC converter, which reduces the number of differential equations to be solved and improves the speed of the model. The reaction set presented by Rao et al. [35] and Ramanathan and Sharma [28] can adequately model the chemical mechanism inside the TWC converter. Therefore, the reactions and reaction kinetics of the high-fidelity model in

the present study are directly adopted from the models of Rao et al. [35] and Ramanathan and Sharma [28]. The high-fidelity model simulates 15 reactions, as shown in Table 3.2.

Table 3.2: Reactions inside the converter that are considered

#	Reactant	Products
1	$CO + 0.5O_2$	CO_2
2	$C_3H_6 + 4.5O_2$	$3CO_2 + 3H_2O$
3	$C_3H_8 + 5O_2$	$3CO_2 + 4H_2O$
4	$H_2 + 0.5O_2$	H_2O
5	$CO + NO$	$CO_2 + 0.5N_2$
6	$C_3H_6 + 9NO$	$3CO_2 + 3H_2O + 4.5N_2$
7	$H_2 + NO$	$0.5N_2 + H_2O$
8	$CO + H_2O$	$CO_2 + H_2$
9	$C_3H_6 + 3H_2O$	$3CO + 6H_2$
10	$2Ce_2O_3 + O_2$	$4CeO_2$
11	$Ce_2O_3 + NO$	$2CeO_2 + 0.5N_2$
12	$CO + 2CeO_2$	$Ce_2O_3 + CO_2$
13	$C_3H_6 + 12CeO_2$	$6Ce_2O_3 + 3CO + 3H_2O$
14	$C_3H_8 + 14CeO_2$	$7Ce_2O_3 + 3CO + 4H_2O$
15	$H_2 + 2CeO_2$	$Ce_2O_3 + H_2O$

Oxidation and reduction reactions

Reactions 1–7 in Table 3.2 are the oxidation and reduction reactions of CO, HC, and NO. The reaction rates of reactions 1–7 are given in (20) [69],

$$r_j = k_i c_{reactant1} c_{reactant2} \quad (20)$$

where $c_{reactant}$ is the concentration of the reactants, and k_j is the reaction rate parameter of the jth reaction. The rate expressions are expressed in terms of the species concentrations in the solid phase, which are related to the mole fractions as

$$c_{s,i} = \frac{p}{R_g T_s} x_{s,i} \quad (21)$$

The purpose of the reaction kinetic model is to calculate the reaction rate parameter k_i. The reaction rate parameter is calculated according to the Langmuir-Hinshelwood mechanism, which is widely used in research on surface reactions.

According to the Langmuir-Hinshelwood mechanism, the molecules of the reactants are first adsorbed into the wash-coat, and then chemical reactions occur as a result of the effective collisions of reactant molecules. Therefore, the reaction rate coefficients are calculated according to three factors: number of collisions, number of effective collisions, and adsorption rates of the molecules [70][71].

The reaction rate coefficient expressions are given in equation (22),

$$k_i = A_i \exp(-E_i/RT)/G \quad (22)$$

where A_i is the pre-exponent multiplier, which expresses the probability of the collisions; E_i is the activation energy, which represents the possibility of effective collisions; and G evaluates the adsorption rate of gas reactant from the gas phase to the solid phase.

The inhibition factor G is calculated using the methods and parameters from the open lectures [35], and the equations are given as follows,

$$G = (1 + K_1 c_{CO} + K_2 c_{C3H6})^2 (1 + K_3 c_{CO}^2 c_{C3H6}^2)(1 + K_4 c_{NO}) \quad (23)$$

$$K_i = k_{i,G} \exp\left(-E_{i,G}/T\right) \; i = 1 \sim 4$$

where $k_{i,G}$ and $E_{i,G}$ are the adsorption constant and adsorption heat, respectively. The values of these two sets of parameters are the experience values from the open lectures [35], as shown in Table 3.3.

Table 3.3: Adsorption constant and adsorption heat values

i	$k_{i,G}$	$E_{i,G}$
1	4.314	-485
2	1.289	166

3	2.147E-4	-10163
4	8.699E5	3685

Water-gas shift reactions

Reactions 8 and 9 are water-gas shift reactions. The reaction rates are given by equations (24) and (25).

$$r_8 = \frac{A_8}{G}\exp(-\frac{E_8}{RT_s})(C_{CO}C_{H_2O} - \frac{C_{H_2}C_{CO_2}}{K_{WGS}}) \quad (24)$$

$$r_9 = \frac{A_9}{G}\exp(\frac{E_9}{RT_s})C_{C_3H_6}C_{H_2O} \quad (25)$$

The equilibrium constant is given by:

$$K_{WGS} = \exp(-\frac{\Delta G_{WGS}}{RT_s}) \quad (26)$$

The reaction free energy of the water-gas shift reaction is computed using data from the Chemical Properties Handbook [72] by means of equation

$$\Delta G_{WGS} = -4.1034 \times 10^4 + 44.19 T_s - 5.553 \times 10^{-3} T_s^2 \quad (27)$$

Normally, the engine-out measurement includes the concentration of exhaust gas (CO, HC, NO, O_2, CO_2). However, the water and hydrogen mole fraction is also required to calculate the water-gas shift reaction rates. These are calculated using the empirical formulae from [28][73][74]:

$$[H_2] = \frac{1.85}{2} \frac{[CO]([CO]+[CO_2])}{[CO]+[CO_2]/0.285} \quad (28)$$

$$[H_2O] = \frac{1.85}{2} \frac{[CO_2]([CO]+[CO_2])}{0.285[CO]+[CO_2]} \quad (29)$$

Oxygen storage reaction

Reactions 10–15 are oxygen storage reactions. The reaction rates of the oxygen storage reactions are given below.

$$r_i = A_i \exp(-\frac{E_i}{RT_s}) C_j \Psi \quad (30)$$

$$\Psi = \begin{cases} 1-\theta & i = 10, 11 \\ \theta & i = 12-15 \end{cases}$$

The surface coverage θ, as shown in equation (31), is the ratio of oxygen storage in the higher oxidation state compared to the total available oxygen storage capacity, which is effectively the fraction of cerium that is fully oxidized.

$$\theta = \frac{\text{mole of } CeO_2}{\text{mole of } CeO_2 + 2 \times \text{mole of } Ce_2O_3} \tag{31}$$

θ can be calculated as a function of solid temperature, concentration, and surface coverage (θ).

$$\frac{d\theta}{dt} = (4r_{10} + 2r_{11}) - (2r_{12} + 12r_{13} + 14r_{14} + 2r_{15}) \tag{32}$$

Cerium is more stable in its oxidized state. Therefore, θ is taken as the value of 1 when t=0.

For all 15 reactions, the pre-exponent multiplier A_i and activation energy E_i are the parameters that need to be tuned. In this thesis, these parameters are tuned manually during the driving cycle simulation. The accuracy obtained is sufficient for the control system and the state estimations. The initial values of the parameters are directly adopted from Ramanathan and Sharma [28] and are given in Table 3.4.

Table 3.4: Initial pre-exponent multiplier and activation energy values

Pre-exponent multiplier	Default values	Activation energy	Default values
A_1	5.542×10^{13}	E_1	121450
A_2	1.917×10^{15}	E_2	129530
A_3	6.404×10^{15}	E_3	165160
A_4	1.814×10^{15}	E_4	111450
A_5	2.857×10^{9}	E_5	52374
A_6	2.994×10^{11}	E_6	80063
A_7	7.88×10^{10}	E_7	69237
A_8	1.8×10^{5}	E_8	56720
A_9	1.23×10^{5}	E_9	81920
A_{10}	2.943	E_{10}	5296
A_{11}	792	E_{11}	25101
A_{12}	0.1824	E_{12}	31768
A_{13}	13.57	E_{13}	39070
A_{14}	17.7	E_{14}	39680
A_{15}	2.845	E_{15}	31768

3.2 Simulation of the high-fidelity TWC converter model

The high-fidelity model is simulated using the professional software GT-SUITE, which is designed to build vehicle-related models, including engine models, emission systems models, and vehicle models [75]. The physical specifications of the high-fidelity model are determined according to a TWC converter in a testing bench. The simulation includes two parts, a constant inlet simulation and a driving cycle simulation.

3.2.1 Dimensions of the TWC converter

The geometric parameters of the converter, which can be set in GT-SUITE when building the model, are listed below in Table 3.5.

Table 3.5: Geometric parameters of the converter

Parameters	Values	Units
PGM active surface site density	0.35	$mole/m^3$
Cerium active surface site density	50	$mole/m^3$
Cerium atomic weight	140	-
PGM atomic weight	195	-
Channel geometry	Square	-
Frontal area (A)	0.0082	m^2
Length (L)	150	mm
Substrate thickness (w_1)	1.0922×10^{-4}	m
Cell density	1394910	$/m^2$

Cordierite density (ρ_{cor})	1720	kg/m^3
Alumina density (ρ_{ws})	1300	kg/m^3
Cordierite specific heat (c_{cor})	Appendix B	$J/kg \cdot K$
Alumina specific heat (c_{al})	1000	$J/kg \cdot K$

3.2.2 Setup of the high-fidelity TWC converter model

GT-SUITE v7.4 provides a visual modelling method by assembling the model modules. The model can be used to simulate the performance of a TWC converter. The modules of the high-fidelity model are shown in Figure 3.4.

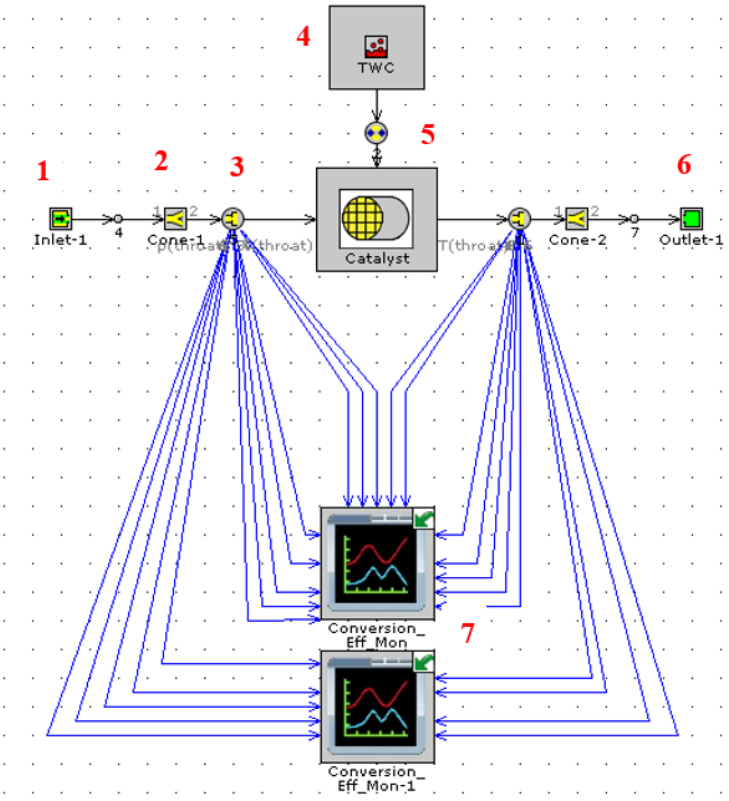

Figure 3.4: High-fidelity GT-SUITE model

Component 1 is the inlet module. The initial inlet includes the inlet gas volume flow rate, initial gas mole fraction, and inlet temperature.

Component 2 is the cone flow split module. The flow split cones are required in the model map to enable transit from a single inlet tile pipe to the multiple channel geometry of the catalytic converter. The geometry of the split is a truncated cone, which essentially expands from a diameter equal to the inlet pipe to a diameter equal to the front face of the catalyst brick.

Component 3 is a throat. Here, the throat is used as a nozzle for measuring the input and output gas information of the converter.

Component 4 is the module of the surface reaction mechanism inside the catalytic converter. The reactant, the product, and the reaction rate parameters of the reactions are set in this module.

Component 5 is the converter monolith. In this module, geometry and heat transfer parameters are defined. The dimensions of the converter match those of the real converter mentioned in Chapter 3. The square channel geometries provided in Table 3.1 are also set in this module.

Heat transfer through the catalyst substrate wall is modelled using a one-dimensional conduction object that considers only axial temperature gradients in the substrate. The discretization length of the converter is 5mm, and the time step size is 1s. The determination

of the grid and time steps are presented in Appendix D. They have been proven to have a negligible impact on the results. The outside heat transfer flag of the converter is turned off in line with the assumptions.

3.2.3 Constant inlet warming-up analysis

The main heat sources causing the rise in the converter's temperature are the heat convection from the gas to the solid and the heat release from the chemical reactions. In this section, a qualitative analysis of the warming-up process caused by these two factors is conducted to determine the converter's warming-up mechanism.

In order to determine the influence of the gas-solid heat convection on the warming-up process, the TWC converter's warming-up times under different inlet gas volume rates are compared.

As mentioned in Chapter 3.2.2, the modelling resolution of the high-fidelity converter model is 30 and the time steps are 1s in length. During the simulation, a total of 10 points along the converter are taken as the sampling points, as shown in Figure 3.5.

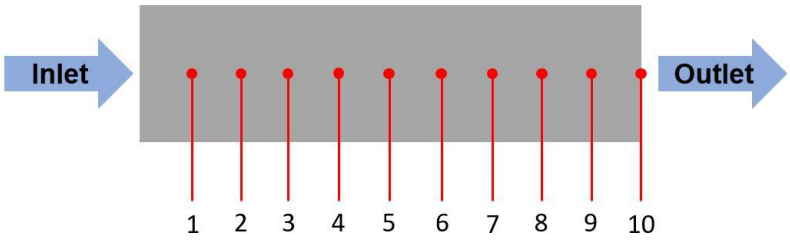

Figure 3.5: The temperature sampling points

The constant inlet data consist of three different inlet volume flow rates of 0.8, 1.0, and 1.2 m^3/min with a constant TWC inlet temperature of 500 °C (773.5 K). Reactions inside the converter model during the warming-up analysis are turned off. The constant inlet simulation duration is 200s.

The temperature of each measurement point under different inlet conditions is shown in Figure 3.6 below.

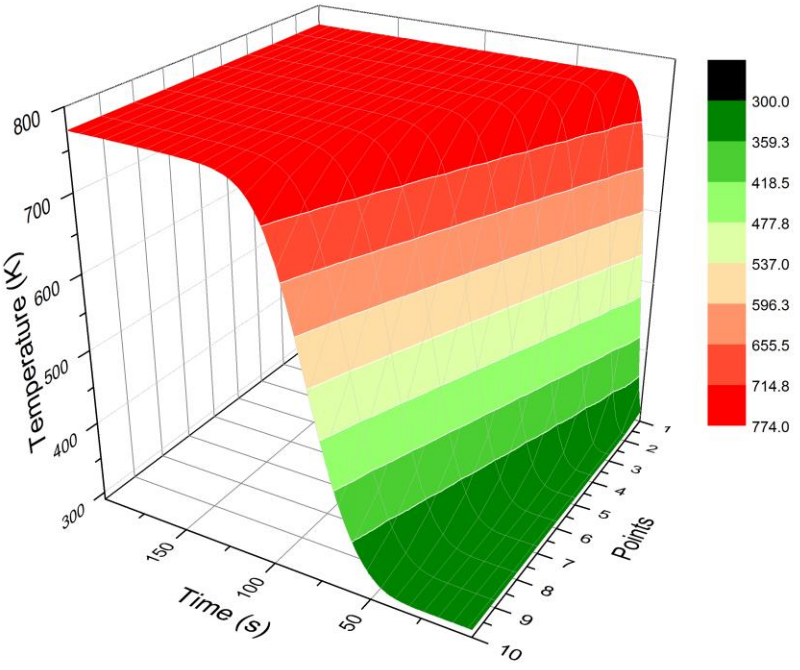

Figure 3.6: Converter temperature during the warming-up process at a volume rate of 0.8

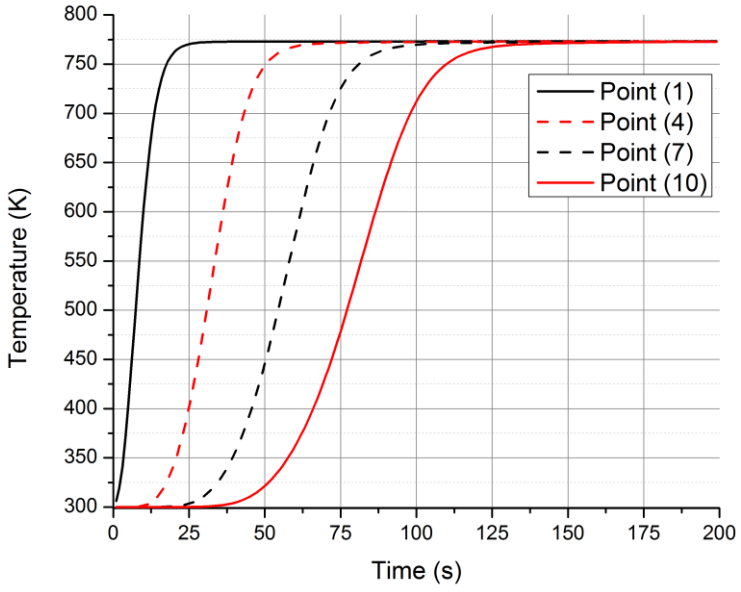

Figure 3.7: Warming-up time of selected points at a volume rate of 0.8

Figure 3.6 and Figure 3.7 show the converter temperatures for an inlet volume of 0.8 m^3/min. The time taken for the temperature to increase from 300K to 774K is approximately 75s at the middle of the converter (point 5) and 140s at the outlet (point 10).

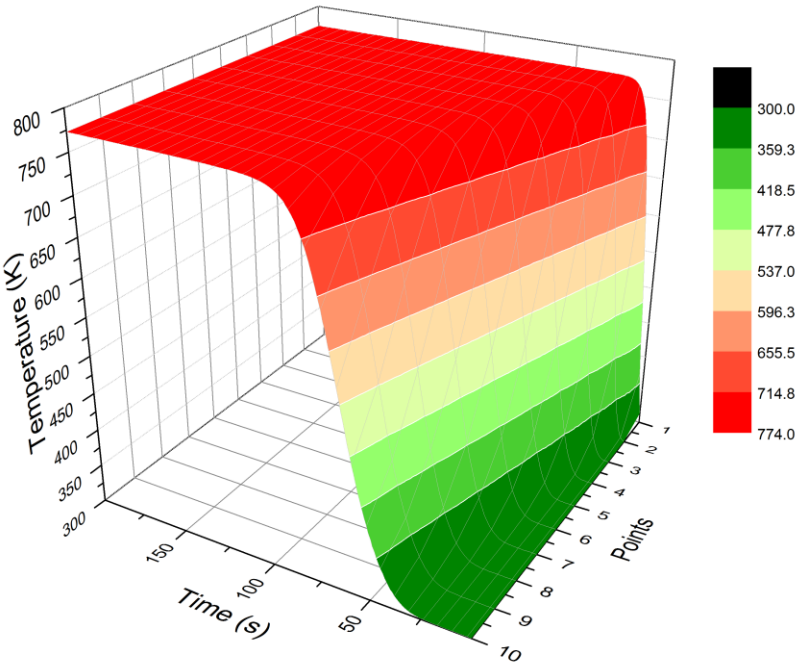

Figure 3.8: Converter temperature during the warming-up process at a volume rate of 1.0

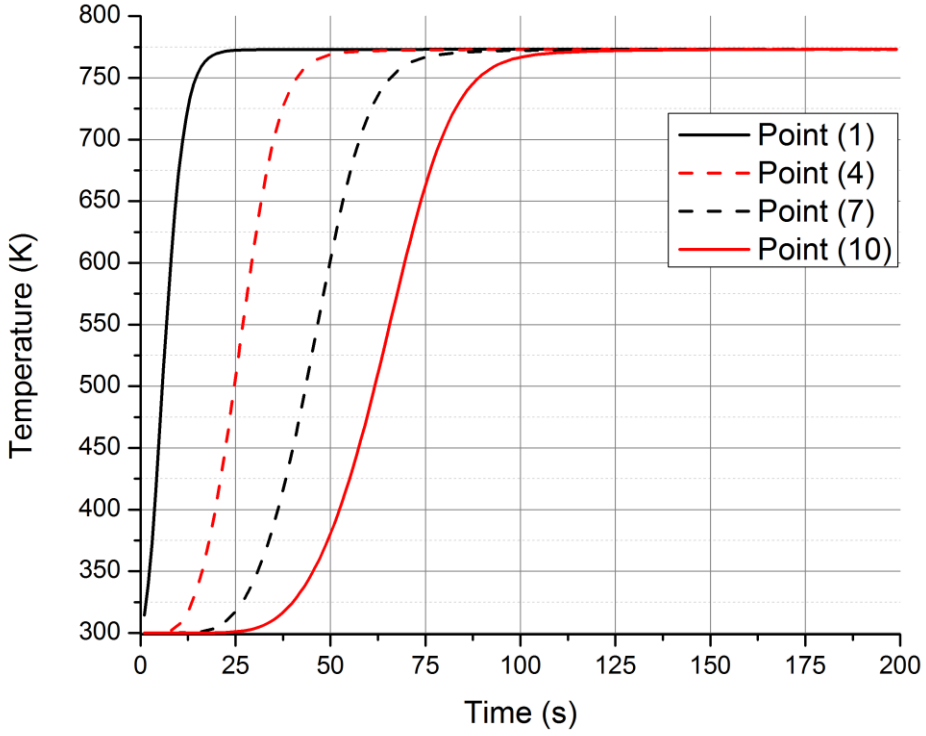

Figure 3.9: Warming-up time of selected points at a volume rate of 1.0

Figure 3.8 and Figure 3.9 show the converter temperatures for an inlet volume of 1.0 m^3/min. The time taken for the temperature to increase from 300K to 774K is approximately 60s at the middle of the converter (point 5) and 110s at the outlet (point 10).

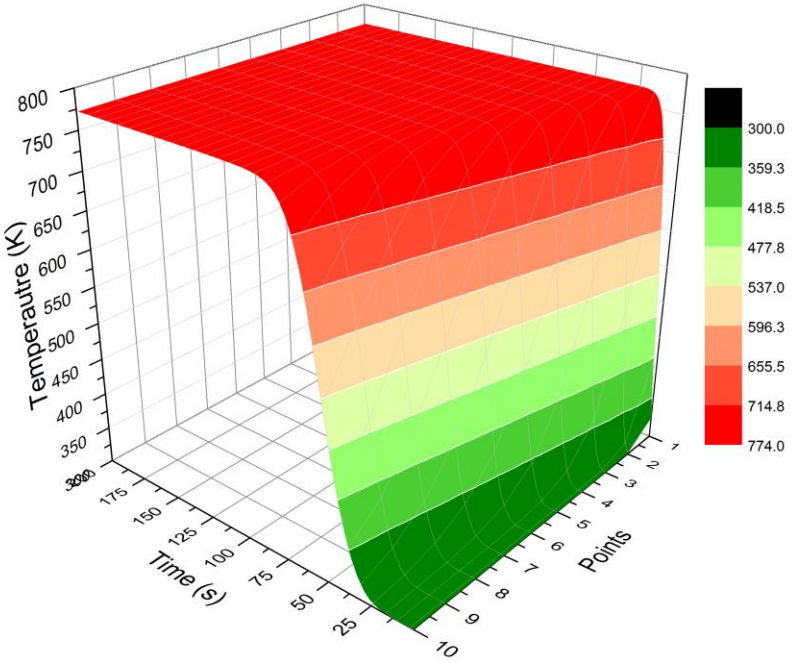

Figure 3.10: Converter temperature during the warming-up process at a volume rate of 1.2

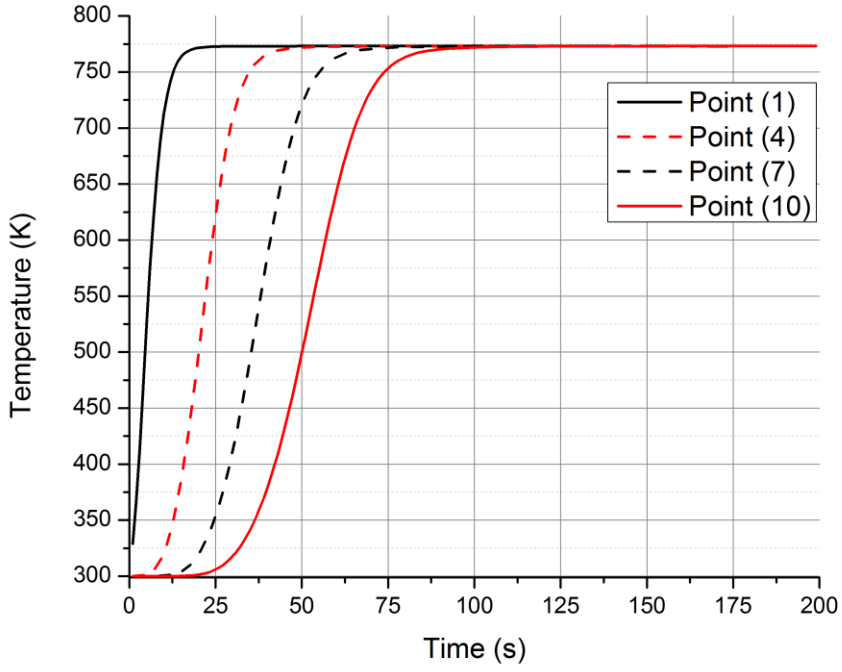

Figure 3.11: Warming-up time of selected points at a volume rate of 1.2

Figure 3.10 and Figure 3.11 show the converter temperatures for an inlet volume of 1.2 m^3/min. The time taken for the temperature to increase from 300K to 774K is approximately 50s at the middle of the converter (point 5) and 80s at the outlet (point 10).

Direct comparisons of the temperature increase times at the middle (point 5) and the outlet (point 10) of the converter are provided in Figure 3.12 and Figure 3.13, respectively.

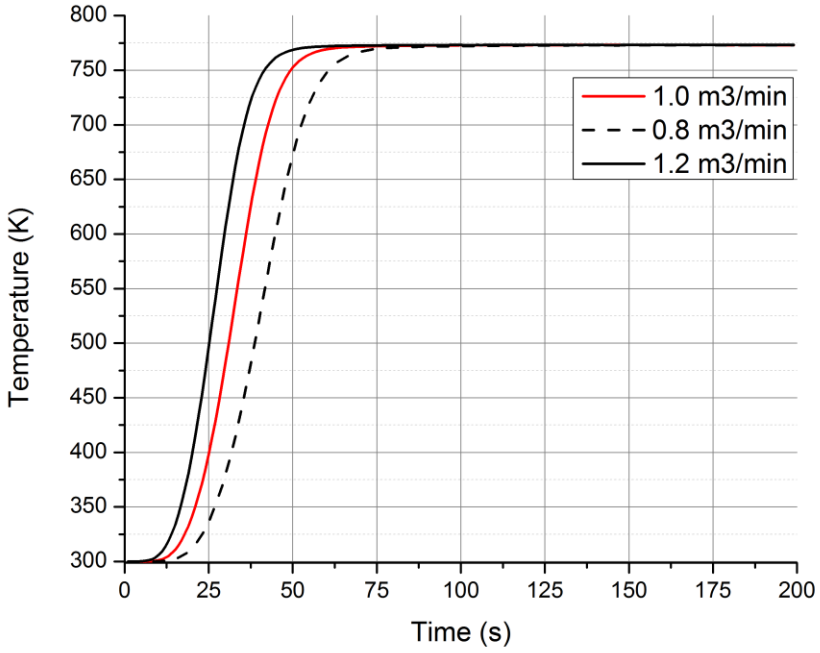

Figure 3.12: Comparison of temperature increase times at middle point (point 5)

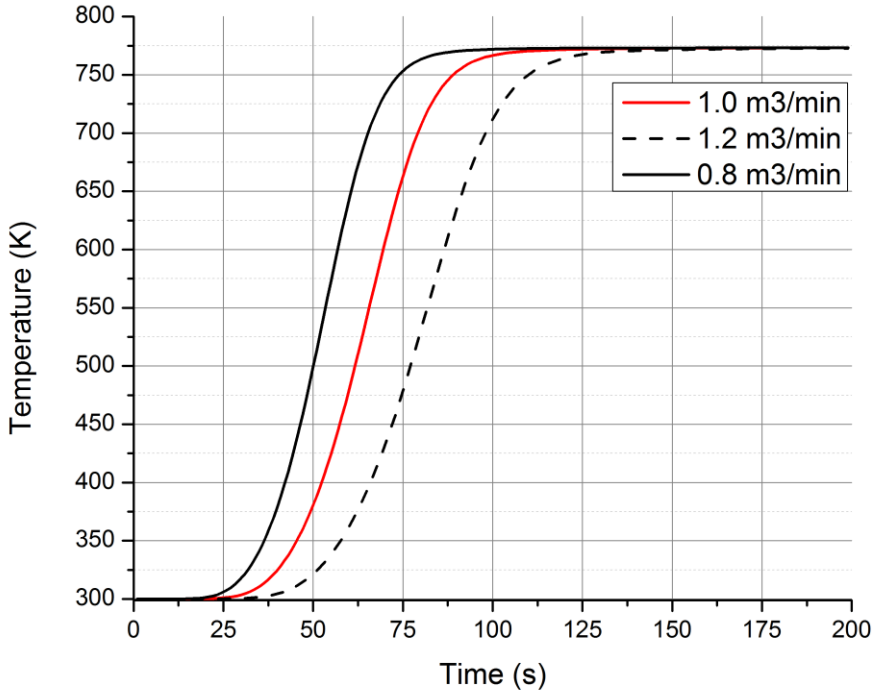

Figure 3.13: Comparison of temperature increase times at outlet point (point 10)

The comparison of the results indicates that a higher inlet gas volume rate reduces the TWC converter's warming-up time.

In addition to the heat convection from the gas to the solid, the heat release from the TWC converter's internal reactions is an alternative factor causing the temperature increase. A separate analysis of the internal chemical reactions' influence on the converter's temperature increase is conducted. The inlet temperature is kept constant at 774K. The inlet volume flow rate is 1.0 m^3/min. The inlet pollutant species concentrations are set to zero, average and high to control the variable reaction rate. The values of the species

concentration are all chosen from the experimental tests. The temperature increase maps are compared under the different inlet concentrations.

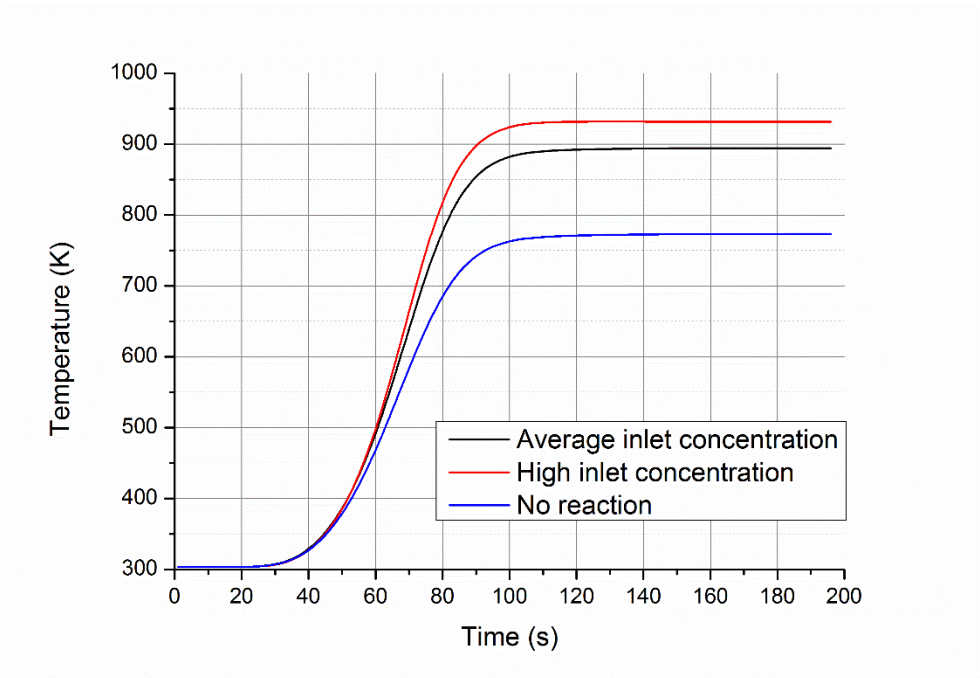

Figure 3.14: Outlet temperature under different species inlet concentrations

Figure 3.14 shows the outlet temperature of the converter under different inlet species concentrations. The higher reaction rate can lead to a higher outlet temperature and allow the TWC converter to warm up faster. As illustrated in Figure 3.14, the outlet temperature of the converter is 774K (without reactions), 890K (average inlet concentration), and 930K (high inlet concentration). The energy levels required to heat the converter to the specific temperatures are calculated to be 217,823.36 J, 271,130.35 J and 289,512.06 J, respectively.

Table 3.6: Energy required for temperature increases

Outlet Temperature	774K	890K	930K
Inlet concentration	Zero	Average	High
Energy required	217823.36 J	271130.35 J	289512.06 J
Energy rise caused by reactions	0%	24.47%	32.91%

Table 3.6 shows the soxxurces and the amount of the energy required for the temperature increase at an inlet temperature of 774K with zero, average and high inlet concentrations. For an average inlet concentration, the outlet temperature is 890K and 271,130.35J energy is required. For a high inlet concentration, the outlet temperature is 930K and 289,512.06J energy is required. By comparing the outlet temperature of the converter and the energy required to heat it, it can be observed that the increase in energy caused by the chemical reactions is approximately 30%. Thus, it can be concluded that for the warming-up process, more energy is provided by the gas-solid heat convection than by the chemical reactions.

3.2.4 Constant inlet chemical reaction simulation

During the constant inlet simulation, the chemical analysis is performed by comparing conversion efficiency under various inlet volume flow rates and temperatures. The data for the chemical analysis consists of CO, HC and NO inlet and outlet concentration at five inlet temperature values ranging from 400 °C to 600 °C at three different inlet volume flow rates

of 0.8, 1.0 and 1.2 m^3/min. The reaction rate parameters are set to the initial values shown in Table 3.4.

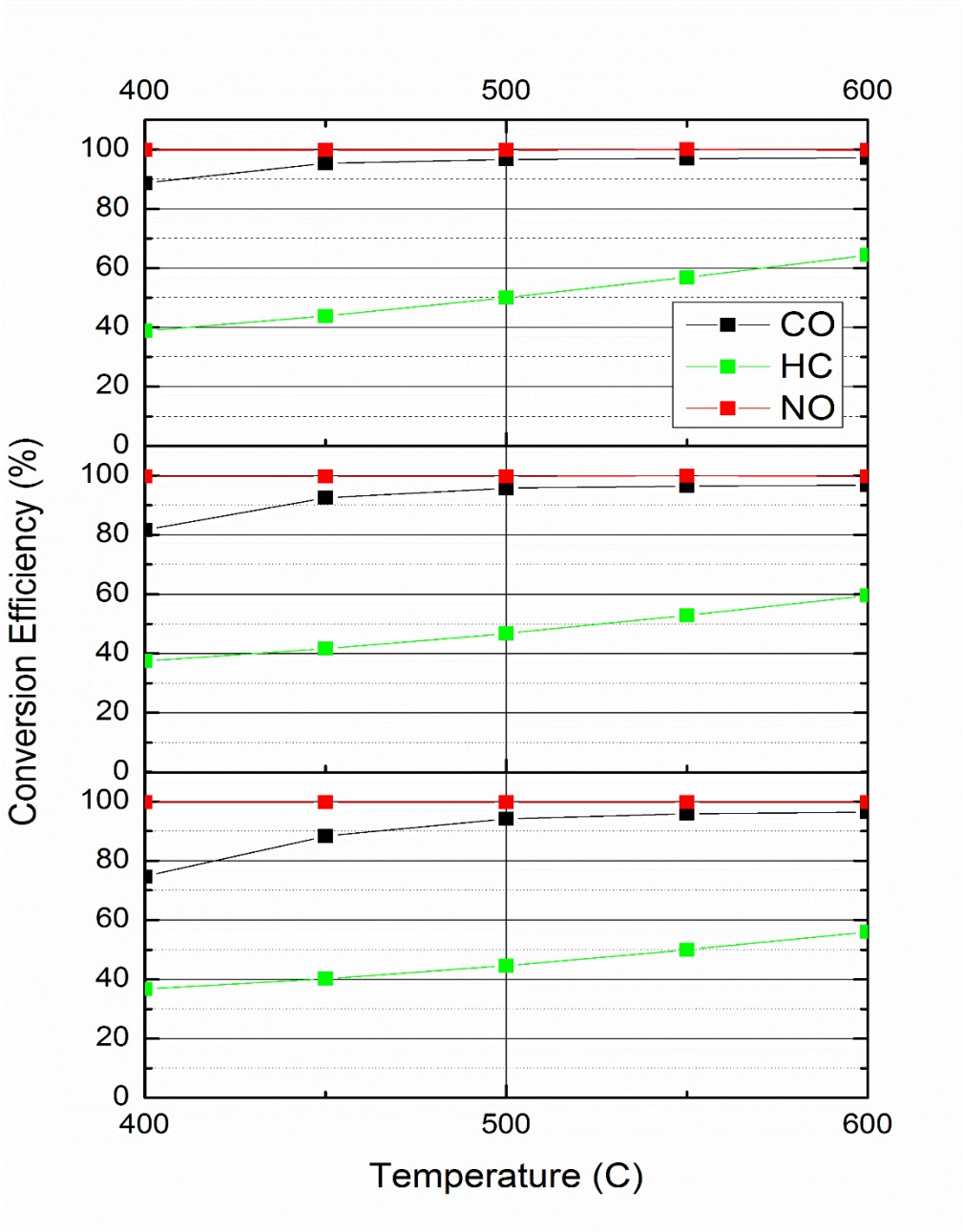

Figure 3.15: Conversion efficiency at different temperatures from 400 C to 600 C and different inlet volume rates of 0.8, 1.0 and 1.2

Figure 3.15 shows the conversion efficiency of HC, CO and NO under inlet volume flow rates of 0.8, 1.0 and 1.2 m^3/min (from top to bottom). From the general trend of the curves, it can be observed that conversion efficiency increases as the temperature increases and drops as the volume flow rate increases. For an inlet volume flow rate of 0.8 m^3/min, the conversion efficiency of HC is approximately 40% at a temperature of 400 °C and reaches over 60% at a temperature of 600 °C. The conversion efficiency of CO reaches over 90% at a temperature of 450 °C. The conversion efficiency of NO is high. For an inlet volume rate of 1.0 m^3/min, the conversion efficiency of HC is lower than 40% at a temperature of 400 °C and reaches 60% at a temperature of 600 °C. The conversion efficiency of CO reaches over 90% at a temperature of 500 °C. For an inlet volume rate of 1.2 m^3/min, the conversion efficiency of HC is 40% at a temperature of 500 °C and no more than 60% at a temperature of 600 °C. The conversion efficiency of CO reaches over 90% at a temperature of 500 °C.

An additional aim of the constant inlet chemical simulation is to determine the reaction rate parameters, including the pre-exponent multiplier and activation energy parameters. Harsha [76] uses a similar method to determine these parameters by comparing the experimental and simulated conversion efficiencies during the constant inlet simulation. The reaction rate parameters in the present study are tuned during the driving cycle simulation, since the experiment under the constant inlet are absent. The driving cycle simulation method is more complicated and produces more errors, because the reliability of the species mole fraction sensors is reduced under driving cycle conditions.

3.2.5 Driving cycle simulation

The input of the driving cycle simulation is transient emission data from real engine testing. The transient simulation identifies the data of the activation energy and the pre-exponential multiplier parameters for the reactions.

The FTP-72 driving cycle is employed. FTP-72 was developed for emissions testing by the US Environmental Protection Agency (EPA) in the 1970s and is widely used in US federal emissions tests. Vehicle speed over time for the FTP-72 driving cycle is illustrated in Figure 3.16 [77]. The driving cycle specifications are provided in Table 3.7. The driving cycle is divided into two phases: a cold-start phase (0~505s to the left of the red line) and a transient phase. The results from the two phases are analysed in the following sections.

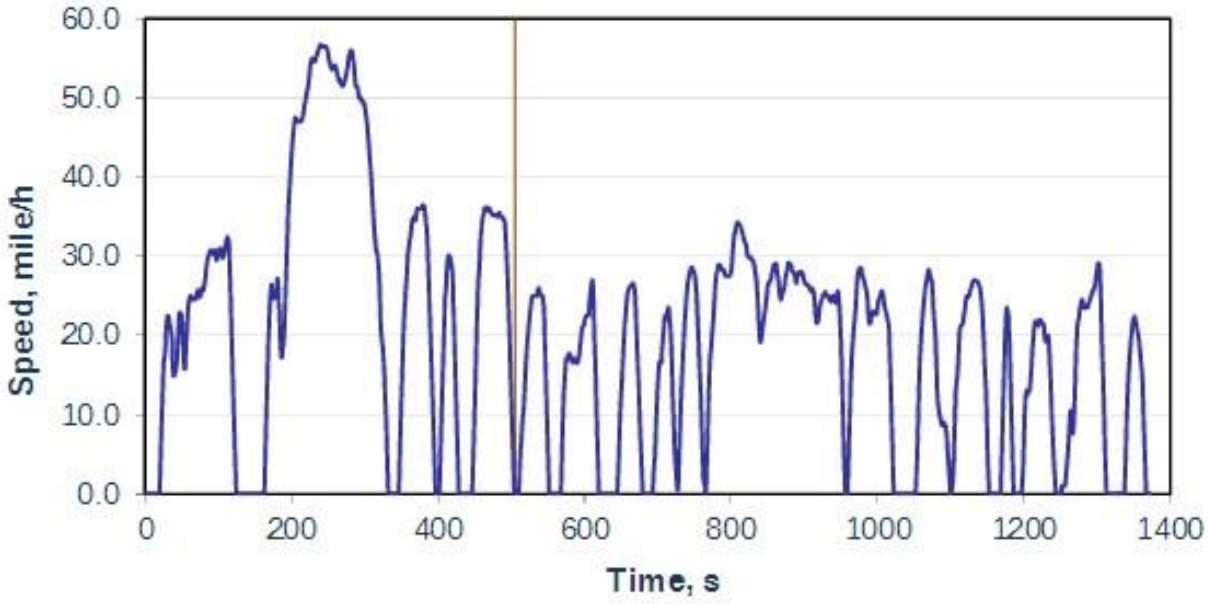

Figure 3.16: Vehicle speed over time for FTP-72 driving cycle

Table 3.7: Specifications of FTP-72 driving cycle

Parameters	Values
Distance travelled	17.7 km (11.04 miles)
Duration	1,372 seconds
Average speed	34.1 km/h (21.2 mph)

The inlet data of the high-fidelity converter model include the gas volume flow rate; the mole fractions of CO, NO, HC, O_2, and CO_2; and the gas phase temperature. The engine providing the pre-catalyst gas is a 3.5L DOHC V6 gasoline engine from a 2010 Ford Edge with an odometer reading of 11,031 miles. The engine's maximum power is 285 HP at 6,500 RPM and its maximum torque is 253 lb·ft at 4,000 RPM. The initial inlet gas volume flow rate is illustrated in Figure 3.17. The inlet gas temperature is shown in Figure 3.18.

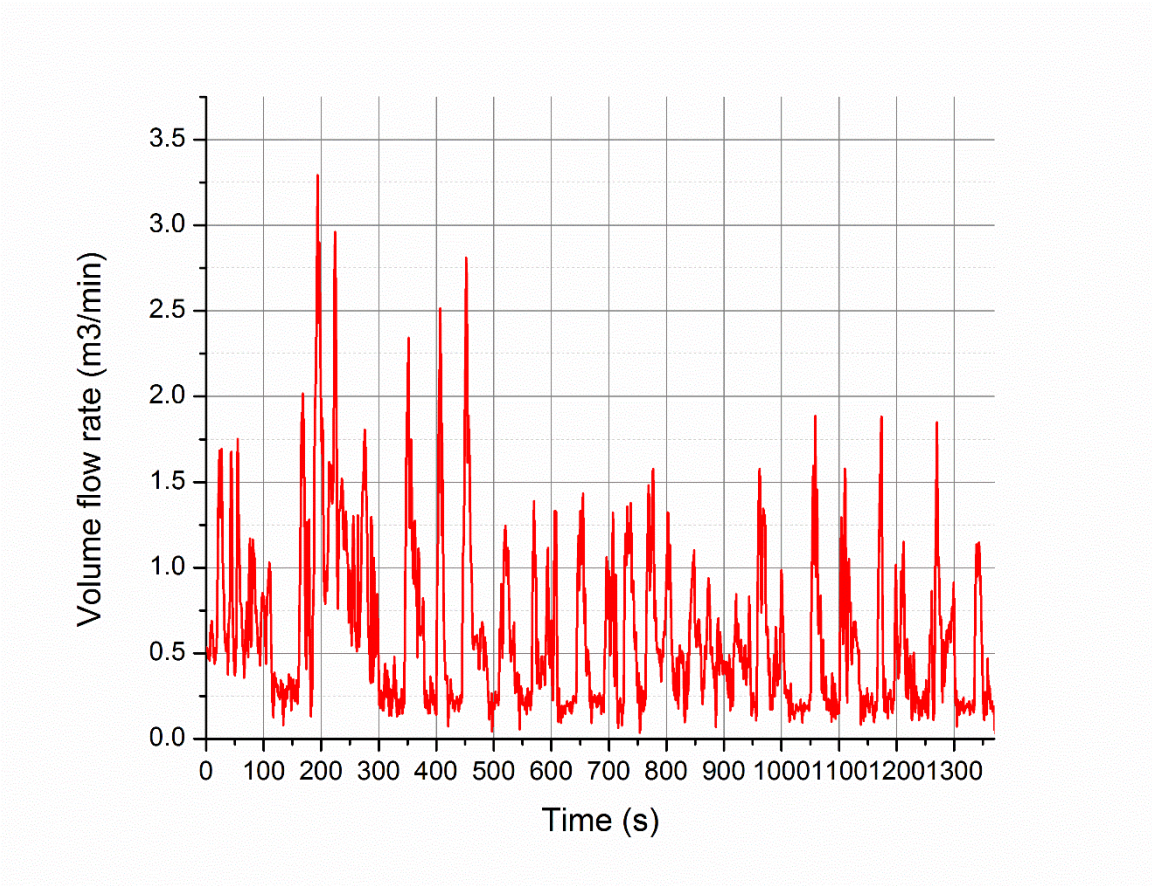

Figure 3.17 Initial inlet gas volume flow rate

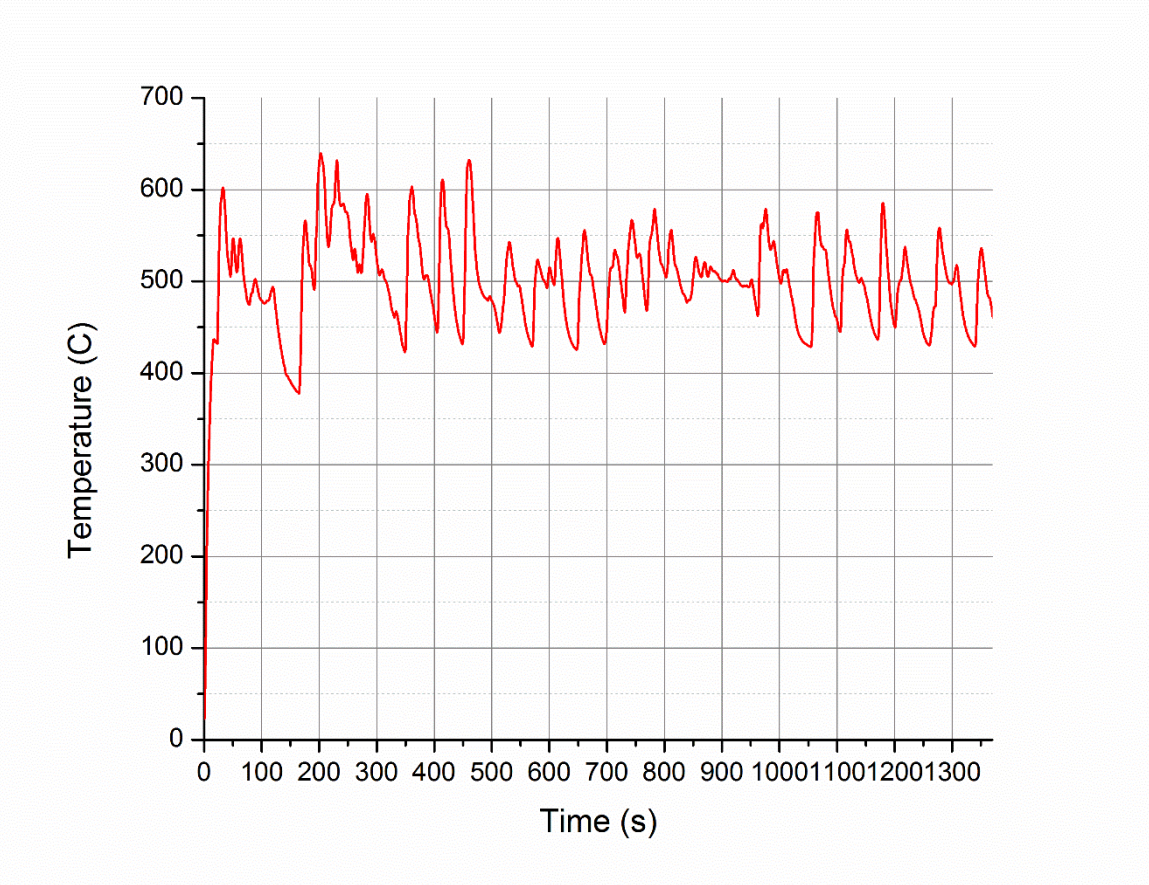

Figure 3.18: Inlet gas temperature

The mole fraction of the pollutant in the inlet gas are shown from Figure 3.19 to Figure 3.21 in units of ppm.

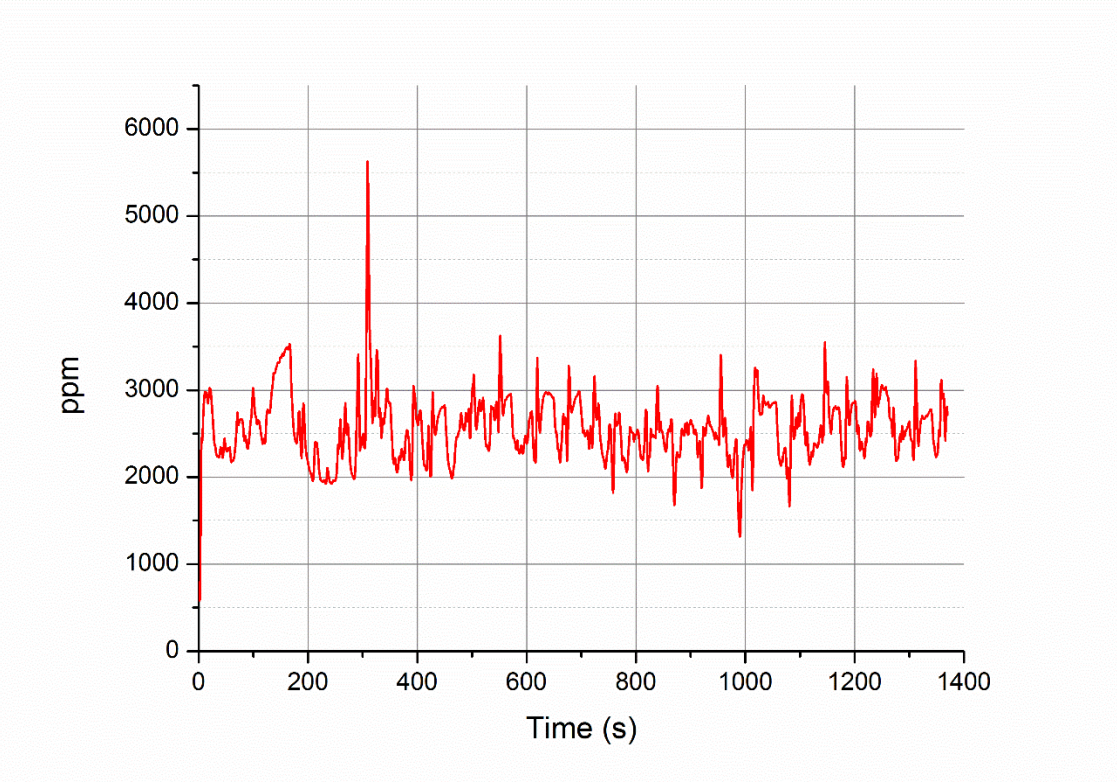

Figure 3.19 Inlet HC mole fraction

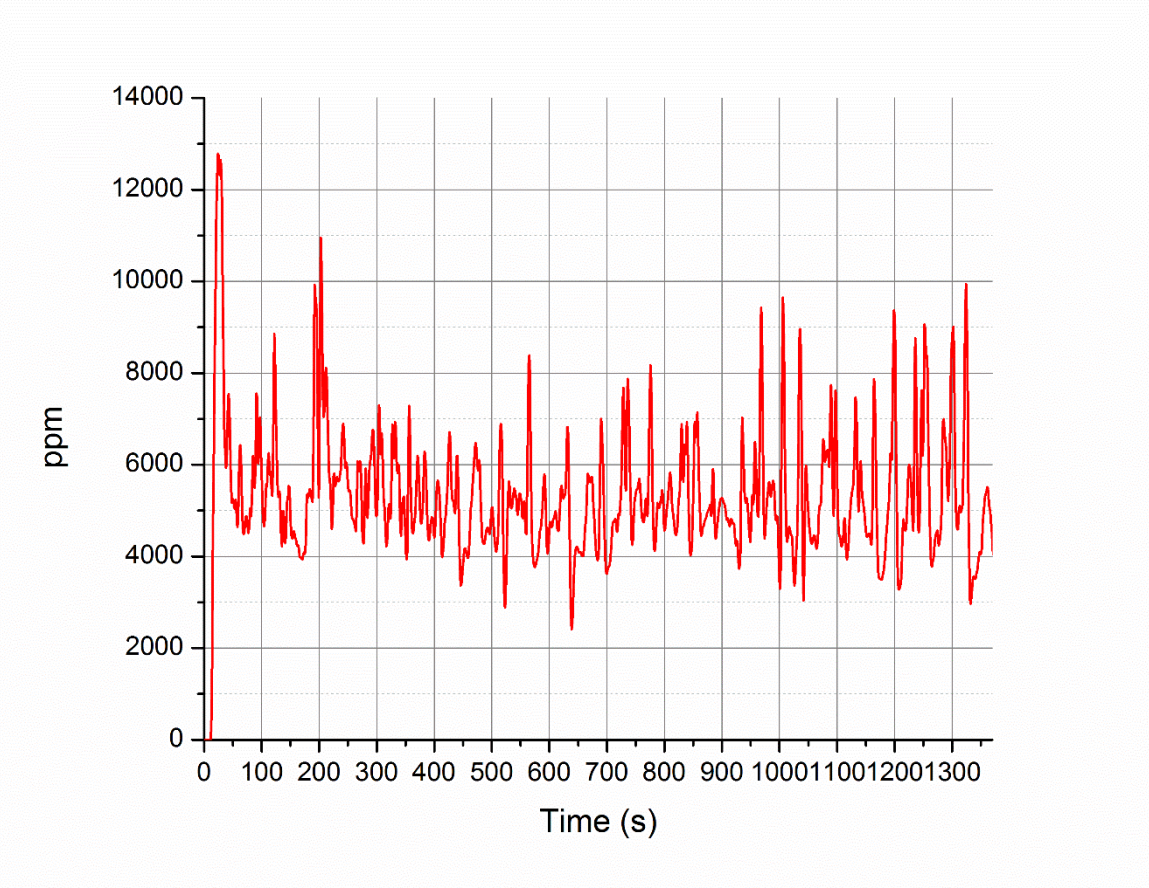

Figure 3.20 Inlet CO mole fraction

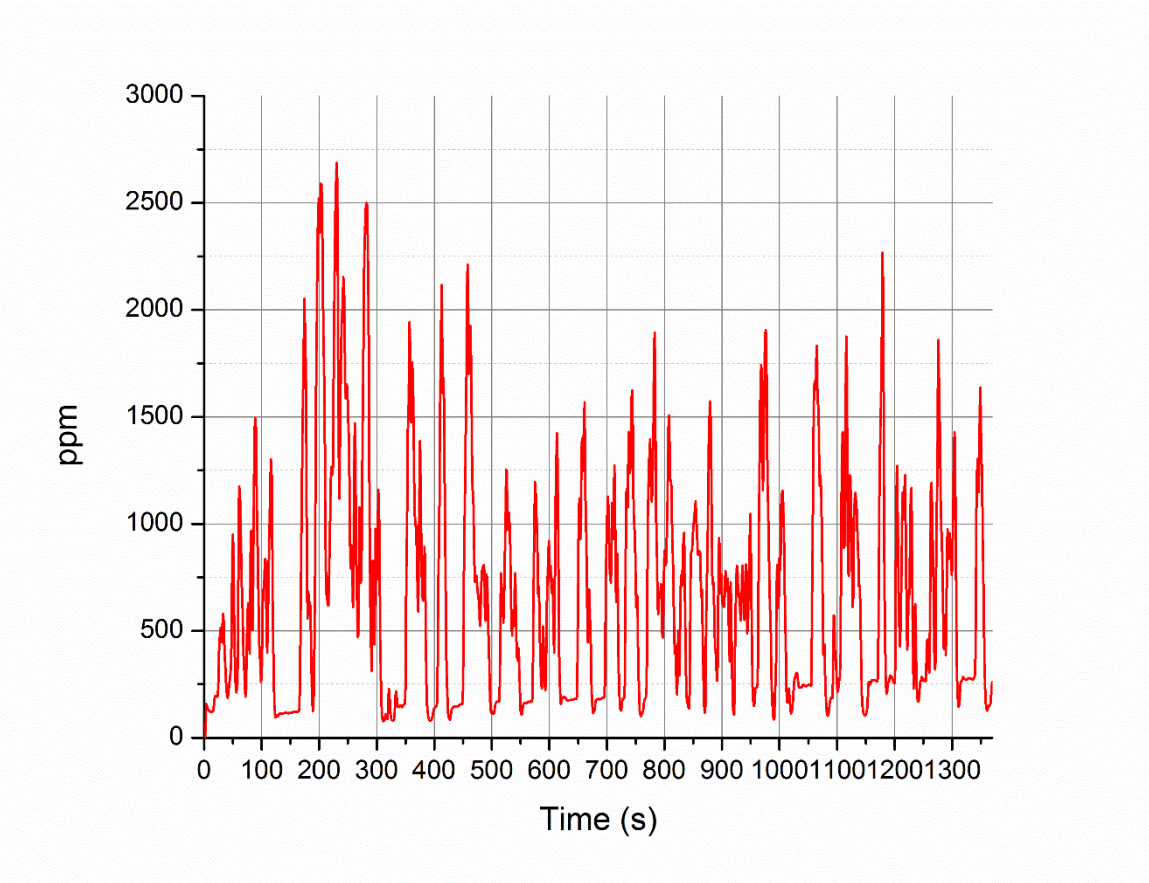

Figure 3.21 Inlet NO mole fraction

Both initial and ambient temperatures are set at 26.85 degrees, which matches the testing conditions of the engine testing bench.

3.2.5.1 Driving cycle chemical simulation results

One of the main purposes of the driving cycle simulation is to tune the reaction rate parameters by minimizing the errors between the experimental and the simulated data.

For the adjustment of the reaction rate parameters, the outlet CO and HC mole fraction results of the high-fidelity model with Ramanathan and Sharma's [28] reaction rate parameter values (initial parameter values shown in Table 3.4) are provided. The results are shown in Figure 3.22 ~ Figure 3.24.

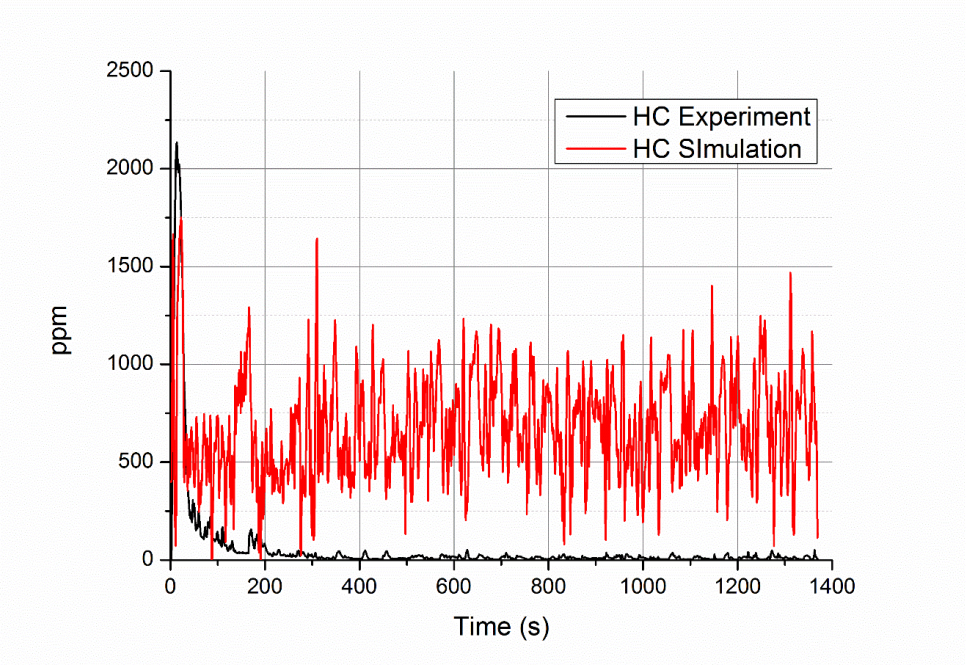

Figure 3.22: Outlet HC mole fraction with Ramanathan and Sharma's parameter values

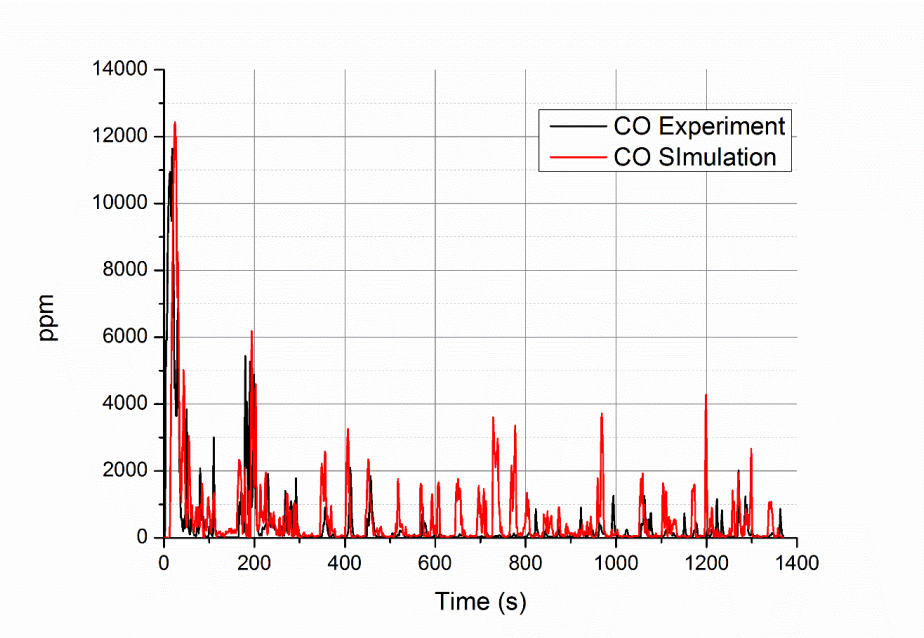

Figure 3.23: Outlet CO mole fraction with Ramanathan and Sharma's parameter values

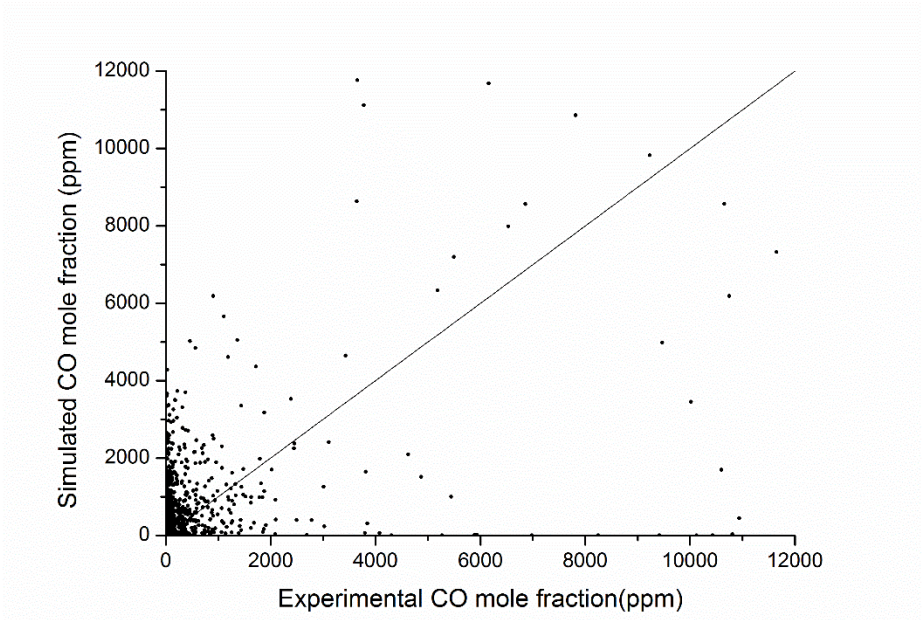

Figure 3.24: Outlet CO mole fraction scatter diagram with Ramanathan and Sharma's parameter values

The high transient of the results makes it hard to detect the difference in mole fraction simply from the line diagram, especially the line diagram of CO output mole fraction shown in Figure 3.23. Therefore, a scatter diagram is made through Figure 3.24. If the model accuracy is high, the points should be located around the line of y=x. From Figure 3.22, Figure 3.23 and Figure 3.24 it can be observed that the model's accuracy when using Ramanathan and Sharma's [28] parameter values is less than satisfactory in the present study case. This is especially true regarding the outlet HC mole fraction, which does not fit the experimental data throughout the driving cycle. And according to the results shown in Figure 3.24 the accuracy of CO mole fraction also has room for improvement, although the difference in mole fraction is kept within a value of 1000 for a large proportion of the points. Therefore, the reaction rate parameter values need to be re-tuned.

The pre-exponent multipliers and activation energy parameters are tuned manually by minimizing the transient outlet error between the measured and simulated data. Across all 30 parameters, the activation energy parameter E_i is kept unchanged, since the catalyst and wash-coat formulations are similar for most TWC converters. The steam reforming and water-gas shift reactions are fairly insensitive to the measured data according to prior research [28]. Therefore, the water-gas shift reaction parameters are not re-tuned. In Ramanathan and Sharma's [28] study, the oxidation reaction rate parameters are tuned initially, followed by the NO reduction reactions and then the oxygen storage reactions. In the present study, the results are accurate enough for the control system once the oxidation and reduction reaction rate parameters have been tuned. Therefore, the re-tuned parameters

are the pre-exponent multipliers of the oxidation and reduction reactions. The values of the tuned parameters are listed in Table 3.8.

Table 3.8: Comparison between Ramanathan and Sharma's parameter values and those in the present study

A_i	Ramanathan and Sharma's value	Value in this study
A_1	5.542×10^{13}	7.542×10^{13}
A_2	1.917×10^{15}	9.83×10^{15}
A_5	2.857×10^{9}	6.45×10^{9}
A_6	2.994×10^{11}	2.65×10^{12}

As illustrated in Table 3.8, the adjustment range of the CO-related reaction parameters (A_1 and A_6) is small, while the adjustment range of the HC-related reaction parameters is relatively large in order to reduce the error of the outlet HC mole fraction. The adjusted parameter values in the present study are within ten times Ramanathan and Sharma's [28] values.

The results of the driving cycle simulation are listed. These results include the transient outlet mole fraction values and the total output amounts.

The results regarding the transient output CO mole fraction are shown in Figure 3.25.

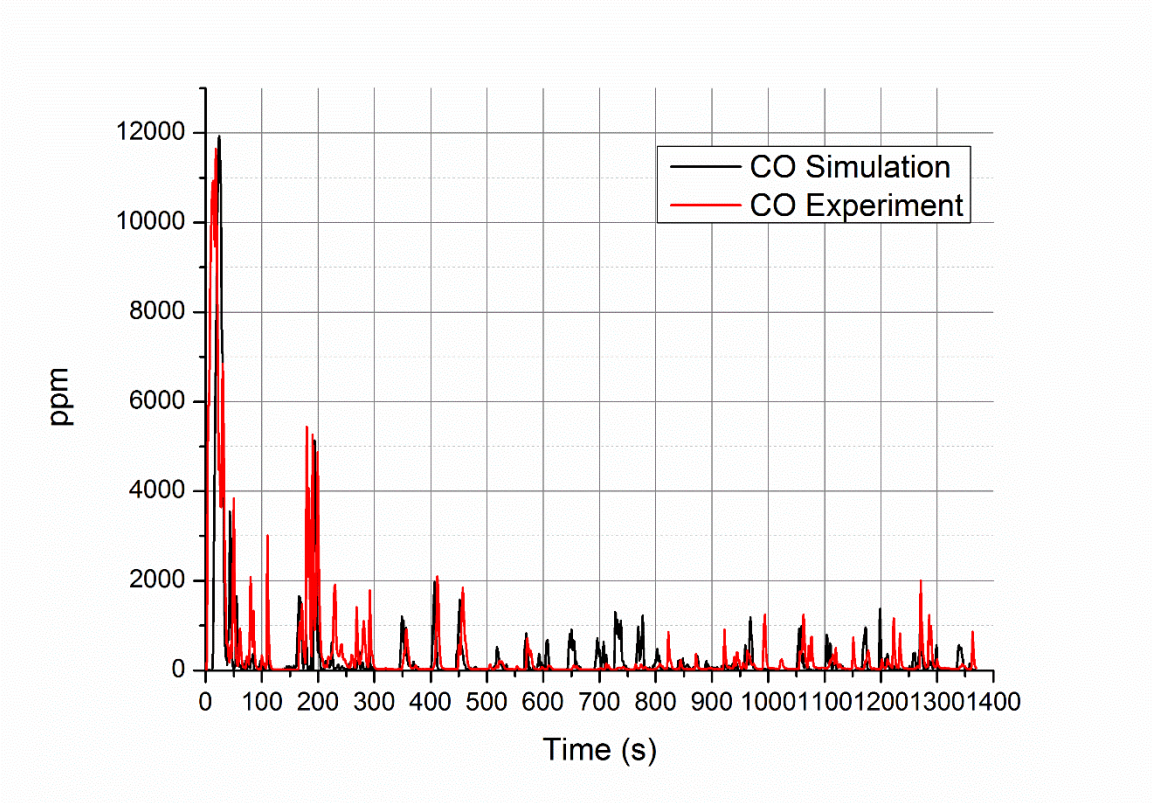

Figure 3.25: Transient line diagram of high-fidelity model CO output mole fraction

From the curve of the transient CO output results, it can be observed that the experimental and simulated value fit well for most of the peaks. Like the previous analysis, it is difficult to determine the model's accuracy simply based on Figure 3.25 due to the results' high transient. Moreover, the large peak at 0~50s reduces the figure's ordinate resolution and makes the error of the transient phase undetectable. Therefore, the scatter diagram is made in Figure 3.26.

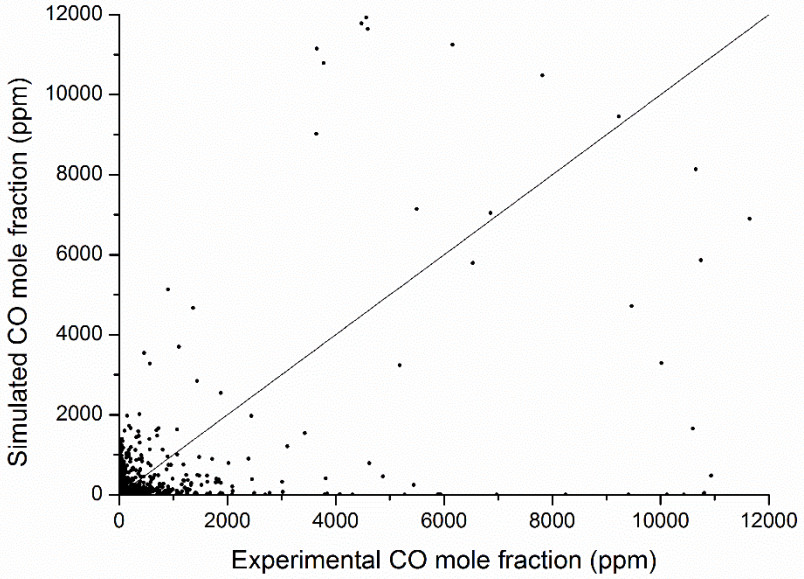

Figure 3.26: Scatter diagram of high-fidelity model CO output mole fraction

From Figure 3.26 it can be observed that the result points are more convergent to the line of y=x compared to the results shown in Figure 3.24. Therefore, it can be concluded that the model accuracy is improved to some extent.

In order to detect the model accuracy of the cold-start phase and the transient phase, the results gathered in these two phases are listed as line diagrams and scatter diagrams in Figure 3.27~Figure 3.30, respectively.

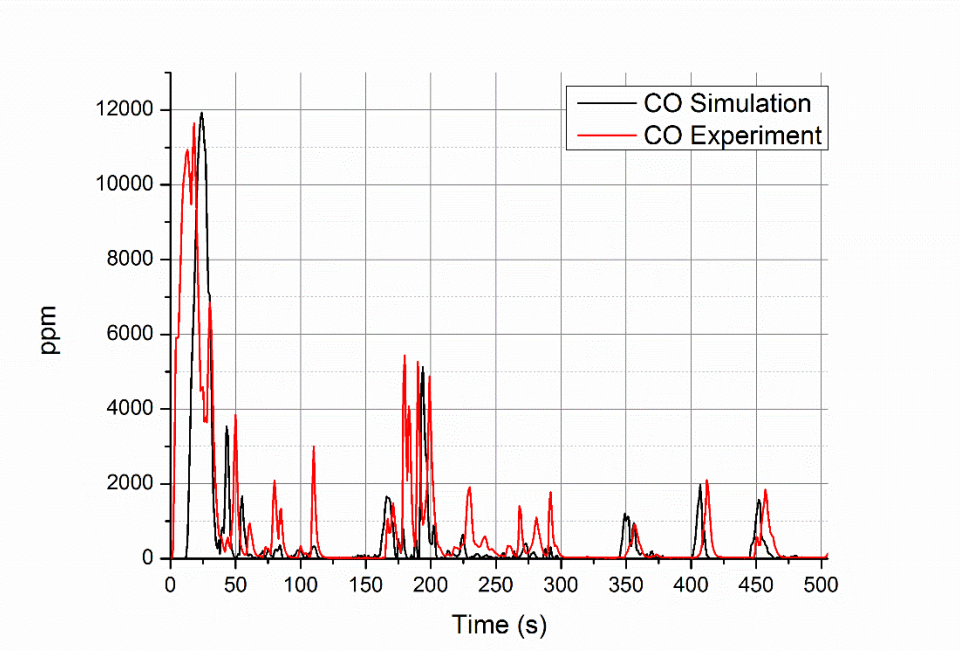

Figure 3.27 Transient line diagram of high-fidelity model CO output mole fraction in cold start phase

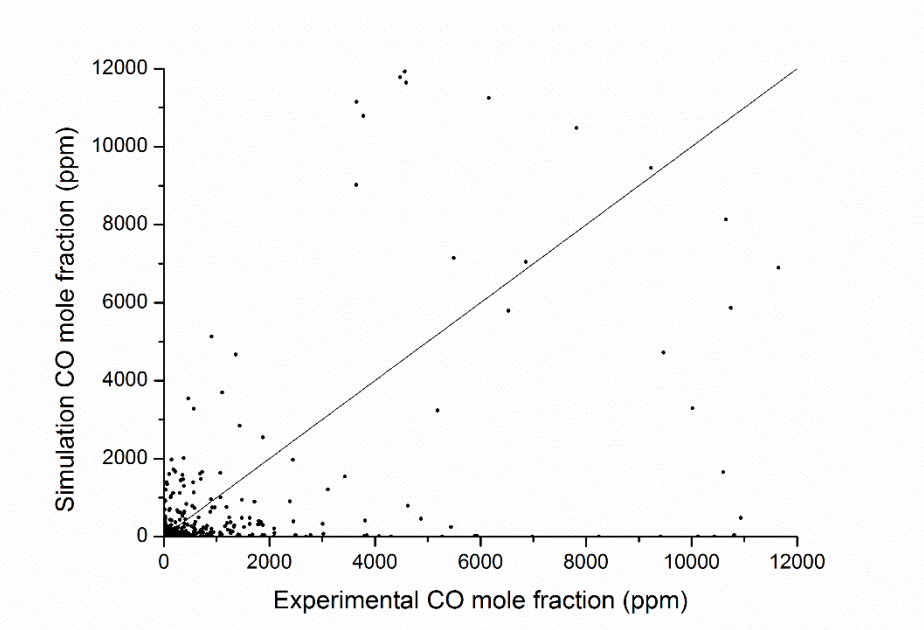

Figure 3.28 Scatter diagram of high-fidelity model CO output mole fraction in cold start phase

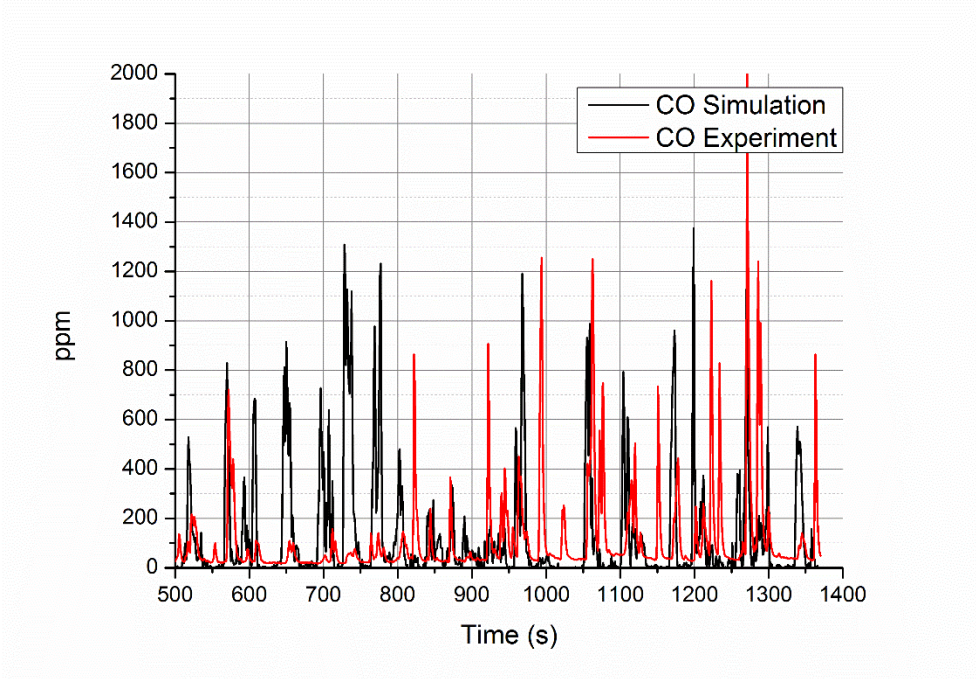

Figure 3.29 Transient line diagram of high-fidelity model CO output mole fraction in transient phase

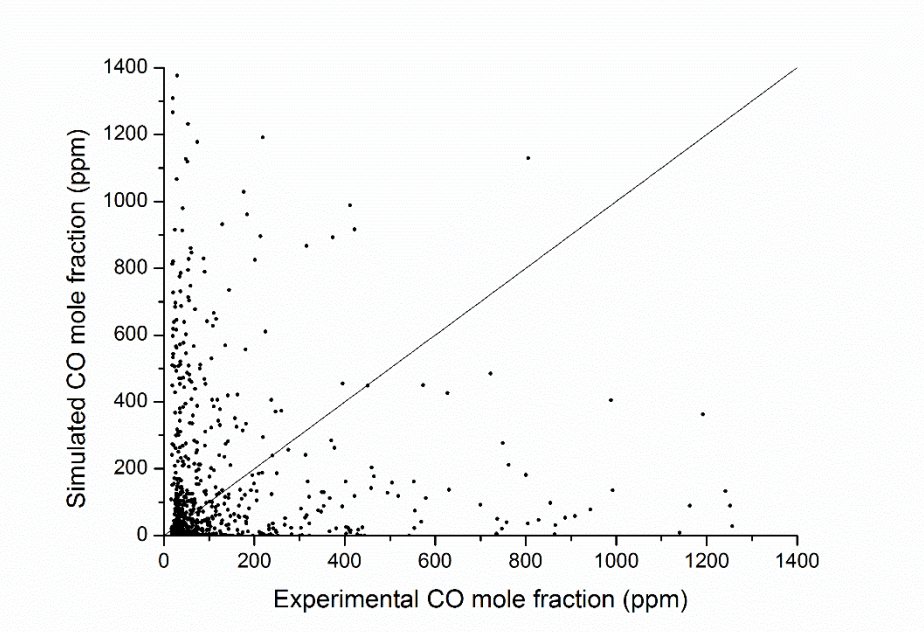

Figure 3.30 Scatter diagram of high-fidelity model CO output mole fraction in transient phase

In Figure 3.27 and Figure 3.28, it can be observed that the CO output error of the cold-start phase is small. Some time delays can also be observed in Figure 3.27, without which the result points could be more convergent to the line of y=x in Figure 3.28. In Figure 3.29, it can be observed that a relatively large error occurs from 600s to 800s. In addition, although some of the peaks do not fit well from 900s to 1,370s, the overall accuracy is acceptable. In Figure 3.30, it can be observed that a large proportion of the points are kept within a difference of 100 during the transient phase.

One of the major sources of error is the measurement uncertainty of the testing equipment. The accuracy of the mole fraction testing of the gas species is limited due to the testing sensors. In addition, stalled waste gas from the previous testing cycle may also produce errors in the results.

The total output species values are compared in order to determine the accuracy of the high-fidelity model. The total CO output values are shown in Table 3.9.

Table 3.9: Total CO output results

	Total output results	Values
Driving cycle	Experiment amount (gram)	8.606
	Experimental conversion efficiency	92%
	Simulation amount (gram)	9.801
	Simulated conversion efficiency	95%
0~100s	Experiment amount (gram)	3.776
	Simulation amount (gram)	2.171
100~200s	Experiment amount (gram)	2.046

	Simulation amount (gram)	1.402
200~300s	Experiment amount (gram)	0.818
	Simulation amount (gram)	0.789
300~400s	Experiment amount (gram)	0.184
	Simulation amount (gram)	0.613
400~500s	Experiment amount (gram)	0.620
	Simulation amount (gram)	0.797
500~600s	Experiment amount (gram)	0.122
	Simulation amount (gram)	0.446
600~700s	Experiment amount (gram)	0.038
	Simulation amount (gram)	0.509
700~800s	Experiment amount (gram)	0.068
	Simulation amount (gram)	0.975
800~900s	Experiment amount (gram)	0.070
	Simulation amount (gram)	0.213
900~1000s	Experiment amount (gram)	0.190
	Simulation amount (gram)	0.413
1000~1100s	Experiment amount (gram)	0.197
	Simulation amount (gram)	0.424
1100~1200s	Experiment amount (gram)	0.133
	Simulation amount (gram)	0.483
1200~1300s	Experiment amount (gram)	0.304
	Simulation amount (gram)	0.399

As illustrated in Table 3.9, the differences between the total output results in the experimental and the simulated data are small across the entire driving cycle. In addition, the total output results for every 100s period of the driving cycle are calculated individually.

It can be observed in Table 3.9 that for the period of 0~300s, a large difference occurs, and the experimental result is approximately 2g higher than the simulated result. For the period of 500~800s, a large difference also occurs, and the simulated result is approximately 2g higher than the experimental amount. In addition to the total output result, conversion efficiency is an alternative indicator of the model's accuracy. It can be observed in Table 3.9 that the conversion efficiency values are extremely similar, which means that the overall reduction in pollutants is similar across the experiment and the simulation.

The transient output mole fraction result for HC is illustrated in Figure 3.31.

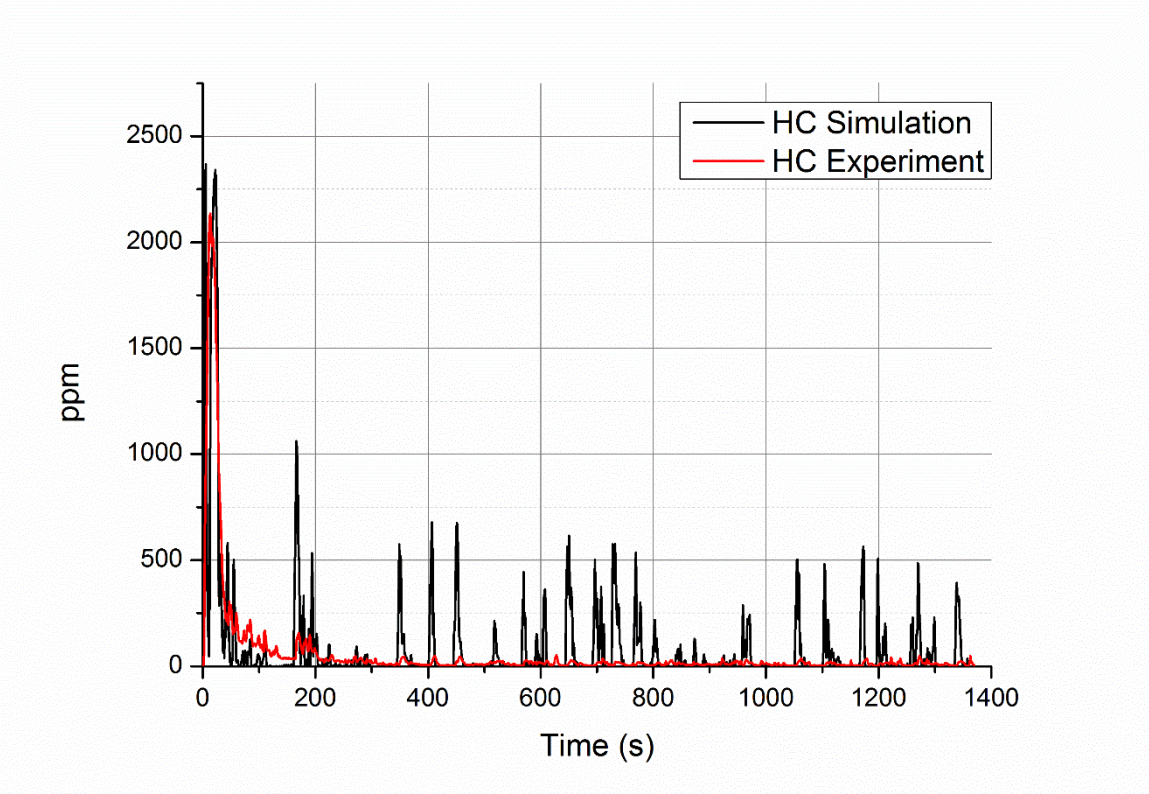

Figure 3.31: Transient line diagram of high-fidelity model HC output mole fraction

The transient output result of the HC mole fraction indicates that some peaks do not fit well during the driving cycle. As with the CO mole fraction result, the large peak at

0~50s reduces the figure's ordinate resolution and makes the error of the transient phase undetectable. Therefore, the scatter diagram is made in Figure 3.32.

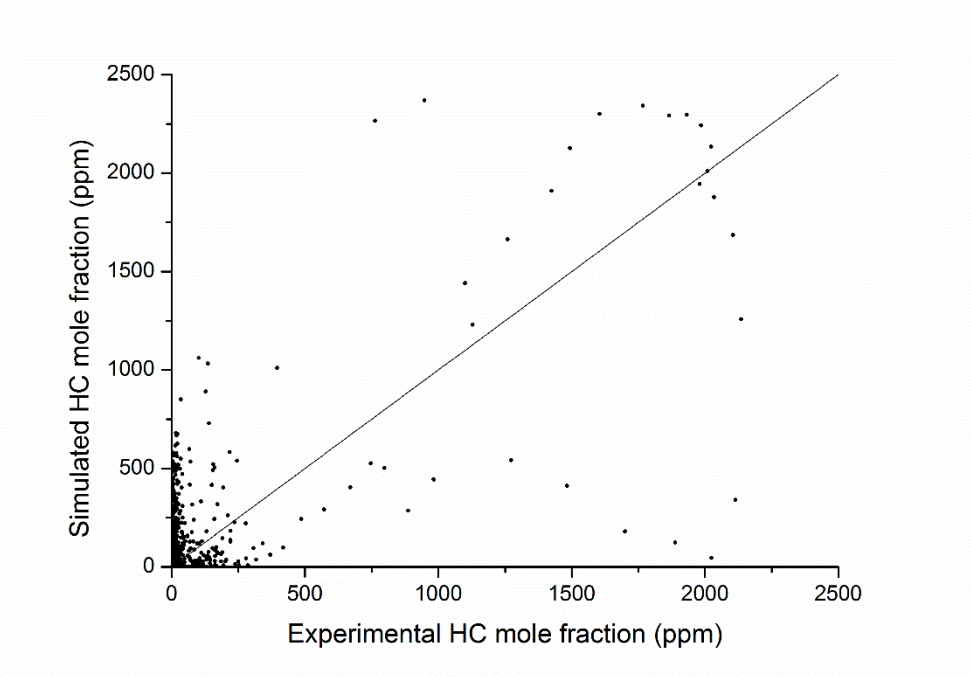

Figure 3.32 Scatter diagram of high-fidelity model HC output mole fraction

From Figure 3.31 and Figure 3.32 it can be observed that the model accuracy has been greatly improved after the parameter-tuning. In order to detect the model accuracy of the cold-start phase and the transient phase, the HC outlet mole fraction results gathered in these two phases are listed as line diagrams and scatter diagrams in Figure 3.33~Figure 3.36, respectively.

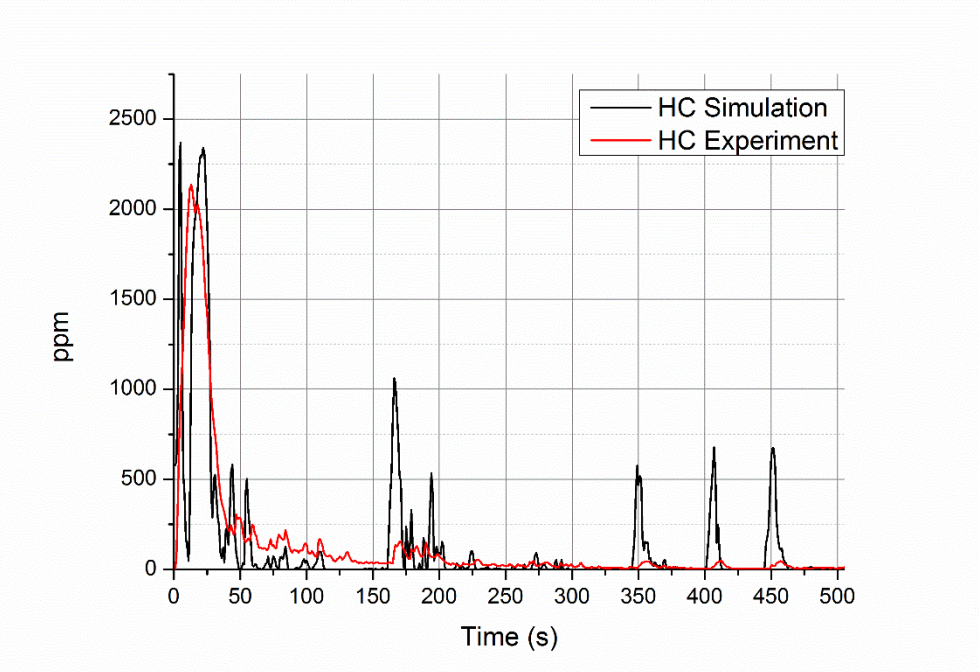

Figure 3.33: Transient line diagram of high-fidelity model HC output mole fraction in cold start phase

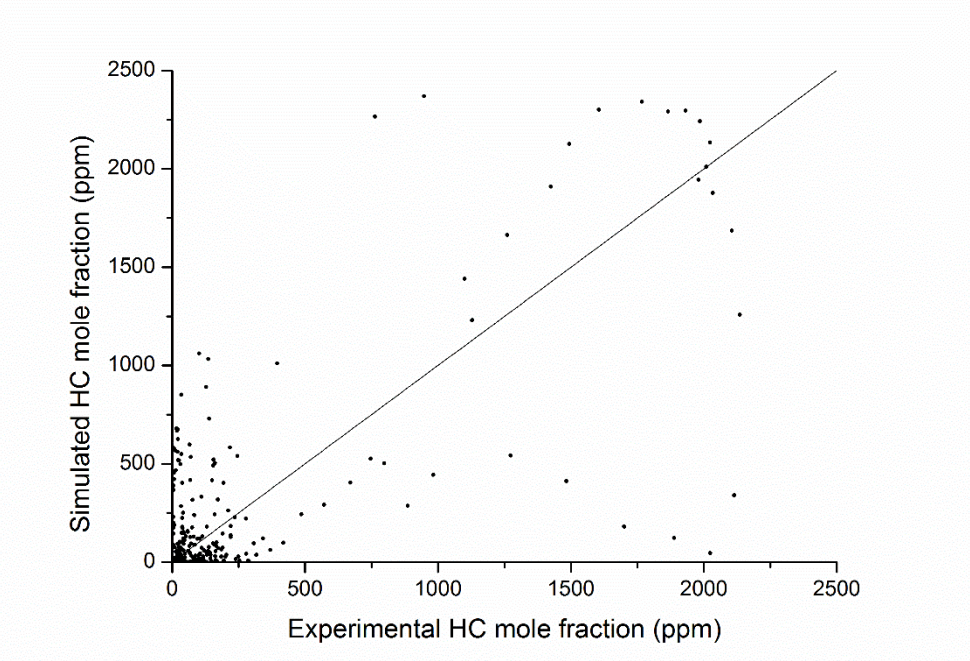

Figure 3.34: Scatter diagram of high-fidelity model HC output mole fraction in cold start phase

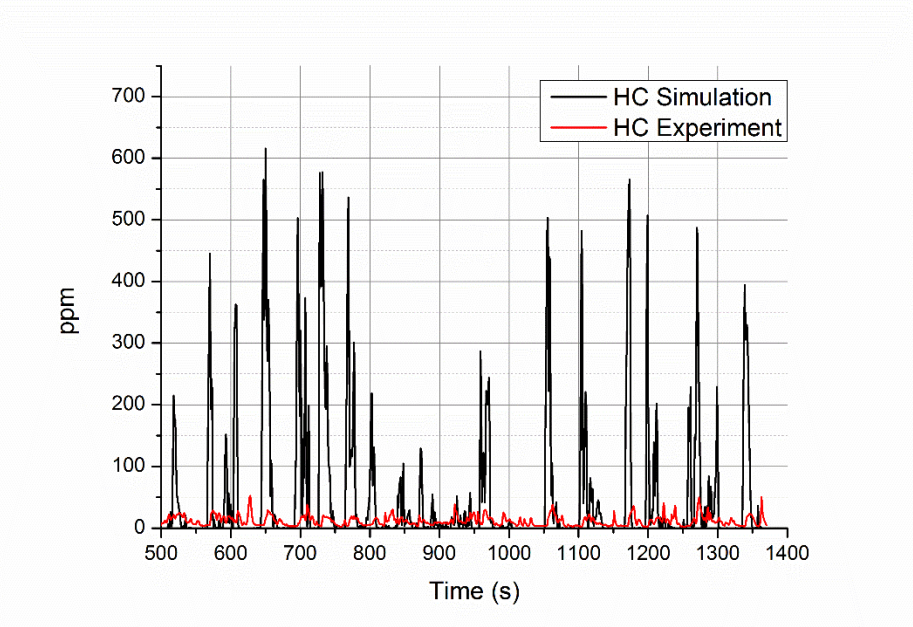

Figure 3.35: Transient line diagram of high-fidelity model HC output mole fraction in transient phase

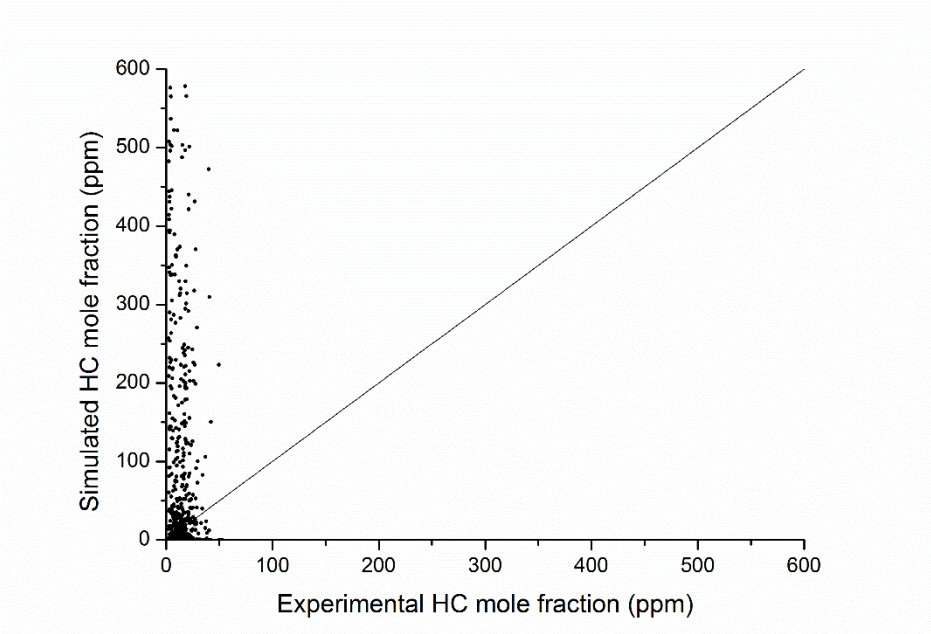

Figure 3.36: Scatter diagram of high-fidelity model HC output mole fraction in transient phase

In Figure 3.33, it can be observed that the curves generally fit well during the cold-start phase, with the exception of some peaks. Therefore, most of the points are observed to be convergent to the line of y=x in Figure 3.34. In Figure 3.35, it is evident that some peaks do not fit well, which causes a large error. And the result points in Figure 3.36 cannot be convergent well. However, the purpose of the current research is to develop a control-oriented model, which has a greater tolerance for output error. Therefore, the accuracy of the model is acceptable.

The test data may also be affected by the accuracy of the sensors. In addition, residual waste gas inside the converter from previous testing cycles is also considered to be a possible source of error.

The total HC output results are shown in Table 3.10.

Table 3.10: Total HC output results

	Total output results	Values (ppm)
Driving cycle	Experiment amount (gram)	0.601
	Experimental conversion efficiency	98%
	Simulation amount (gram)	1.870
	Simulated conversion efficiency	97%
0~100s	Experiment amount (gram)	0.430
	Simulation amount (gram)	0.398
100~200s	Experiment amount (gram)	0.044
	Simulation amount (gram)	0.167
200~300s	Experiment amount (gram)	0.025

	Simulation amount (gram)	0.069
300~400s	Experiment amount (gram)	0.009
	Simulation amount (gram)	0.121
400~500s	Experiment amount (gram)	0.012
	Simulation amount (gram)	0.182
500~600s	Experiment amount (gram)	0.008
	Simulation amount (gram)	0.094
600~700s	Experiment amount (gram)	0.006
	Simulation amount (gram)	0.145
700~800s	Experiment amount (gram)	0.007
	Simulation amount (gram)	0.174
800~900s	Experiment amount (gram)	0.005
	Simulation amount (gram)	0.039
900~1000s	Experiment amount (gram)	0.007
	Simulation amount (gram)	0.059
1000~1100s	Experiment amount (gram)	0.005
	Simulation amount (gram)	0.011
1100~1200s	Experiment amount (gram)	0.005
	Simulation amount (gram)	0.113
1200~1300s	Experiment amount (gram)	0.007
	Simulation amount (gram)	0.080

As shown by the total HC output results, the difference between the simulated and experimental data is relatively large, which is mainly caused by the peaks during the transient phase. As was done with the CO analysis, the total output results for every 100s of the driving cycle are calculated individually. During the cold-start period, 0~200s, the difference between the simulated and experimental data is small. During the other time

periods, the simulated results are higher than the experimental results. In addition, during the period of 700~900s, large differences occur. The total HC output results are consistent with the transient output mole fraction results.

The transient mole fraction results for NO are illustrated in Figure 3.37.

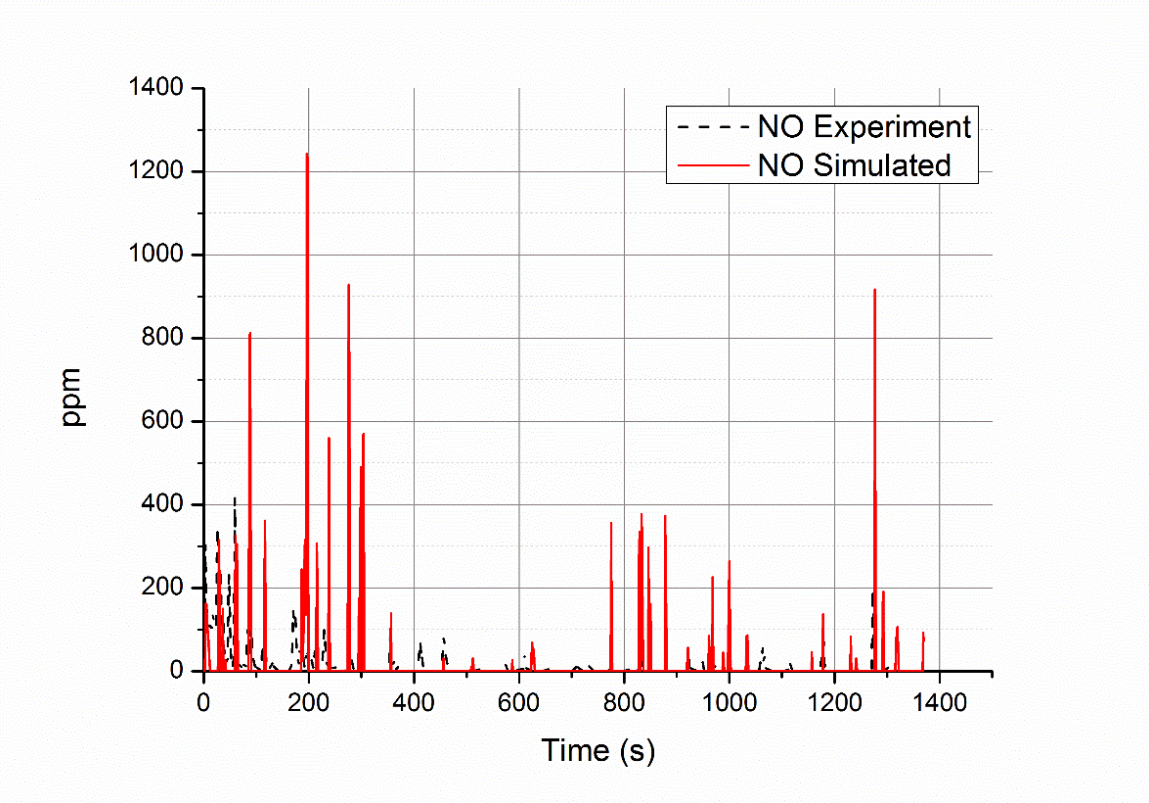

Figure 3.37: Transient output results of the NO mole fraction

As shown in Figure 3.37, the transient NO outputs do not fit as well as those of CO. Several peaks in the simulated results do not fit with the experimental results. In real applications, the tailpipe-out NO concentration is extremely low compared to the CO and HC concentrations. A significant amount of NO is normally removed inside the TWC converter. In addition, there is significant measurement uncertainty regarding NO due to

the equipment. Therefore, the composition of NO does not receive much weight when evaluating the high-fidelity model's accuracy.

3.2.5.2 Transient simulation temperature results

The transient temperatures of the 10 testing points for the solid phase are measured. The warming-up performance between 0s and 200s is shown in Figure 3.38.

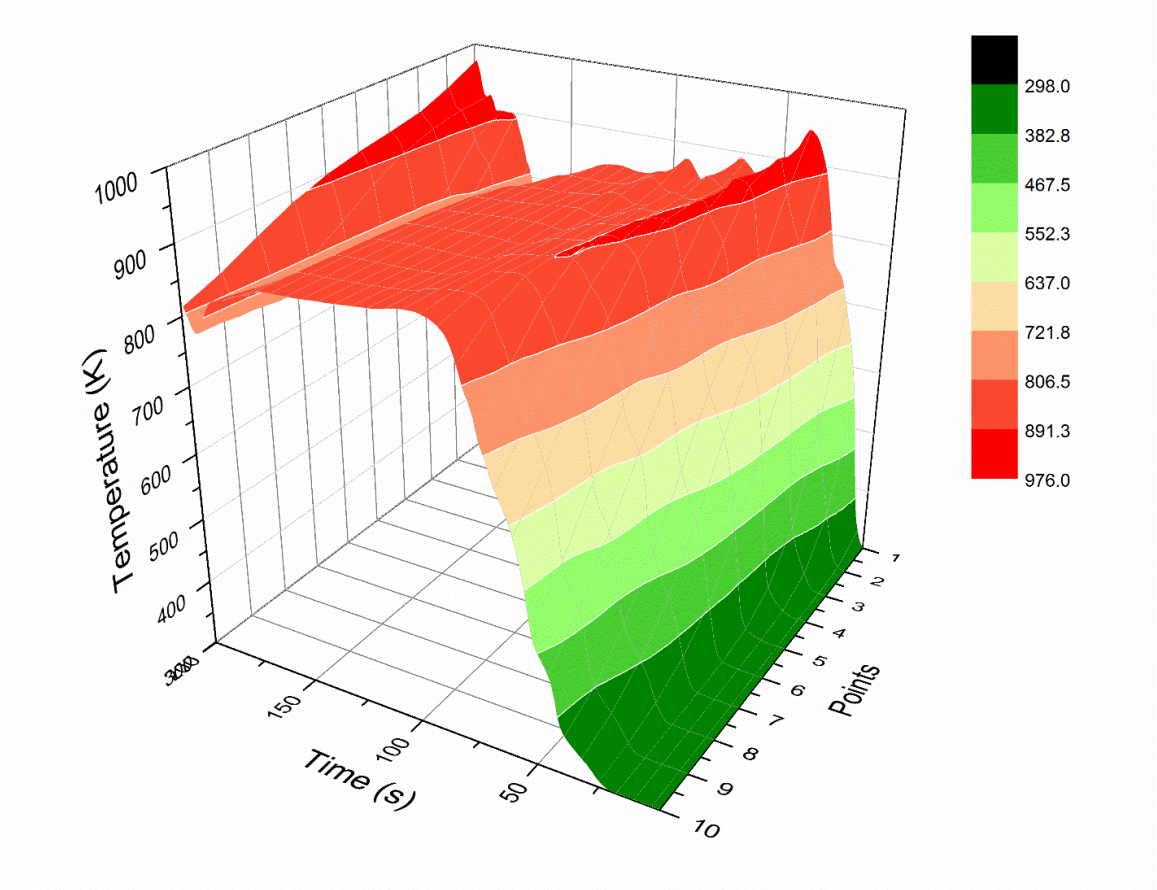

Figure 3.38: Transient warming-up performance

The warming-up time of the outlet (point 10) is around 125s in the driving cycle simulation. The warming-up time is shorter than normal (around 500s) because the

converter tested in the present study is just a protype for testing, and it is shorter than the commercially embedded converters. A comparison between the tested and simulated outlet temperatures is presented in Figure 3.39.

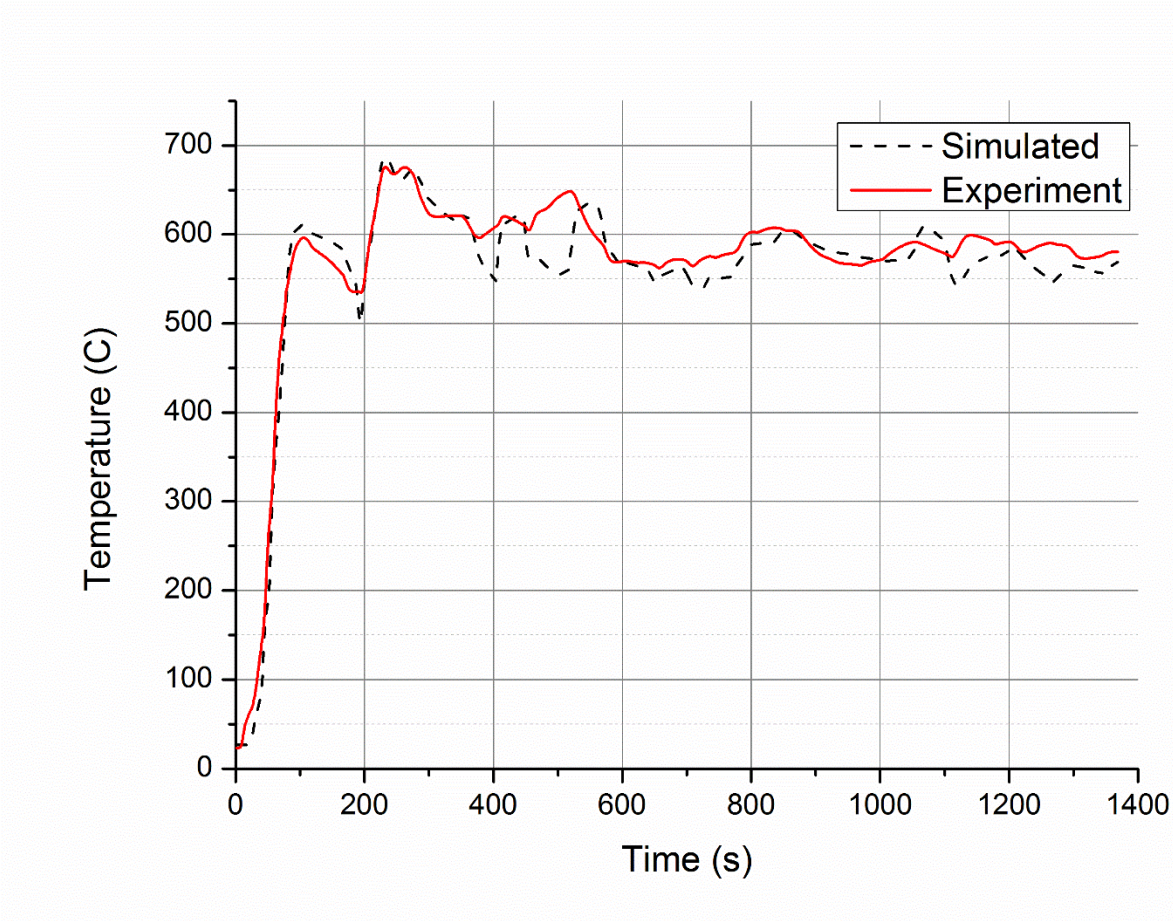

Figure 3.39: Transient outlet temperature results

Figure 3.39 indicates that the differences in warming-up time between the experimental and simulated data are small. The model is able to simulate the temperature response of the TWC experimental data.

Chapter 4 : Reduced-Order TWC Converter Model

4.1 Reduction of the high-fidelity model

Although the high-fidelity model developed in Chapter 3 is sufficiently accurate for control and OBD systems, it is computationally demanding, and control and state estimation strategies are thus difficult to implement. Therefore, reducing the model's computational cost is important for the development of a control-oriented model. This chapter focuses on the simplification of the high-fidelity model.

Harsha [58] developed a reduced-order model of the catalytic converter focusing on two aspects, reaction reduction and phase reduction. Based on Harsha's [58] research, a similar model reduction is performed in the present study.

The reduced-order TWC converter model developed in this chapter employs bulk phase energy conservation equations instead of the separate gas-phase and solid-phase energy conservation equations used in the high-fidelity model. This strategy reduces the model's complexity. Therefore, simulation time and computational costs are reduced.

4.1.1 Phase simplification

The result of the constant inlet simulation shows that the relatively higher rate of gas-solid heat transfer only lasts for a short period, as shown in Figure 4.1. The inlet gas volume flow rate is 1 m^3/min, and the temperature is 500 °C.

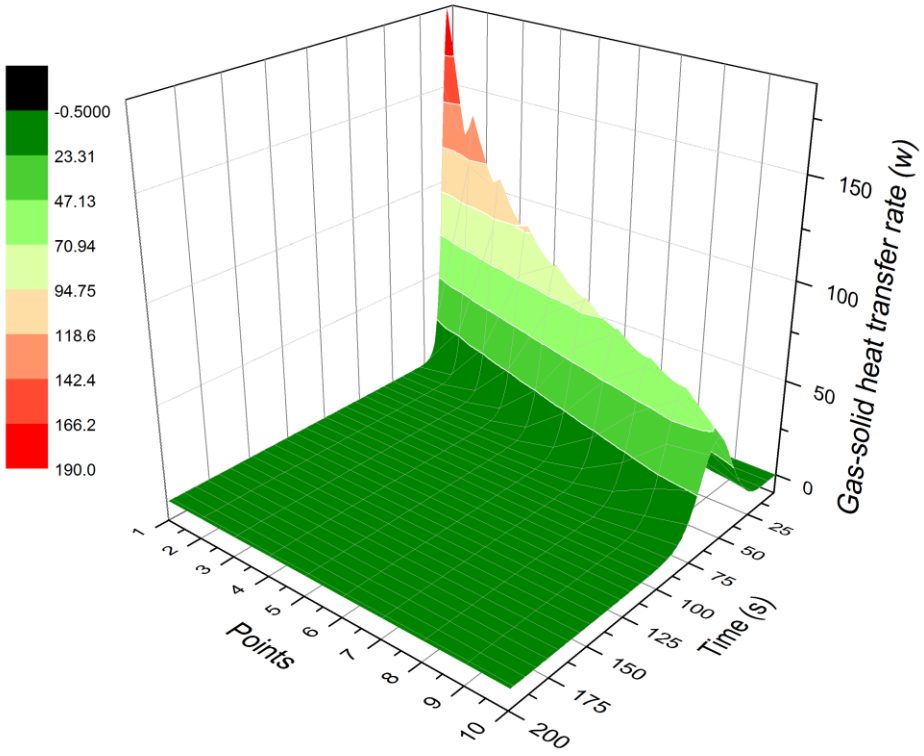

Figure 4.1: Constant inlet gas-solid heat transfer rate

A similar phenomenon is observed in the transient simulation. Figure 4.2 shows the gas-solid heat transfer rates of the driving cycle simulation.

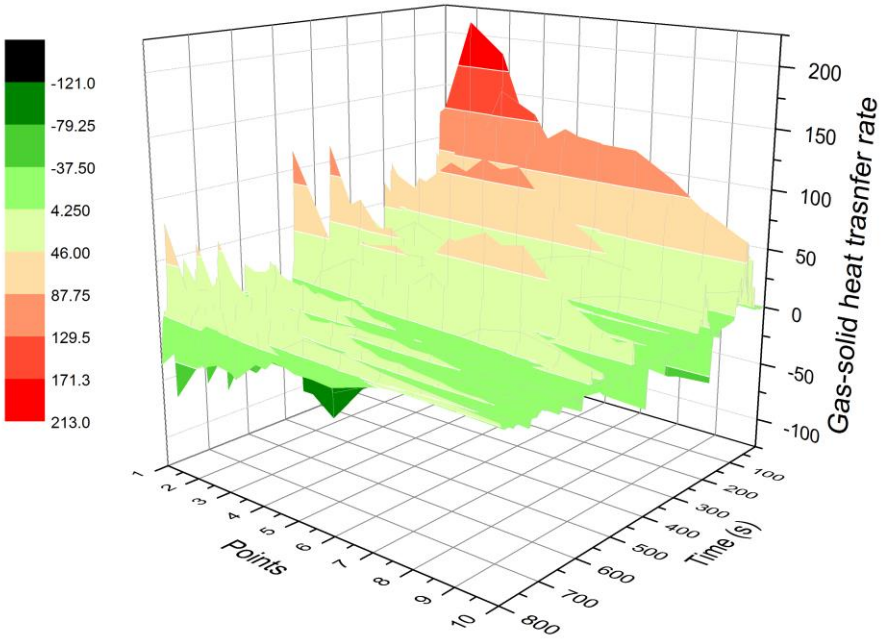

Figure 4.2: Transient gas-solid heat transfer rates

The gas and solid temperatures are compared in the simulations. Figure 4.3 shows the temperatures of the gas and solid phases during the constant inlet simulation without chemical reactions.

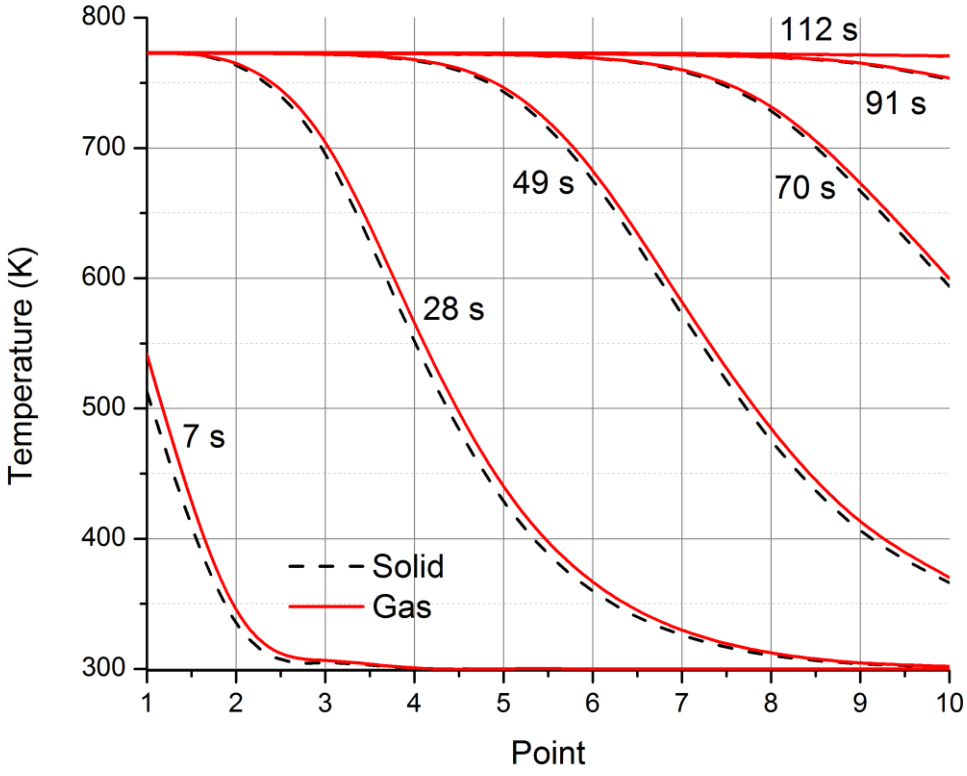

Figure 4.3: Gas and solid temperatures during the constant inlet simulation

As shown in Figure 4.3, the differences in temperature between the gas and solid phases are small during the constant inlet simulation. Small temperature differences can also be observed in the driving cycle simulation with all the chemical reactions included, as shown in Figure 4.4.

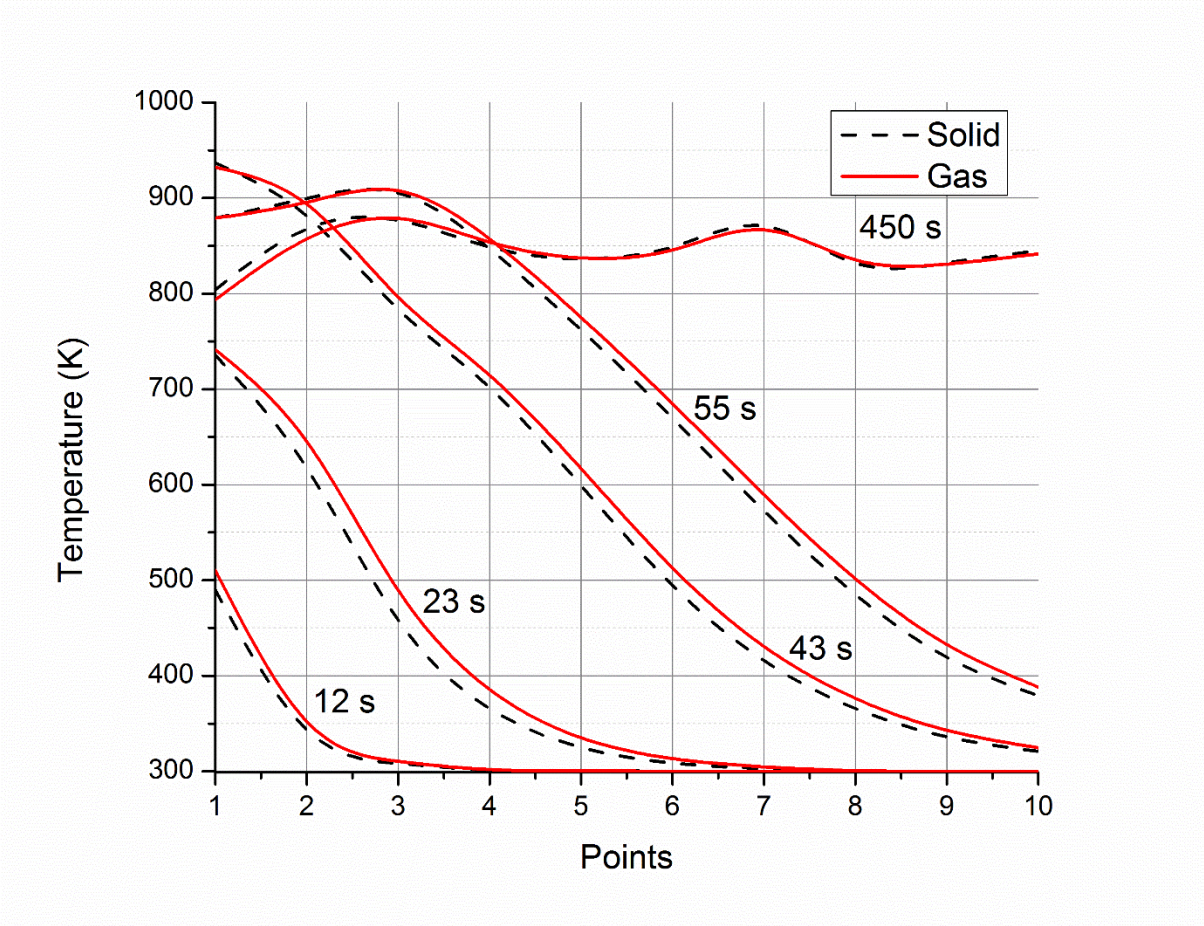

Figure 4.4: Gas and solid temperatures during the transient simulation

Due to this phenomenon, the temperatures of the gas and solid phases (wash-coat and substrate) are assumed to be equal.

$$T_{r,g,k} = T_{r,s,k} = T_{r,k}$$

According to the analysis of the differences in temperature between the gas and solid phases, the phase simplification is conducted by combining the solid and gas phases as a bulk, as shown in Figure 4.5.

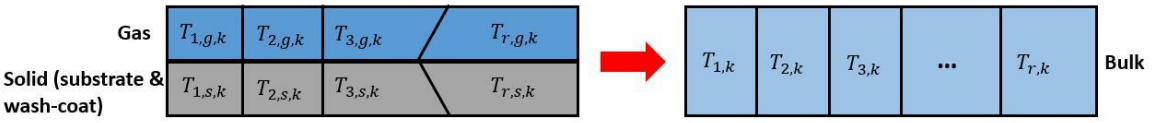

Figure 4.5: Phase simplification of the high-fidelity model

In Figure 4.5, $T_{r,g,k}$ is the temperature of the gas phase; and $T_{r,s,k}$ is the temperature of the solid phase. In the diagram showing the model following simplification, $T_{r,k}$ is the temperature of the bulk.

All the assumptions remain the same as those that apply to the high-fidelity model.

4.1.2 Reaction simplification

Reaction simplification is achieved by reducing the number of reactions taken into consideration.

In the high-fidelity model, 15 reactions are considered. These include oxidation reactions, reduction reactions, water-gas shift reactions and oxygen storage reactions. The reaction rates of different reactions are calculated in different ways, which leads to complexity when calculating the heat release and species concentration. Voltz. et al. [34] have shown that pollutant reduction inside the converter can be represented by specific

reactions. In the present study, a similar concept is used. Reactions with a larger contribution to the results are used as the overall reactions in the converter. Thus, the number of reactions is reduced, and the computation of the model is simplified significantly.

In [78] and [79], CO is assumed to be the main species participating in NO reduction. Hence, the reaction between CO and NO is the dominant mechanism in NO reduction. Since CO serves as the reducing agent for NO, the latter is the oxidising agent for the former. A similar assumption is made in this thesis. The reaction between CO and NO is chosen to represent the reduction of NO, since the former reaction has the largest contribution to the reduction of CO concentration. In addition, this reaction has fewer products (CO_2 and N_2) compared to that of C_3H_6 and NO (CO_2, H_2O and N_2).

In [78], the reactions between CO, C_3H_6 and O_2 were also chosen to model the TWC converter in the exclusion of NO modelling, and they proved to be sufficient for heat transfer research. Therefore, the reactions of the reduced-order model in the present study are adopted from [78]. Four reactions are chosen to represent the reactions in the catalytic converter. The chemical equations of the reactions used in the present study are given below:

$$CO + NO \rightarrow CO_2 + 0.5N_2$$

$$CO + 0.5O_2 \rightarrow CO_2$$

$$C_3H_6 + (9/2)O_2 \rightarrow 3CO_2 + 3H_2O$$

$$H_2 + 0.5O_2 \rightarrow H_2O$$

4.2 Reduced-order model

The process and principles of the reduced-order TWC converter model are the same as those of the high-fidelity model. The reduced-order model includes the heat and mass transfer sub-model and the reaction kinetics sub-model. The heat and mass conservation is used to calculate the temperature and output mole fraction. In addition, the Langmuir-Hinshelwood mechanism is applied to calculate the reaction rates.

4.2.1 Heat and mass transfer of the reduced-order model

The heat transfer equation of the reduced-order TWC converter model is simplified by calculating the one-dimensional heat transfer of the bulk phase. The heat transfer equation is given below.

$$\left(\Psi_s + \varepsilon\rho c_p\right)\frac{\partial T}{\partial t} = -\varepsilon\rho u c_p\frac{\partial T}{\partial x} - \sum_{j=1}^{n}\Delta h_j r_j \tag{33}$$

$j = \text{reactions}$

In this equation, ρ represents the density of the gas, and c_p is the specific heat of the exhaust gas. Other parameters remain the same as those in the high-fidelity model. The mass conservation equations and parameters are also kept unchanged.

4.2.2 Reaction kinetics of the reduced-order model

The Langmuir-Hinshelwood mechanism is used to calculate the reaction rates of the reduced-order model. Reaction rates are calculated based on three factors: the adsorption rate, the total number of possible collisions; and the number of effective collisions, as mentioned in Chapter 3.

The reaction rates of the reduced-order model reactions are given by (34):

$$r_j = k_i c_{reactant1} c_{reactant2} \tag{34}$$

The reaction rate parameter k_i is given by equation (35):

$$k_i = A_i \exp\left(\frac{-E_i}{RT}\right) / G \tag{35}$$

The inhibition factor G is calculated directly using the parameters from the model developed by Chan and Hoang [78]. The equation of G is given below.

$$G = T_s\left(1 + K_1 c_{CO} + K_2 c_{C_3H_6}\right)^2 (1 + K_3 c_{CO}^2 c_{C_3H_6}^2)(1 + K_4 c_{NO}^{0.7}) \quad (36)$$

Where $K_1 = 65.5\exp^{\frac{961}{T}}$, $K_2 = 2.1 \times 10^3 \exp^{\frac{361}{T}}$, $K_3 = 4\exp^{\frac{11611}{T}}$, and $K_4 = 4.8 \times 10^5 \exp^{\frac{-3773}{T}}$.

The initial pre-exponent multiplier and activation energy values are also directly adopted from Chan and Hoang's [78] model. The initial kinetic parameter values are given in Table 4.1. The parameters are tuned according to the errors between the high-fidelity model outlet and the reduced-order model outlet in a later section.

Table 4.1: Initial values of the reaction rate parameters

Reactions	Pre-exponent multiplier	Activation energy
$CO + NO \rightarrow CO_2 + 0.5N_2$	6.45×10^9	52374
$CO + 0.5O_2 \rightarrow CO_2$	1.005×10^{14}	16574
$C_3H_6 + (9/2)O_2 \rightarrow 3CO_2 + 3H_2O$	1.392×10^{15}	19250
$H_2 + 0.5O_2 \rightarrow H_2O$	1.005×10^{14}	16574

4.3 Reduced-order model simulation

The reduced-order model of the TWC converter is tested by subscript coding in MATLAB. The discretization length of the converter is $5mm$.

4.3.1 Constant inlet simulation

As with the high-fidelity model, a constant inlet chemical analysis is conducted in the section of the reduced-order model development. The data for the constant inlet simulation chemical analysis consists of CO, HC and NO inlet and outlet mole fraction data at seven inlet gas temperatures ranging from 500K to 800K at three different inlet volume flow rates, namely 0.8, 1.0 and 1.2 m^3/min.

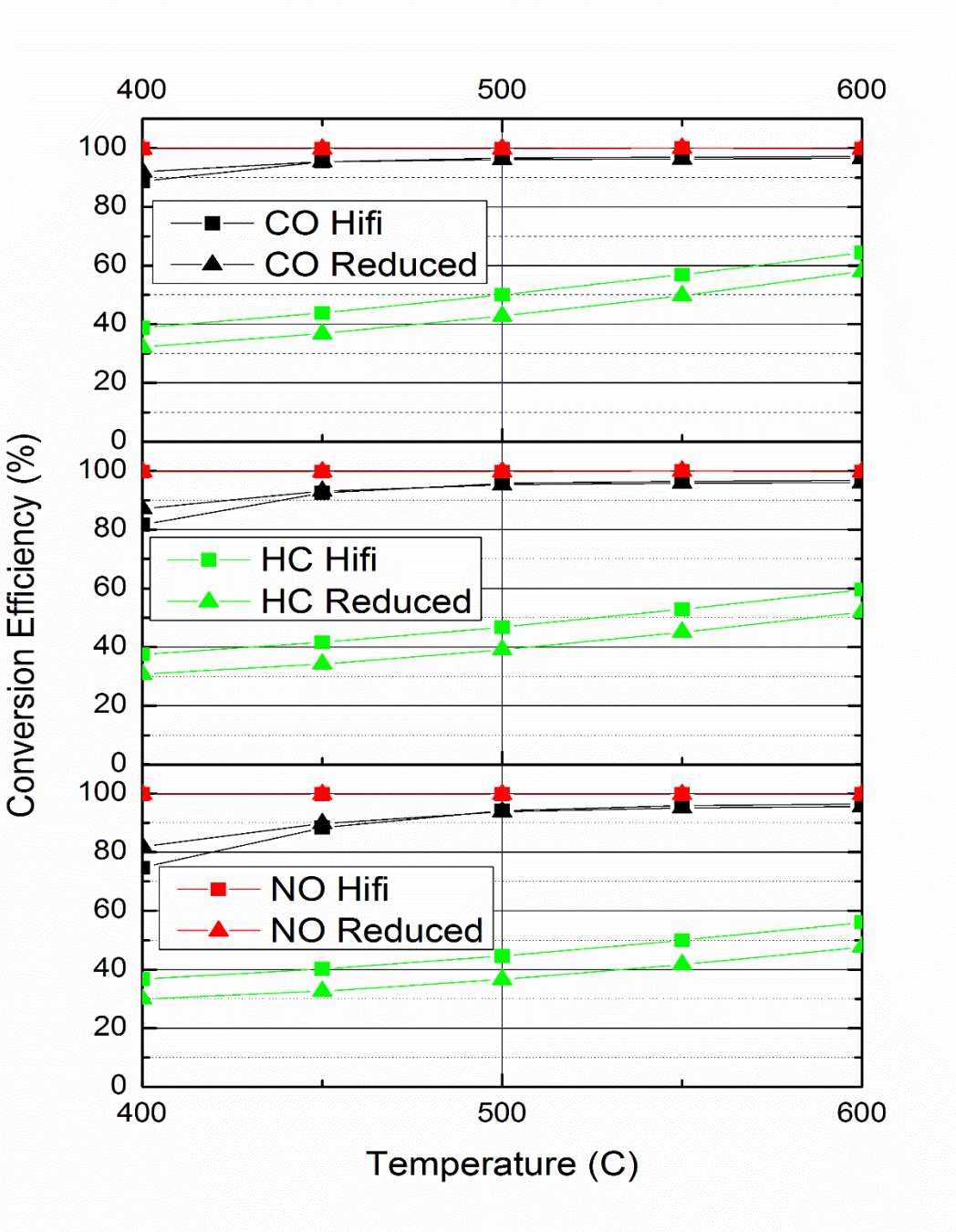

Figure 4.6: Conversion efficiency at different temperatures from 400 C to 600 C and different inlet volume rates of 0.8, 1.0 and 1.2

Figure 4.6 shows the conversion efficiency of HC, CO and NO at inlet volume flow rates of 0.8, 1.0 and 1.2 m^3/min (from top to bottom). From the general trend of the curves, it can be observed that conversion efficiency increases as the temperature increases and drops as the volume flow rate increases. For an inlet volume flow rate of 0.8 m^3/min, the conversion efficiency of HC is over 30% at a temperature of 400 °C and reaches 60% at a temperature of 600 °C. The conversion efficiency of CO reaches over 90% at a temperature of 450 °C. The conversion efficiency of NO is high. For an inlet volume rate of 1.0 m^3/min, the conversion efficiency of HC is slightly higher than 30% at a temperature of 400 °C and reaches 50% at a temperature of 600 °C. The conversion efficiency of CO reaches over 90% at a temperature of 500 °C. For an inlet volume rate of 1.2 m^3/min, the conversion efficiency of HC is 30% at a temperature of 500 °C and no more than 50% at a temperature of 600 °C. The conversion efficiency of CO reaches over 90% at a temperature of 500 °C.

4.3.2 Temperature results of driving cycle simulation

The test results including the temperature and output mole fractions are illustrated below.

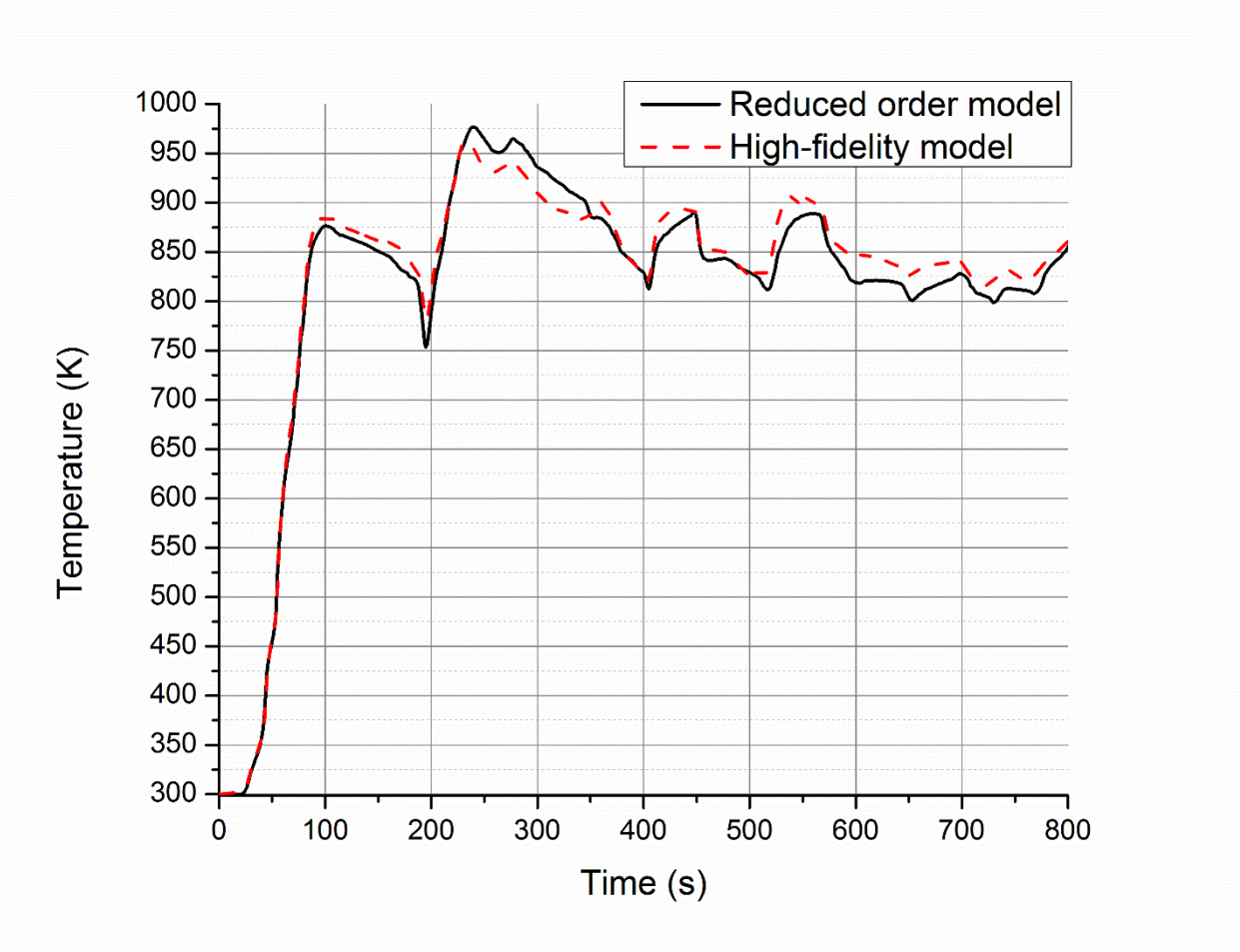

Figure 4.7: Temperature result curves

The temperature result curves are shown in Figure 4.7. It is evident that the temperature differences between the two models are small at most of the points. Thus, it can be concluded that the error caused by phase simplification is acceptable for control strategy and state estimation.

4.3.3 Chemical result of driving cycle simulation

For the adjustment of the reaction rate parameters, the outlet CO and HC mole fraction results of the reduced-order model with Chan and Hoang's [78] reaction rate parameter values (the initial reaction rate parameter values are shown in Table 4.1) are shown in Figure 4.8 ~Figure 4.10.

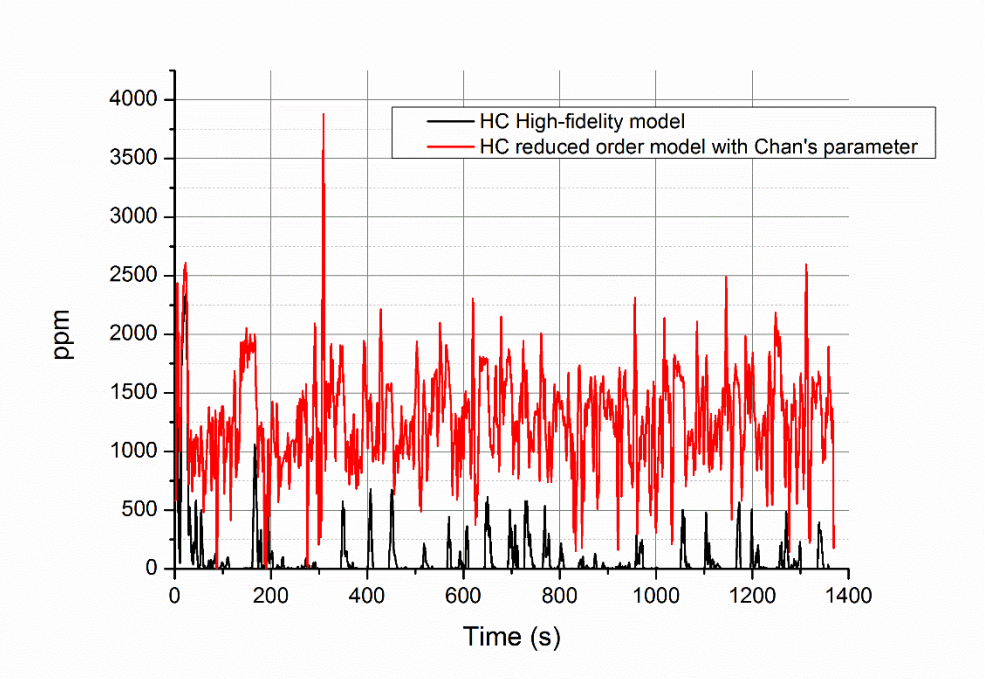

Figure 4.8: HC mole fraction result with Chan and Hoang's [78] parameter values

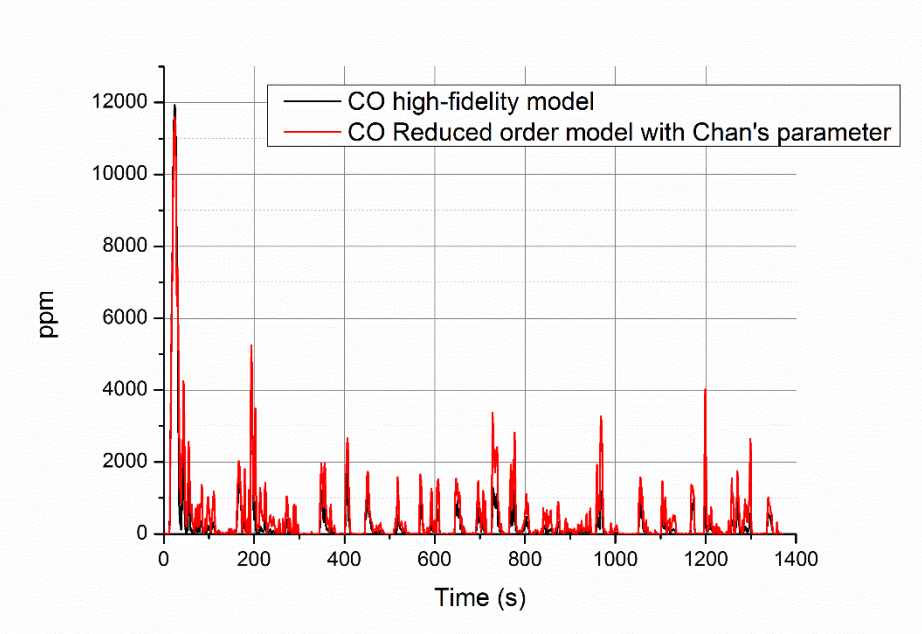

Figure 4.9: CO mole fraction result with Chan and Hoang's [78] parameter values

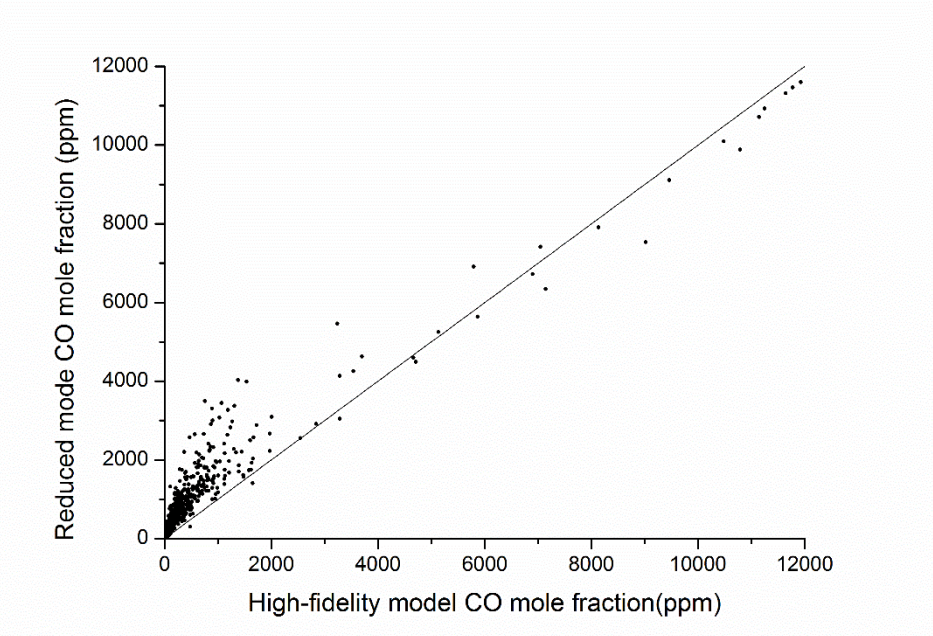

Figure 4.10: CO mole fraction scatter diagram with Chan and Hoang's [78] parameter values

Common with that of the high-fidelity model, the CO output mole fraction results are listed as scatter diagram as shown in Figure 4.10 to make the difference easier to be detected. In Figure 4.8 ~ Figure 4.10, it can be observed that the accuracy of the model using Chan and Hoang's [78] parameter values is less than satisfactory in the present study case. A particular problem is the outlet of HC mole fraction, which shows a large error throughout the driving cycle. Therefore, as with the parameter values of the high-fidelity model, the reaction rate parameter values of the reduced-order model also need to be re-tuned.

The pre-exponent multipliers and activation energy parameters are tuned manually by minimizing the transient outlet error between the measured and simulated data. The values of the pre-exponential multipliers and activation energy parameters after tuning are shown in Table 4.2. The outlet mole fraction results are illustrated in later sections.

Table 4.2: Reaction rate parameter values of the reduced-order model

Reactions	Pre-exponent multiplier	Activation energy
$CO + NO \rightarrow CO_2 + 0.5N_2$	6.45×10^9	52374
$CO + 0.5O_2 \rightarrow CO_2$	3.005×10^{14}	16574
$C_3H_6 + (9/2)O_2 \rightarrow 3CO_2 + 3H_2O$	9.899×10^{15}	19250
$H_2 + 0.5O_2 \rightarrow H_2O$	9.88×10^{13}	16574

As illustrated in Table 4.2, the HC-related reaction rate parameter value is increased significantly to make the HC outlet result acceptable. The CO-related reaction rate parameter value is increased slightly, while the hydrogen reaction rate parameter value is

decreased slightly. The adjustment range of the parameter values in the present study is kept within ten times the values used by Chan and Hoang [78].

The outlet results of the HC and CO mole fractions are shown in Figure 4.11 ~ Figure 4.14.

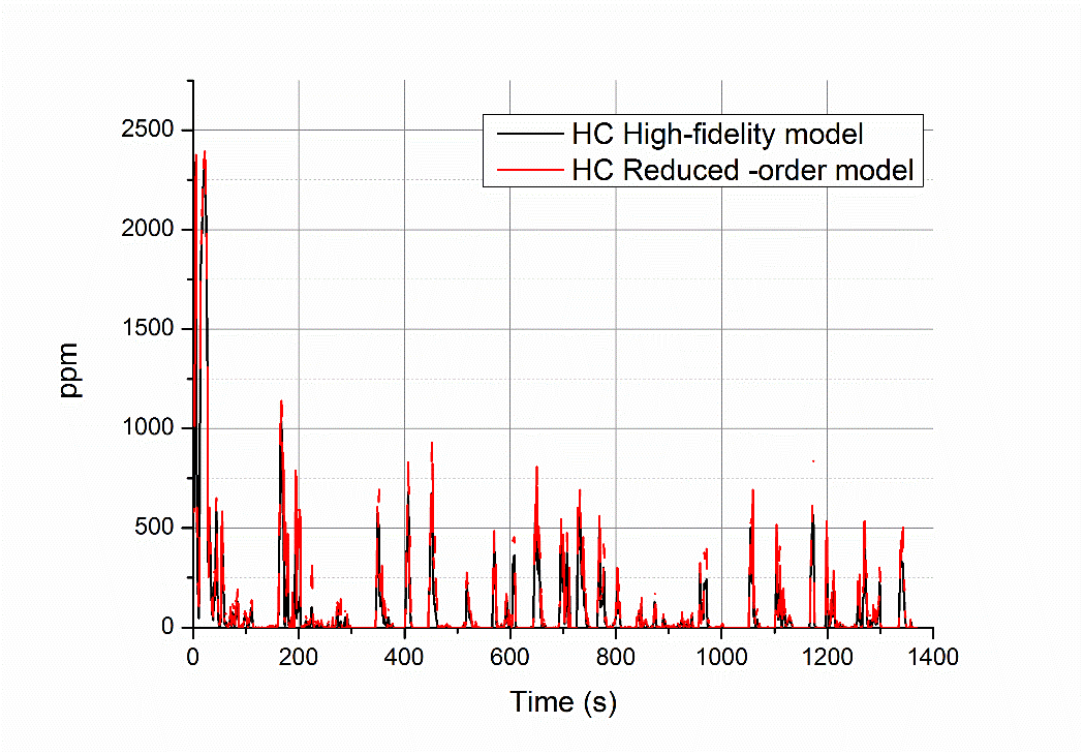

Figure 4.11 Transient line diagram of reduced-order model HC output mole fraction

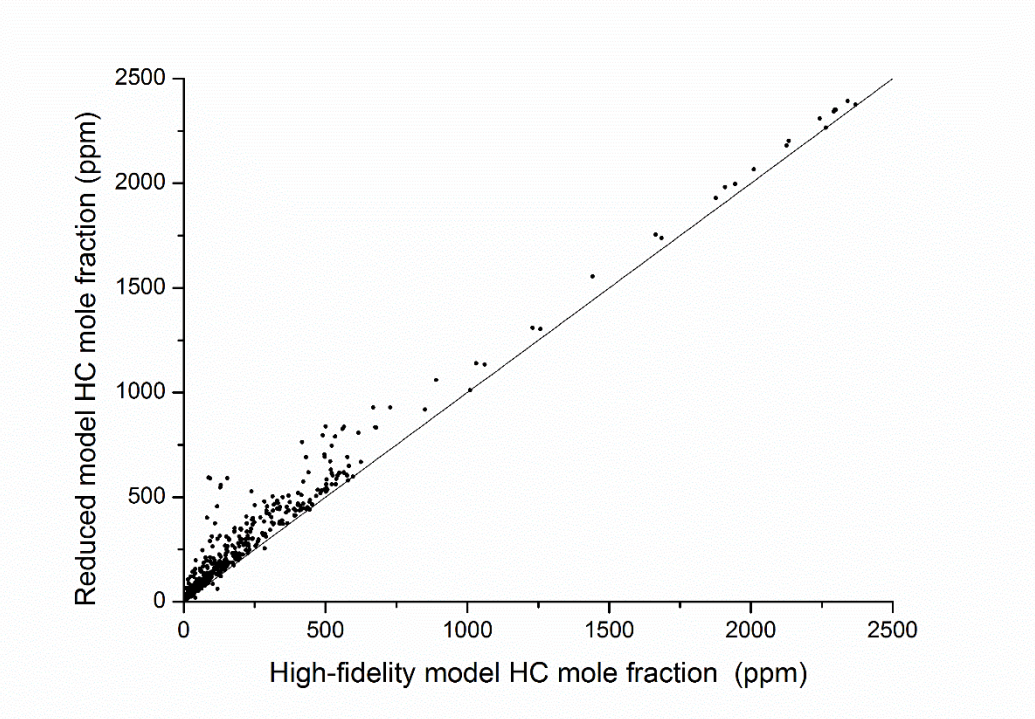

Figure 4.12: Scatter diagram of reduced-order model HC output mole fraction

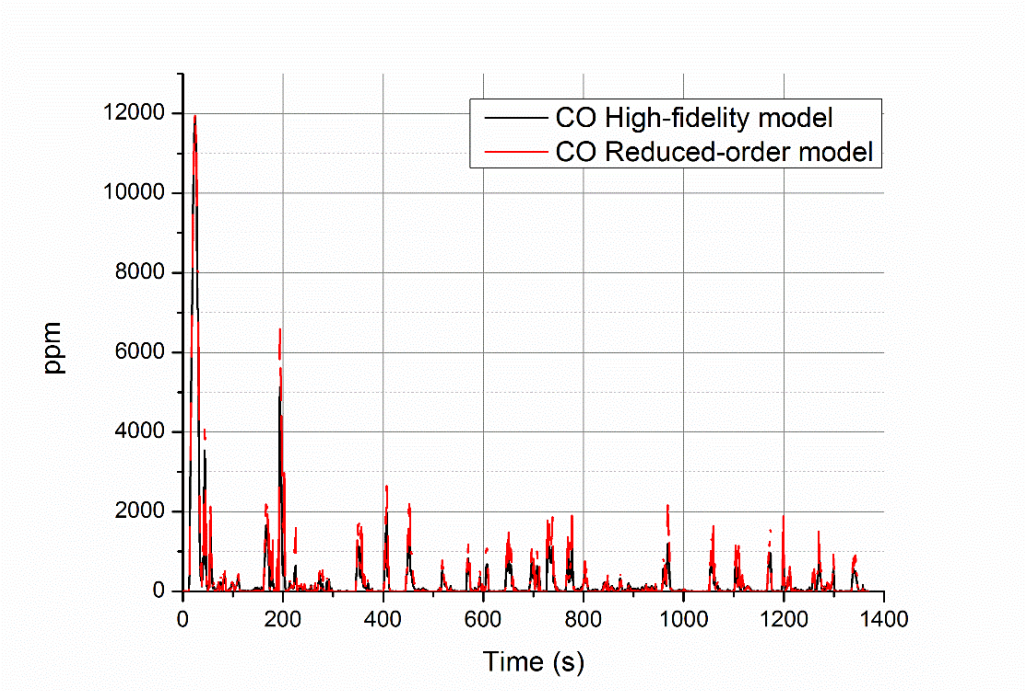

Figure 4.13 Transient line diagram of reduced-order model CO output mole fraction

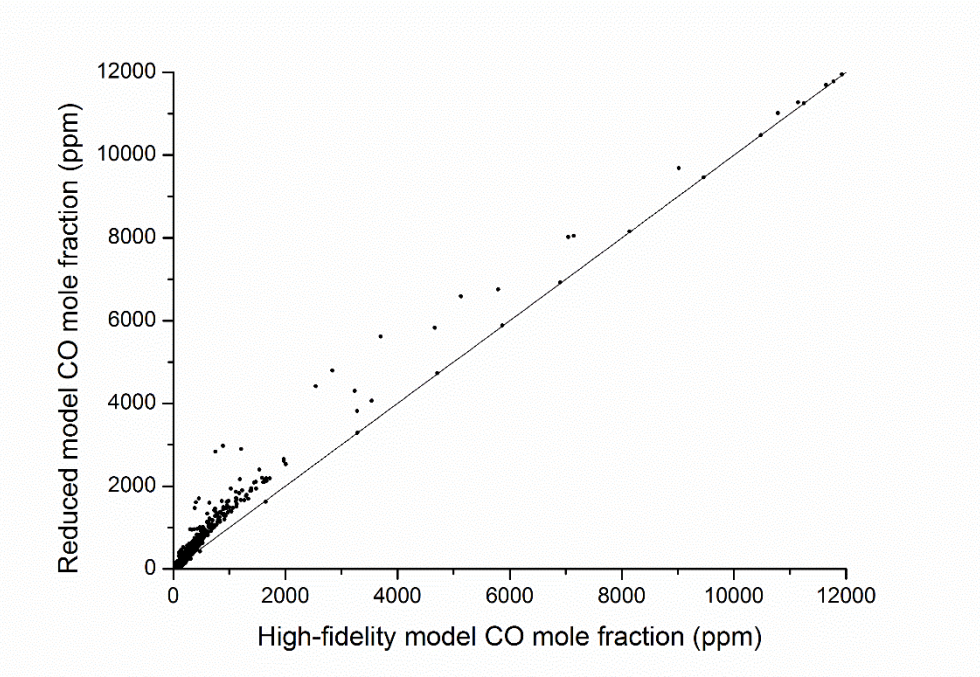

Figure 4.14: Scatter diagram of reduced-order model CO output mole fraction

In Figure 4.11 and Figure 4.13, it can be observed that the timing of the peaks fit well. However, the peaks' values do not fit well due to errors. In Figure 4.12 and Figure 4.14, it can be observed that the result points are more convergent to the line of y=x compared to the results with Chan and Hoang's parameter values. This is especially true regarding the results of HC output mole fraction. The experimental and simulated total output results are compared to verify the accuracy of the reduced-order model, as illustrated in Table 4.3 and Table 4.4.

Table 4.3: Total HC output results for the reduced-order model

Total Output Results (HC)	Values
Experiment (gram)	0.601
Experimental conversion efficiency	98%
Simulation (gram)	2.202
Simulated conversion efficiency	96%

Table 4.4: Total CO output results for the reduced-order model

Total Output Results (CO)	Values
Experiment (gram)	8.606
Experimental conversion efficiency	92%
Simulation (gram)	9.850
Simulated conversion efficiency	93%

The differences between the total output results are mainly caused by the unfitted peak values in the curves of the reduced-order model results. A few high peak values increase the difference. It can also be observed that the overall conversion efficiency is similar between the simulation and the experiment.

A comparison between the NO results of the reduced-order model and the high-fidelity model is conducted, as shown in Figure 4.15.

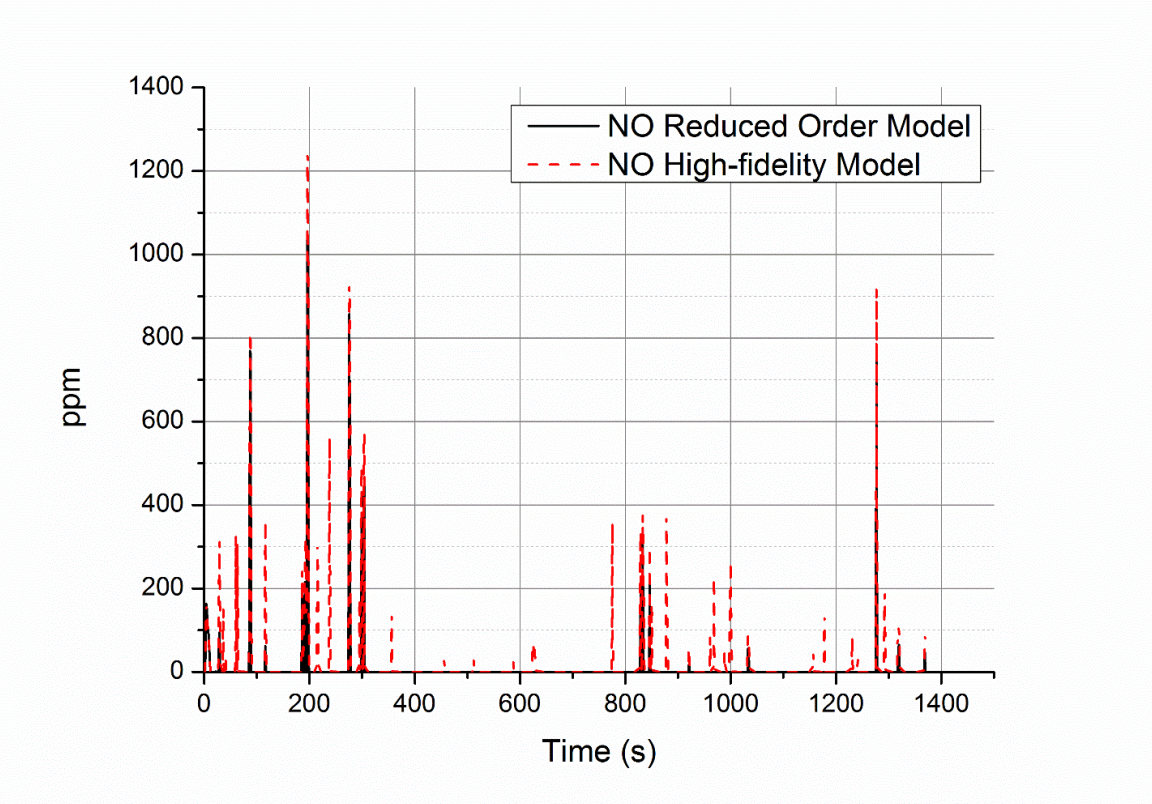

Figure 4.15: NO mole fraction result curves of the reduced-order model and high-fidelity model

It can be observed in Figure 4.15 that the NO mole fraction curves fit well, and the error is acceptable for most of the points. It can be concluded that the simplification of the reactions does not significantly affect the NO mole fraction.

Considered overall, the model reduction does not significantly increase the errors in the outlet temperature. For the outlet mole fraction, the model reduction results in some errors for some specific species, especially HC. The peak values in the reduced-order model's driving cycle simulation significantly raise the error of the total output result for

HC. However, the reduced-order model is a control-oriented model. It is developed to be applied in the thermal management system to control the TWC converter's temperature and detect system failures. Therefore, the accuracy requirements for temperature are higher than those for the species' outlet mole fractions. Thus, the accuracy of the reduced-order model is acceptable due to the high accuracy of the outlet temperature. On the other hand, the control algorithm can remedy the inaccuracy of the model.

Chapter 5 . Conclusions and Future Work

5.1 Research conclusions

In this thesis, the heat and mass transfer mechanism and the reaction kinetics in the TWC converter are analysed by building a high-fidelity TWC converter model. The heat transfer mechanism and warming-up performance are tested by the constant inlet simulation. The reaction rate parameters, including the pre-exponent multiplier and the activation energy are validated by minimizing the differences between the tested data and simulated data in the driving cycle simulation. The testing results illustrate that the high-fidelity model can represent the real mechanism of the TWC converter at a higher accuracy level, which is sufficient for model based control system and state estimation.

Based on the constant inlet simulation and driving cycle simulation results of the high-fidelity model, the phase and reaction simplifications are processed to simplify the converter model. The phase simplification is achieved by merging the gas and solid phases. The reaction simplification is achieved by reducing the number of reactions taken into consideration. From the comparison between the reduced order model and high-fidelity model results, the conclusion can be drawn that the current reduction method can guarantee the reduced order model a higher accuracy while decreasing the computational cost. The error caused by the simplification is acceptable for the application of the control system and the state estimation for OBD.

5.2 Future work

The first future work recommendation is about the high-fidelity model parameters tuning. As mentioned in Chapter 3 the reaction rate parameters are tuned in the driving cycle simulation in the present research. However, the transient inlet during the driving cycle simulation raises the measurement uncertainty of the mole fraction and temperature, which make the tuning more complicated and inaccurate. An alternative way is to tune the reaction rate parameters by constant inlet simulation, which is applied by Harsha [76]. If the constant inlet experimental data can be gathered, the reaction rate parameters can be tuned accurately by minimizing the conversion efficiency error between experimental data and simulation data.

For model simulation, the model can be simulated by applying a different set of inlets, including different driving cycles and engine types. The generality of the high-fidelity and reduced order model can be proved if the models performed well under different work conditions.

In addition, more advanced control strategies can be employed. Some close-loop control strategies under study can reach a better overall conversion [80][81][53]. The reduced order model presented in this study can be verified to explore the serviceability to a more advanced close-loop control strategy. The reduced order model can also be applied to the state estimation. For example, in research [59] and [58], a similar model was used to predict the internal temperatures. Some prediction methods, for instance, Extended Kalman

Filter (EKF) can reach a higher accuracy level in predicting the internal temperatures of the converter.

Appendix A: The specific heat coefficient and enthalpy constant of all the species

Species name	O_2
a_1	-34255.6342
a_2	484.700097
a_3	1.119010961
a_4	0.00429388924
a_5	-6.83630052E-7
a_6	-2.0233727E-9
a_7	1.039040018E12
b	18.4969947

Species name	CO_2
a_1	49436.5054
a_2	-626.411601
a_3	5.30172524
a_4	0.002503813816
a_5	-2.127308728E-7
a_6	-7.68998878E-13
a_7	2.849677801W-13
b	-45281.9846

Species name	H_2O
a_1	-39479.6083
a_2	575.573102
a_3	0.931782653
a_4	0.00722271286
a_5	-7.34255737E-6
a_6	4.95504349E-9
a_7	-1.33693E-12
b	-33039.7431

Species name	C_3H_6
a_1	-191246.2174
a_2	3542.07424
a_3	-21.14878626
a_4	0.0890148479
a_5	-1.001429154E-4
a_6	6.26795939E-8
a_7	-1.637871E-11
b	-15299.61824

Species name	C_3H_8
a_1	-243314.4337
a_2	4656.27081
a_3	-29.39466091
a_4	0.1188952745
a_5	-1.376308269E-4
a_6	8.81482391E-8
a_7	-2.342988E-11
b	-35403.3527

Species name	NO
a_1	-11439.16503
a_2	153.6467592
a_3	3.43146873
a_4	-0.002668592368
a_5	8.48139912E-6
a_6	-7.68511105E-9
a_7	2.3868E-12
b	9098.21441

Species name	CO
a_1	14890.45326
a_2	-292.2285939
a_3	5.72452717
a_4	-0.00817623503
a_5	1.456903469E-5
a_6	-1.087746302E-8
a_7	3.02794E-12
b	-13031.31878

Species name	H_2
a_1	40783.2321
a_2	-800.918604
a_3	8.21470201
a_4	-0.01269714457
a_5	1.753605076E-5
a_6	-1.20286027E-8
a_7	3.36809E-12
b	2682.484665

Species name	N_2
a_1	22103.71497
a_2	-381.846182
a_3	6.08273836
a_4	-0.00853091441
a_5	1.384646189E-5
a_6	-9.62579362E-9
a_7	2.519705809E-12
b	710.846086

Appendix B: The specific heat of cordierite under different temperature

Temperature (K)	Specific heat $(J/kg \cdot k)$
300	736.13
340	826.89
390	906
460	980.43
540	1037.44
630	1082.73
725	1118.75
820	1147.83
920	1173.94
1015	1196

Appendix C: The analysis of Biot number (Bi)

Biot number gives a simple index of the ratio of the heat transfer resistances inside of and at the surface of a body.

Biot number

$$Bi = \frac{hD_h}{\lambda_{sb}}$$

Gas-solid heat transfer coefficient

$$h = Nu\frac{\lambda_g}{D_h}$$

Where

$$\lambda_g = 2.66 \times 10^{-4} T_g^{0.805}$$

We assume asymptotic (constant) Nusselt number (Nu) for simulation purposes. The channel cross-section is assumed to be close to a square geometry, and correspondingly a value of Nu = 3 is chosen [28] [65]. The solid heat conductivity λ_{sb} is 1.5.

$$Bi = \frac{3}{1.5} \times 2.66 \times 10^{-4} T_g^{0.805}$$

During the entire driving cycle, the input temperature is lower than 900K. Therefore, the maximum value of Biot number in the entire driving cycle is 0.12, and for majority of

times the Biot number is lower than 0.1. Values of the Biot number smaller than 0.1 imply that the heat conduction inside the body is much faster than the heat convection away from its surface, and temperature gradients are negligible inside of it. The temperature can be assumed to be constant throughout the material's volume. The assumption 1 is approved to be feasible.

Appendix D: The assurance of the adequacy of the model time step and grid step size

The adequacy of the time and space discretization size are taken under consideration during this version of revision. To assure the adequacy of the space discretization size, the outlet temperatures of three converter discretization length (1mm, 5mm and 10mm) are taken under comparison. To simplify the procedure, the comparison of outlet mole fraction is omitted. The time step size is 1s. The comparison result curve is shown in figure below.

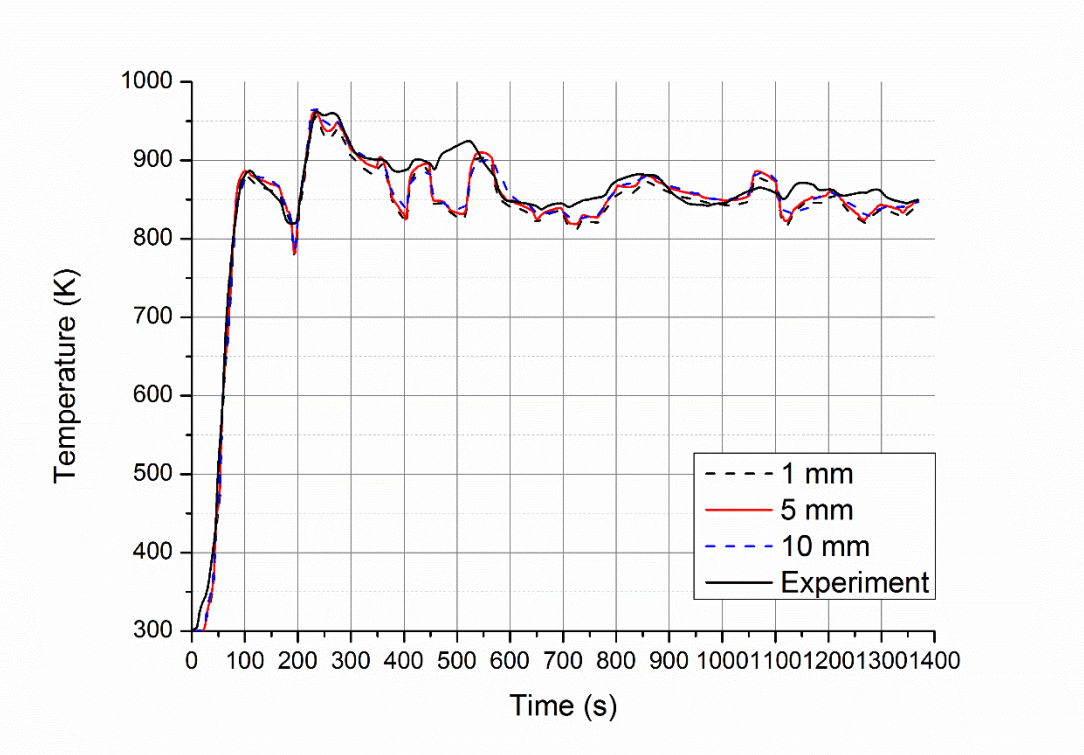

The outlet temperature of different converter discretization length

From the figure it can be observed that the outlet temperature under the discretization length of 1mm, 5mm, and 10mm are extremely closed. Therefore, the chosen of discretization length does not cause a significant impact on the outcome.

To test the adequacy of the discretization time step, the outlet temperatures of three time step sizes (1s, 5s and 10s) are taken under comparison. The discretization length is 5mm. the comparison result curve is shown in figure below.

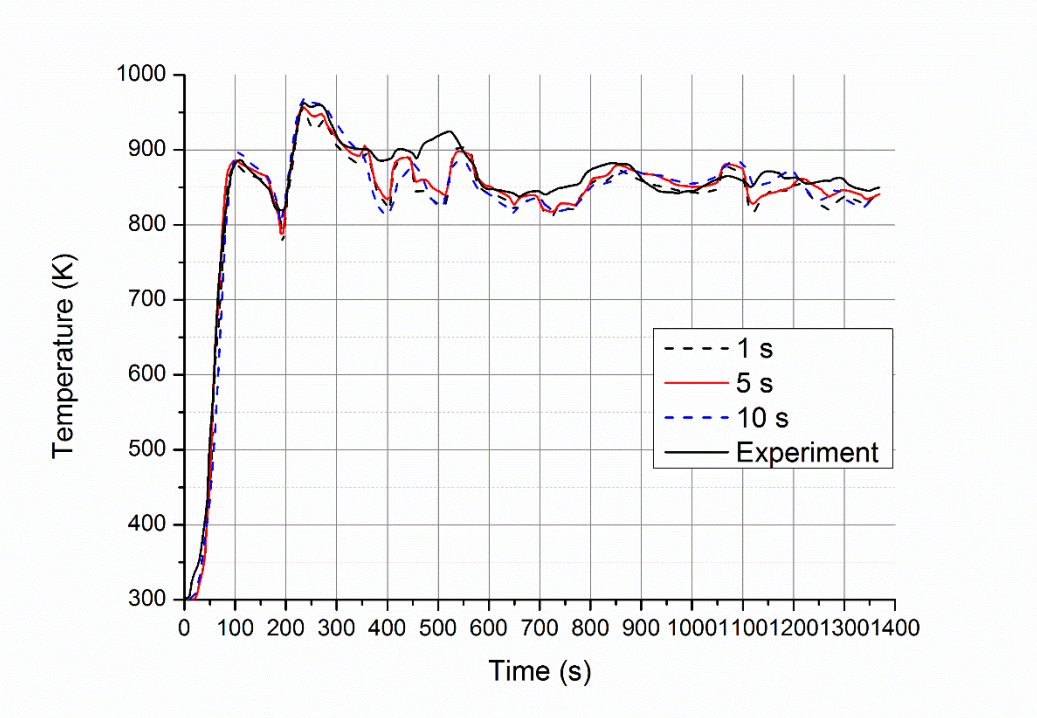

The outlet temperature of different time discretization sizes

From the figure it can be observed that the outlet temperature under the time discretization size of 1s, 5s, and 10s are also extremely closed. Therefore, the chosen of time discretization size does not cause a significant impact on the outcome either.

REFERENCES

[1] European parliment, “Council Directive 91/441/EEC of 26 June 1991 amending Directive 70/220/EEC on the approximation of the laws of the Member States relating to measures to be taken against air pollution by emissions from motor vehicles,” *Off. J. Eur. Communities*, no. 242, pp. 1–106, 1991.

[2] European Parliament, “Directive 98/69/EC of the European parliament and of the council of 13 October 1998 relating to measures to be taken against air pollution by emissions from motor vehicles and amending Council Directive 70/220/EEC,” *Off. J. Eur. Union*, vol. L350, pp. 1–56, 1998.

[3] European Parliament and Council of the European Union, “Regulation No 715/2007 of the European parliament and of the council of 20 June 2007 on type approval of motor vehicles with respect to emissions from light passenger and commercial vehicles (Euro 5 and Euro 6) and on access to vehicle repair and mai,” *Off. J. Eur. Union*, vol. L171, no. December 2006, pp. 1–16, 2007.

[4] N. Guillen-Hurtado, V. Rico-Perez, A. Garcia-Garcia, D. Lozano-Castello, and A. Bueno-Lopez, “Three-way catalysts: past, present and future,” *Edición Espec.*, pp. 114–121, 2012.

[5] D. I. Andrianov, C. Manzie, and M. J. Brear, “Spark ignition engine control strategies for minimising cold start fuel consumption under cumulative tailpipe

emissions constraints," *Control Eng. Pract.*, vol. 21, no. 8, pp. 1007–1019, 2013.

[6] S. Burch, M. Keyser, C. Colucci, T. Potter, D. Benson, and J. Biel, "Applications and Benefits of Catalytic Converter Thermal Management," in *SAE Technical*, 1996, p. Paper 961134.

[7] J. B. Heywood, *Internal Combustion Engine Fundementals*, vol. 21. 1988.

[8] C. P. Please, P. S. Hagan, and D. W. Schwendeman, "Light-off Behavior of Catalytic Converters," *SIAM J. Appl. Math.*, vol. 54, no. 1, pp. 72–92, Feb. 1994.

[9] H. Birgersson, L. Eriksson, M. Boutonnet, and S. G. Jaras, "Thermal gas treatment to regenerate spent automotive three-way exhaust gas catalysts (TWC)," *Appl. Catal. B Environ.*, vol. 54, no. 3, pp. 193–200, 2004.

[10] D. S. Lafyatisa *et al.*, "Ambient temperature light-off for automobile emission control," *Appl. Catal. B Environ.*, vol. 18, no. 1, pp. 123–135, 1998.

[11] R. J. Farrauto and R. M. Heck, "Catalytic converters: state of the art and perspectives," *Catal. Today*, vol. 51, no. 3–4, pp. 351–360, 1999.

[12] H. S. Gandhi, G. W. Graham, and R. W. McCabe, "Automotive exhaust catalysis," *J. Catal.*, vol. 216, no. 1, pp. 433–442, 2003.

[13] L. Guzzella and C. H. Onder, *Introduction to Modeling and Control of Internal Combustion Engine Systems*. Berlin, Heidelberg: Springer Berlin Heidelberg, 2010.

[14] K. S. Daiji Isobe, "Internal combustion engine control with fast exhaust catalyst warm-up," 1996.

[15] D. Bresch-Pietri, T. Leroy, and N. Petit, *Control-oriented input-delay model of the distributed temperature of a SI engine exhaust catalyst*. 2014.

[16] D. Andrianov, C. Manzie, and M. Brear, "A Methodology for Minimising Emissions Constrained Cold Start Fuel Consumption," in *SAE Technical Paper*, 2012, p. 11.

[17] K. S. Chen, et al , "Motorcycle emissions and fuel consumption in urban and rural driving conditions," *Sci. Total Environ.*, vol. 312, no. 1–3, pp. 113–122, Aug. 2003.

[18] H. Couetouse and D. Gentile, "Cooling System Control in Automotive Engines," in *SAE Technical Paper*, 1992, p. 11.

[19] D. Bresch-Pietri, T. Leroy, and N. Petit, "Control-oriented time-varying input-delayed temperature model for SI engine exhaust catalyst," in *American Control Conference*, 2013, pp. 2192–2198.

[20] V. Cioffi, S. Scala, and E. Sepe, "Control Oriented Modeling of the Exhausted Gas After-treatment System," in *International Workshop on Modeling, Emissions and Control of Automotive Engines*, 2001.

[21] E. P. Brandt, Y. Wang, and J. W. Grizzle, "Dynamic modeling of a three-way catalyst for SI engine exhaust emission control," *IEEE Trans. Control Syst. Technol.*, vol. 8, no. 5, pp. 767–776, 2000.

[22] P. Kiwitz, C. Onder, and L. Guzzella, "Control-oriented modeling of a three-way catalytic converter with observation of the relative oxygen level profile," *J. Process Control*, vol. 22, no. 6, pp. 984–994, 2012.

[23] J. Peyton Jones, J. Roberts, P. Bernard, and R. Jackson, "A Simplified Model for the Dynamics of a Three-Way Catalytic Converter," *SAE Technical Paper* 2000-01-0652, 2000.

[24] G. C. Koltsakis, P. A. Konstantinidis, and A. M. Stamatelos, "Development and application range of mathematical models for 3-way catalytic converters," *Appl. Catal. B Environ.*, vol. 12, no. 2–3, pp. 161–191, Jun. 1997.

[25] J. Peyton Jones, J. Roberts, J. Pan, and R. Jackson, "Modeling the Transient Characteristics of a Three-Way Catalyst," *SAE Technical Paper* 1999-01-0460, 1999.

[26] D. Chatterjee *et al.*, "Detailed surface reaction mechanism in a three-way catalyst," *Faraday Discuss.*, vol. 119, no. 1, pp. 371–384, Nov. 2001.

[27] C. Larese *et al.*, "Effects of calcination temperature on the stability of CePO4 detected in vehicle-aged commercial three-way catalysts," *Appl. Catal. B Environ.*, vol. 48, no. 2, pp. 113–123, Mar. 2004.

[28] K. Ramanathan and C. S. Sharma, "Kinetic parameters estimation for three way catalyst modeling," *Ind. Eng. Chem. Res.*, vol. 50, no. 17, pp. 9960–9979, 2011.

[29] P. Granger, C. Dujardin, J. F. Paul, and G. Leclercq, "An overview of kinetic and spectroscopic investigations on three-way catalysts: mechanistic aspects of the CO+NO and CO+N2O reactions," *J. Mol. Catal. A Chem.*, vol. 228, no. 1–2, pp. 241–253, Mar. 2005.

[30] P. Laing, M. Shane, S. Son, A. Adamczyk, and P. Li, "A Simplified Approach to Modeling Exhaust System Emissions: SIMTWC," *SAE Technical Paper* 1999-01-3476, 1999.

[31] J. Koop and O. Deutschmann, "Detailed surface reaction mechanism for Pt-catalyzed abatement of automotive exhaust gases," *Appl. Catal. B Environ.*, vol. 91, pp. 47–58, 2009.

[32] H. J. Kwon, J. H. Baik, Y. T. Kwon, I. S. Nam, and S. H. Oh, "Detailed reaction kinetics over commercial three-way catalysts," *Chem. Eng. Sci.*, vol. 62, pp. 5042–5047, 2007.

[33] N. Mladenov, J. Koop, S. Tischer, and O. Deutschmann, "Modeling of transport and chemistry in channel flows of automotive catalytic converters," *Chem. Eng. Sci.*, vol. 65, pp. 812–826, 2009.

[34] S. E. Voltz, C. R. Morgan, D. Liederman, and S. M. Jacob, "Kinetic Study of Carbon Monoxide and Propylene Oxidation on Platinum Catalysts," in *Ind. Eng. Chem. Res.*, 1973, p. 294.

[35] S. K. Rao, R. Imam, K. Ramanathan, and S. Pushpavanam, "Sensitivity Analysis and Kinetic Parameter Estimation in a Three Way Catalytic Converter," *Ind. Eng. Chem. Res.*, vol. 48, no. 8, pp. 3779–3790, 2009.

[36] G. Pontikakis, C. Papadimitriou, and A. Stamatelos, "Kinetic Parameter Estimation by Standard Optimization Methods in Catalytic Converter Modeling," *Chem. Eng.*

Comm, vol. 191, pp. 1473–1501, 2004.

[37] C. Montreuil, S. Williams, and A. Adamczyk, "Modeling Current Generation Catalytic Converters: Laboratory Experiments and Kinetic Parameter Optimization - Steady State Kinetics," *SAE Technical Paper* 920096, 1992.

[38] L. Glielmo, S. Santini and G. Serra, "A Two-Time-Scale Infinite-Adsorption Model of Three Way Catalytic Converters During the Warm-Up Phase," *J. Dyn. Syst. Meas. Control*, vol. 123, no. 1, p. 62, 2001.

[39] G. N. Pontikakis, G. S. Konstantas, and A. M. Stamatelos, "Three-Way Catalytic Converter Modeling as a Modern Engineering Design Tool," in *Trans ASME*, 2004, p. 23.

[40] J. Votruba, O. Mikus, K. Nguen, V. Hlavacek, and J. Skrivanek, "Heat and mass transfer in honeycomb catalysts—II," *Chem. Eng. Sci.*, vol. 30, no. 2, pp. 201–206, Feb. 1975.

[41] B. C. Pak and Y. I. Cho, "Heat and mass trasnfer in monolithic honeycomb catalysts-I," *Exp. Heat Transf.*, vol. 11, no. 2, pp. 151–170, Apr. 1998.

[42] K. N. Pattas *et al.*, "Transient Modeling of 3-Way Catalytic Converters," *SAE Technical Paper* 940934, 1994.

[43] K. Zygourakis, "Transient operation of monolith catalytic converters: a two-dimensional reactor model and the effects of radially nonuniform flow distributions," *Chem. Eng. Sci.*, vol. 44, no. 9, pp. 2075–2086, 1989.

[44] J. Votruba, J. Sinkule, V. Hlavaceks, and J. Skrivanek, "Heat and mass transfer in monolithic honeycomb catalysts-I," *Chem. Engineeting Sci.*, vol. 30, pp. 117–123, 1975.

[45] M. Flytzani-Stephanopoulos, G. E. Voecks, and T. Charng, "Modeling of Heat Trasnfer in Non-Adiabatic Monolith Reactors and Experimental Comparison of Metal Monolith With Packed Beds," vol. 41, no. 5, pp. 1203–1212, 1986.

[46] A. L. Boehman, "Radiation heat transfer in catalytic monoliths," *AIChE J.*, vol. 44, no. 12, pp. 2745–2755, Dec. 1998.

[47] L. C. Young and B. A. Finlayson, "Mathematical Models of the Monolith Converter," *AIChE J.*, vol. 22, no. 2, pp. 331–344, 1976.

[48] S. H. Oh and J. C. Cavendish, "Transients of Monolithic Catalytic Converters: Response to Step Changes in Feedstream Temperature as Related to Controlling Automobile Emissions," *Ind. Eng. Chem. Rod. Res. Dev*, vol. 1082, no. 21, pp. 29–37.

[49] D. K. S. Chen, E. J. Bissett, S. H. Oh, and D. L. Van Ostrom, "A Three-Dimensional Model for the Analysis of Transient Thermal and Conversion Characteristics of Monolithic Catalytic Converters," in *SAE Technical Paper* 880282, 1988.

[50] S. H. Oh, E. J. Bissett, and P. A. Battiston, "Mathematical Modeling of Electrically Heated Monolith Converters: Model Formulation, Numerical Methods, and Experimental Verification," *Ind. Eng. Chem. Res*, vol. 32, pp. 1560–1567, 1993.

[51] N. Kruse, A. Frennet, and J. M. Bastin, *Catalysis and automotive pollution control IV : proceedings of the Fourth International Symposium (CAPoC4), Brussels, Belgium, April 9-11, 1997*. Elsevier, 1998.

[52] E. P. Brandt, Y. Wang, and J. W. Grizzle, "Dynamic modeling of a three-way catalyst for SI engine exhaust emission control," *IEEE Trans. Control Syst. Technol.*, vol. 8, no. 5, pp. 767–776, 2000.

[53] F. Aimard, S. Li, and M. Sorine, "Mathematical modeling of automotive three-way catalytic converters with oxygen storage capacity," *Control Eng. Pract.*, vol. 8, no. 4, pp. 1119–1124, 1996.

[54] P. Koci, M. Kubicek, and M. Marek, "Modeling of Three-Way-Catalyst Monolith Converters with Microkinetics and Diffusion in the Washcoat," *Ind. Eng. Chem. Res.*, vol. 43, no. 16, pp. 4503–4510, 2004.

[55] E. P. Brandt, Y. Wang, and J. W. Grizzle, "A Simplified Three-Way Catalyst Model for Use in On-Board SI Engine Control and Diagnostics," *Proc. ASME Dyn. Syst. Contr. Div*, vol. 61, pp. 653–659, 1997.

[56] E. Shafai, C. Roduner, and H. Geering, "Indirect Adaptive Control of a Three-Way Catalyst," *SAE Int. Congr*, Feb. 1996.

[57] V. Pandey, B. Jeanneret, S. Gillet, A. Keromnes, and L. Le Moyne, "A simplified thermal model for the three way catalytic converter," *21st Int. Transp. Air Pollut. Conf.*, 2016.

[58] H. Surenahalli, G. Parker, and J. Johnson, "Extended Kalman Filter to Estimate NO , NO 2 , Hydrocarbon and Temperatures in a DOC during Active Regeneration and Under Steady State Conditions," *SAE Technical Paper 2*015-01-1059, 2015.

[59] H. Surenahalli, G. Parker, J. Johnson, and M. N. Devarakonda, "A Kalman Filter Estimator for a Diesel Oxidation Catalyst During Active Regeneration of a CPF," *Am. Control Conf. (ACC), 2012*, pp. 4969–4974, 2012.

[60] H. C. Kang, T. A. Jachimowski, and W. H. Weinberg, "Role of local configurations in a Langmuir–Hinshelwood surface reaction: Kinetics and compensation," *J. Chem. Phys.*, vol. 93, no. 2, pp. 1418–1429, Jul. 1990.

[61] Z. Hu *et al.*, "Performance and Structure of Pt–Rh Three-Way Catalysts: Mechanism for Pt/Rh Synergism," *J. Catal.*, vol. 174, no. 1, pp. 13–21, Feb. 1998.

[62] Y. Peng, "Properties of ceramic foam catalyst supports: one-dimensional and two-dimensional heat transfer correlations," *Appl. Catal. A Gen.*, vol. 266, no. 2, pp. 235–244, Jul. 2004.

[63] G. F. Hewitt, G. L. Shires, and T. R. Bott, *Process heat transfer*. 1994.

[64] B. Todd and J. B. Young, "Thermodynamic and transport properties of gases for use in solid oxide fuel cell modelling." *Journal of Power Sources*, Volume 320, 15 July 2016, Pages 349

[65] K. Ramanathan, V. Balakotaiah, and D. H. West, "Geometry effects on ignition in catalytic monoliths," *AIChE J.*, vol. 50, no. 7, pp. 1493–1509, Jul. 2004.

[66] G. Technologies, “GT-SUITE Exhaust Aftertreatment Application Manual.”

[67] B. I. Khaikin and A. G. Merzhanov, “Theory of thermal propagation of a chemical reaction front,” *Combust. Explos. Shock Waves*, vol. 2, no. 3, pp. 22–27, 1969.

[68] J. Ning and F. Yan, “IMC based iterative learning control of DOC temperature during DPF regerneration,” in *2016 European Control Conference (ECC)*, 2016, pp. 1051–1056.

[69] P. Hanggi, P. Talkner, and M. Borkovec, “Reaction-rate theory: fifty years after Kramers,” *Rev. Mod. Phys.*, vol. 62, no. 2, pp. 251–341, Apr. 1990.

[70] W. M. Irvine, “Langmuir-Hinshelwood Mechanism,” in *Encyclopedia of Astrobiology*, Berlin, Heidelberg: Springer Berlin Heidelberg, 2011, pp. 905–905.

[71] K. M. Khan and E. V. Albano, “Catalytic oxidation of carbon monoxide: a lattice gas non-thermal Langmuir–Hinshelwood mechanism,” *Chem. Phys.*, vol. 276, no. 2, pp. 129–137, Feb. 2002.

[72] S. Turns, *Chemical properties handbook : physical, thermodynamic, environmental, transport, safety, and health related properties for organic and inorganic chemicals*. McGraw-Hill, 1999.

[73] R. Douglas, “AFR and Emissions Calculations for Two-Stroke Cycle Engines,” 1990.

[74] S. R. Turns, *An introduction to combustion : concepts and applications*. McGraw-Hill, 2012.

[75] T. Morel, J. Silvestri, K. Goerg, and R. Jebasinski, "Modeling of Engine Exhaust Acoustics," *SAE Technical Paper* 1999-01-1665, 199.

[76] H. S. Surenahalli, "Dynamic Model Based State Estimation in a Heavy Duty Diesel Aftertreatment System for Onboard Diagnostics and Controls," Michigan Technological University, *ProQuest Dissertations Publishing*, 2013. 3595423.

[77] M. Montazeri-Gh and M. Naghizadeh, "Development of Car Drive Cycle for Simulation of Emissions And Fuel Economy," in *European Simulation Symposium Proceedings*, 2003, p. 6.

[78] S. H. Chan and D. L. Hoang, "Heat transfer and chemical reactions in exhaust system of a cold-start engine," *Int. J. Heat Mass Transf.*, 1998.

[79] S. Siemund, J. P. Leclerc, D. Schweich, M. Prigent, and F. Castagna, "Three-way monolithic converter: Simulations versus experiments," *Chem. Eng. Sci.*, vol. 51, no. 15, pp. 3709–3720, Aug. 1996.

[80] T. Maunula, A. Vakkilainen, A. Lievonen, K. Torkkell, K. Niskanen, and M. Harkonen, "Low Emission Three-way Catalyst and OSC Material Development for OBD Diagnostics," *SAE Technical Paper* 1999-01-3625, 1999.

[81] G. Haraldsson, P. Tunestal, B. Johansson, and J. Hyvonen, "HCCI Closed-Loop Combustion Control Using Fast Thermal Management," *SAE Technical Paper* 2004-01-0943, 2004.